UNIVERSITÉ PARIS SUD

Comprendre le monde, construire l'avenir®

FACULTÉ DES SCIENCES D'ORSAY

UNIVERSITE PARIS-SUD

ÉCOLE DOCTORALE : STITS
Institut d'Electronique Fondamentale

DISCIPLINE : PHYSIQUE

THÈSE DE DOCTORAT

soutenue le 24/10/2012

par

Khanh Van DO

Contribution à l'Exploration des Propriétés Dispersives et de Polarisation de Structures à Cristaux Photoniques Graduels

Directeur de thèse : Eric CASSAN, Professeur, Université Paris-Sud

Composition du jury :

Président du jury :
Rapporteurs : Emmanuel CENTENO, Professeur, Université Montpellier II
Olivier VANBESIEN, Professeur, Université Lille 1
Examinateurs : Alfredo de ROSSI, HDR, Thales Group
Anne TALNEAU, DR, LPN- CNRS
Eric CASSAN, Professeur, Université Paris-Sud
Frédérique de FORNEL, DR, Université de Bourgogne

Acknowledgement

First and foremost, I would like to express my sincere appreciation and deepest gratitude to my supervisor Professor Eric CASSAN from the MINAPHOT group of the Institut d'Electronique Fondamentale (IEF – UMR 8622 CNRS) for his encouragement, guidance and support during my thesis. His willingness to promote me professionally through advising and recommending on my work, and sending me to schools, conferences has been most generous.

I would like to thank the program Pôle Universitaire Français à Hanoi, the collaboration Master program between the Université Paris-Sud and the University of Engineering and Technology, Vietnam National University of Hanoi, where I followed my graduate study on Micro-and-Nano Technologies. My sincere thanks also sent to Professor Elisabeth Dufour-Gergam, representative of this Master program, for her kind helps on the first day I came to Paris and throughout my studies both in Vietnam and France.

It was a great opportunity for me to joint and work in a professional environment with enthusiastic, dynamic professors, technicians and colleagues in the Silicon Photonics Group during my three years. My many thanks devote to all group members for their support and friendship. On the top of this list, I am especially grateful to Xavier Le Roux, who provided a huge effort for the realization of graded photonic crystal structures in the CTU clean room. I would like to thank him for his main involvement in the fabrication of GPhC samples, for sharing me his technology expertise in the clean-room and for his fruitful discussions on the design, fabrication as well as investigation of GPhC samples involved in my thesis.

I would like to warmly thank Laurent VIVIEN, Delphine MARRIS-MORINI and Anatole LUPU for their availability and kindness to give me practical advices and helps on the characterization of samples. Thanks to it I have perhaps got valuable results which will be presented in this manuscript.

One part of the characterization of GPhC samples was done in the collaboration with the Groupe d'Optique de Champ Proche, Laboratoire Interdisciplinaire Carnot de Bourgogne (ICB Dijon). I would like to thank Professor Frédérique de FORNEL, Benoit CLUZEL and PhD student Jean DELLINGER for their efforts on investigating our samples, their great contribution and worth discussions on SNOM results.

Also, I would like to thank all members of the administrative and technical staff of IEF for the services they gave me during my study.

Finally, I am eternally grateful to my parents, my brothers, my second family in France Mme. Danièle ROUSSEAU and all of my friends for their constant love and encouragement.

Orsay, October 2012

Khanh Van DO

Table of contents

Acknowledgement i

Table of contents iii

Introduction 1

Chapter 1
Introduction to Photonic Crystals and Graded Photonic Crystals 3

1.1. Two-dimensional photonic crystals 3
1.1.1. Real lattice, reciprocal space and Brillouin zone 3
1.1.2. Band diagram 5
1.1.3. Conservation of parallel wave-vector at the interface between two media . 6
1.1.4 Equi-frequency surfaces and refraction at the interface with a photonic crystal 8
1.1.5. Some examples of dispersion effects in photonic crystals 11
1.1.5.1. Negative refraction 13
1.1.5.2. Self-collimation effect 13
1.1.5.3. Superlensing effect 15
1.1.5.4. Superprism effect 16
1.2. Planar two dimensional photonic crystals 17
1.3. Introduction to Graded Photonic Crystals 19
1.3.1. Introduction 19
1.3.2. Equi-frequency surface deformations 20
1.3.2.1. Equi-frequency surface deformations by changing the angle between the two primitive lattice vectors 20
1.3.2.2. Equi-frequency surface deformations by changing the aspect ratio between the two primitive lattice vectors 22
1.3.2.3. Equi-frequency surface deformations by the gradient of photonic crystal filling factor 23
1.4 Conclusion 24

Chapter 2
Hamiltonian optics-assisted ray tracing in graded photonic crystals using the local photonic bandstructure 25

2.1. General principle of Hamiltonian optics 26
2.2. Hamiltonian optics for graded photonic crystals 27
2.2.1. Hamiltonian optics for graded photonic crystals operating in the homogeneous regime 27
2.2.2. Hamiltonian optics for graded photonic crystals in the diffractive regime 31
2.2.2.1. Calculation of EFSs 32
2.2.2.2. Analytical extraction of EFSs for one particular case 33
2.2.2.3. Hamiltonian optics-assisted ray tracing in the chosen GPhC operating in the diffractive regime near the photonic bandgap 35
2.3 Conclusion 38

Chapter 3
Modeling and Simulation of Graded Photonic Crystals 39

3.1. Mirage and superbending effect in the considered square-lattice GPhC 39
3.1.1 Structure design 41
3.1.2. Circular 90°-bending GPhC structure 42
3.1.2.1. Study of the incident point to inject light into GPhC configuration 42
3.1.2.2. Light propagation in circular 90°-bending GPhC structure 44
3.1.2.3. Estimation of losses and bandwidth in the 90°-bending GPhC structure 45
3.1.2.4. Enhancement of the transmission efficiency in the 90°-bending GPhC structures 47
3.1.3. Other configurations for light bending effect 49
3.1.3.1. 180°-bending GPhC structure 49
3.1.3.2. 270°-bending GPhC structure 50
3.2. Wavelength dispersion sensitivity of graded photonic crystals 51
3.2.1. Sensitivity to wavelength 51
3.2.2. Two-channel demultiplexing 53
3.2.3. Four-channel demultiplexing 55
3.3. Polarization properties of graded photonic crystals 56
3.4. Conclusion 61

Chapter 4
Fabrication and Characterization of Graded Photonic Crystals 63

4.1. Description of fabrication process of considered GPhC structures 64
4.1.1. Mask design 65
4.1.2. Fabrication process in CTU clean room 68
4.1.2.1. Overview of fabrication process of the GPhC sample 68
4.1.2.2. Proximity effecs in e-beam lithography process 70
4.2. Description of characterization benches 72
4.2.1. Experimental setup for the far-field measurement 72
4.2.2. Experimental setup for the near field measurement 73
4.3. Results and discussions 75
4.3.1. SEM images of fabricated structures 75
4.3.2. Experimental investigation of the optical mirage and super-bending effect in GPhCs 76
4.3.2. Dispersion properties of the GPhC configuration 78
4.3.2.1. Dispersion properties of the considered GPhC configuration 78
4.3.2.1. Wavelength demultiplexing devices based on the considered GPhC configuration 81
4.3.3. Polarization-dependency of the GPhC configuration 82
4.3.4. Transition between homogenizable regime and PhC regime 83
4.4. Conclusion 90

Conclusion and Perspectives 91

References 93

French Summary 97

Publications and Conferences 113

Introduction

This thesis is in the context of the research efforts conducted in recent years on the investigation of artificial electromagnetic materials. The underlying pursed idea is to define structures and media with adjustable properties (where ε and μ values may be designed, for example) leading to original and/or exploitable electromagnetic phenomena (invisibility, Luneberg or Maxwell's fish-eye lenses), and has led to the concept of metamaterials. Emblematic phenomena in metamaterials, such as "cloaking" or negative refraction, were first studied and then demonstrated experimentally in the range of microwave frequencies, typically in the period 2000-2006. Among those significant works, a particular one was presented by *D. Schurig et al.* in a well-known article published in the *Science* journal in 2006. The direct transposition of the concepts used at microwave frequencies to optical wavelengths in near infra-red range (λ~1.5μm) proved later to be more difficult than initially foreseen due to the technological constraints on fabrication techniques for the realization of "meta-atoms" with far sub-wavelength dimensions (around 50nm) and to the high level of metals optical absorption losses at optical frequencies. From a theoretical point of view, an adaptation of spatial coordinate transforms previously developed for metamaterials was proposed in 2008 by J. Li and J.B. Pendry as a new conformal transformation to take into account the use of media with quasi-isotropic properties usually encountered in optics (most of semiconductors including silicon, oxides, etc). Application of these ideas has led to several papers by American research groups (Stanford, Berkeley) reporting in 2009 experimental results on optical media obtained by the modulation of the effective index seen by light (index-map) using the drilling of holes in a silicon wafer with a control of the hole density. All of these advances have helped but have not solve all the problems, true photonic metamaterials reduced to non-index maps remaining based on the use of metals and therefore loss-limited. Another noticeable feature of these works is that optical media are almost systematically addressed within the principle of homogenization, which can lead to a very wide band operation provided that the employed meta-atoms have not a resonating behaviour, and this point is generally seen as an advantage.

In this context, this thesis has been devoted to the study of graded photonic crystals previously proposed in different works in the late 1990's and mi-2000's. The main common point with '*index-map materials*' recently employed as non-lossy photonic metamaterials is the use of all-dielectric structures generally made of an air-hole lattice etched in a silicon wafer with variable chirped parameters (such as the air-

hole filling factor). The main difference arises from the fact that the flexible choice of the lattice period to wavelength ratio (a/λ) can lead to two types of operating regimes of light propagation: the homogenization regime where $a/\lambda << 0.5$, and the diffractive one where a/λ (typically) > 0.2. The latter provides the possibility to reconfigure the optical paths of the beams propagating in the medium by tuning the light wavelength and thus to exploit the dispersive effects of the photonic crystals. It has attracted particular attention in our work.

Starting from October 2009, we first conducted preliminary studies to investigate the effect of opto-geometric deformations of planar photonic crystal lattices using Plane Wave Expansion calculations by considering the possibility of a gradual filling factor, a gradual variation of the orientation of the two basic vectors of the lattice and the aspect ratio between these two basic vectors, etc. They yielded interesting qualitative trends and opened perspectives to the present works. However, considering the richness and complexity of the possible two-dimensional gradients of lattice parameters and their combination, we chose to restrict the studies performed in this thesis to the case of a square lattice photonic crystal made of air hole with a two-dimensional gradual filling factor.

This thesis is organized into four chapters:

The first chapter gives the general concepts related to two-dimensional planar photonic crystals (PhCs) and graded photonic crystals (GPhCs). Their dispersive properties with respect to light propagation are presented in connection with the equi-frequency surface shapes. The observation of the dependency of graded photonic crystal equi-frequency surfaces (EFSs) with lattice deformations is also introduced in this chapter.

Chapter 2 aims at presenting a simple ray tracing approach for the study of light propagation in graded photonic crystals. The chosen approach is based on the two equations of Hamiltonian optics, the Hamiltonian being related to the local PhC dispersion relationship at each point along the propagation path. An analytical expression of EFSs as a function of varied lattice parameters is presented in this chapter through the extraction of the exploited EFSs for the particular GPhC studied reference structure made of a square photonic crystal with a varying air hole filling factor profile.

In chapter 3, simulations of graded photonic crystals are shown using the method of Hamiltonian optics ray tracing and the FDTD methods. The properties of light bending effect, sensitivity to wavelength, and polarization dependency of the proposed configuration are described and numerically studied in this chapter.

The fabrication process of GPhC sample as well as the experimental investigation of those samples are then presented in Chapter 4. Electron Beam Lithography and Reactive Ion Etching techniques are used for the fabrication of GPhCs samples and two methods of optical measurements are employed for the characterization of those fabricated GPhC samples.

Finally, we conclude and draw some possible perspectives on the study of GPhCs in the last part of this manuscript.

Chapter 1

Introduction to Photonic Crystals and Graded Photonic Crystals

This chapter is devoted to the presentation of the general concepts related to two-dimensional photonic crystals and graded photonic crystals. First, two-dimensional photonic crystals will be presented with their dispersive properties with respect to light propagation relying on the equi-frequency surface shapes. In the second part, we will see the basic concepts of graded photonic crystal structures made of a modulation of lattice parameters. Some sets of equi-frequency surfaces of different types of photonic crystals with different values of lattice parameters are then shown in order to have a qualitative insight into the study on graded photonic crystals based on the deformations of equi-frequency surfaces.

1.1. Two-dimensional photonic crystals

Two-dimensional photonic crystals (2D-PhCs) are structures with a periodic arrangement of low and high dielectric constants in two dimensions and infinite in the third dimension. 2D-PhCs exhibit most of important characteristics of planar photonic crystals and can be used to investigate many of the physical effects present in photonic crystal structures and devices.

1.1.1. Real lattice, reciprocal space and Brillouin zone

Two-dimensional photonic crystals can be represented in space by two **primitive vectors** $\vec{a}_1$ and $\vec{a}_2$ as seen in Fig. 1(a) and (c). 2D photonic crystals can be classified into different types corresponding to different sets of these two primitive vectors. We can see the dielectric map or real lattice of two common types of

photonic crystal structures: the square lattice in which $|\vec{a}_1| = |\vec{a}_2|$ and $\theta_{lattice} = (\vec{a}_1, \vec{a}_2) = 90°$ (Fig.1(a)) and the triangular lattice where $|\vec{a}_1| = |\vec{a}_2|$ and $\theta_{lattice} = (\vec{a}_1, \vec{a}_2) = 60°$ (Fig.1(c)). Photonic crystal structures are commonly known to be made of high index rods surrounded by a low index material or low index holes embedded in a high index material. Figs. 1(a) and (d) give an example of the real lattice dielectric maps of two simple photonic crystal structures (square and triangular lattices) made of air holes of radius $r = 0.3a$ in a high dielectric constant medium.

For the study of photonic crystal properties, beside the real lattice, we use also the two notions of **reciprocal space** and **Brillouin zone**.

Square lattice

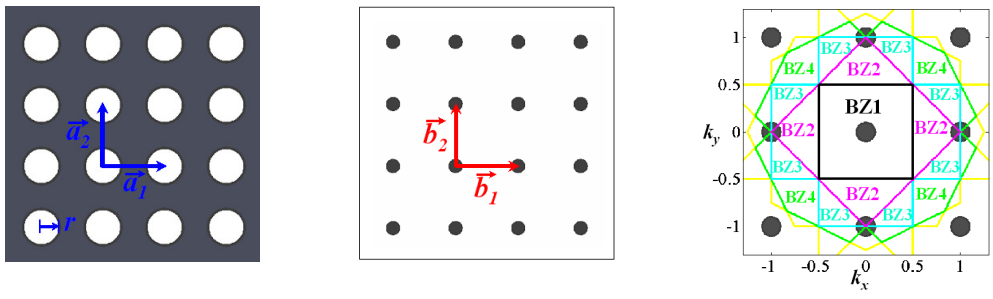

(a) (b) (c)

Triangular lattice

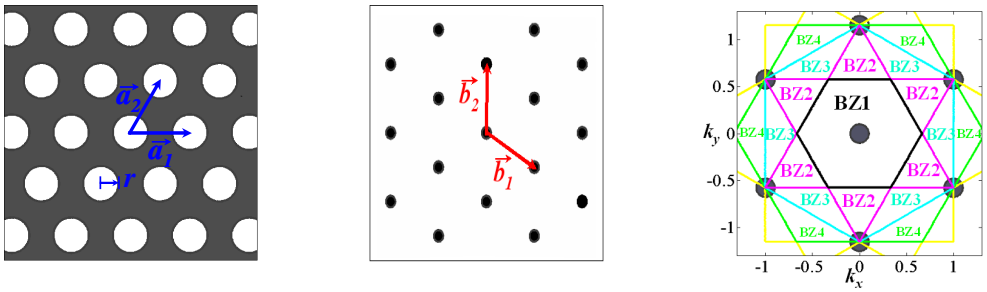

(d) (e) (f)

Figure 1.1: Real lattice, reciprocal lattice and Brillouin zones of (a), (b), (c) Square lattice $|\vec{a}_1| = |\vec{a}_2| = a$, $\theta_{lattice} = (\vec{a}_1, \vec{a}_2) = 90^o$; and (d), (e), (f) Triangular lattice $|\vec{a}_1| = |\vec{a}_2| = a$, $\theta_{lattice} = (\vec{a}_1, \vec{a}_2) = 60^o$ made of air holes $r = 0.3a$, respectively.

Reciprocal space: each set of direct lattice vectors defines two reciprocal lattice vectors which specify the reciprocal space. The reciprocal space of a 2D PhC is defined from the real lattice with the following relation:

$$\vec{a}_i . \vec{b}_j = 2\pi\delta_{ij} \tag{1.1}$$

where $\vec{a}_i$ and $\vec{b}_j$ are the primitive vectors in real lattice and reciprocal lattice, respectively, and δ_{ij} is the Kronecker symbol.

Brillouin zone: the first Brillouin zone can be visually defined as a region in the reciprocal space formed by the points which are closer to the original lattice point than to any other points. The first Brillouin zone has symmetry properties corresponding to the symmetries of the real lattice. Hence, in some cases, the irreducible Brillouin zone – the smallest surface that allows reconstructing the first Brillouin zone using the symmetries of the reciprocal lattice – can be used to characterize the properties of photonic crystals. We can see in Fig. 1.1 the two primitive vectors in reciprocal space and Brillouin zones of two types of photonic crystals: the square and triangular lattice. The first Brillouin zone of a square lattice is a square while it is hexagonal for the case of a triangular lattice.

The first Brillouin zone is the region containing all needed wave-vectors $\vec{k}$ for the study of band structure and dispersion properties of photonic crystals.

1.1.2. Band diagram

The study of photonic crystals is governed by the Bloch-Floquet theorem in such a way that the behaviour of waves propagating inside a periodic medium is regulated by a periodic envelope function multiplied by a plane wave. The solutions to this equation are the eigenvalues $\omega(\vec{k})$ and eigenvectors $\vec{k}$. The eigenvalues $\omega(\vec{k})$ are continuous functions of $\vec{k}$ and forming discrete bands in a band structure or dispersion diagram of the photonic crystal structure.

The band structure or dispersion diagram of a photonic crystal lattice is the graphical representation of the frequency (eigenvalues) against the wave-vector (eigenvectors) relationship. This relationship depends on both the lattice parameters and the polarization of light. In two dimensional systems, electromagnetic fields can be divided into two independent polarizations: the transverse electric (TE) modes, in which the electric field is in the plane of periodicity and the magnetic field is perpendicular to this plane, and the transverse magnetic (TM) modes where the magnetic field is in the plane of periodicity and the electric field is perpendicular to it. Then, the band structure of a photonic crystal lattice can also be separated in TE and TM bands.

Due to the scaling-invariance of Maxwell's equations, frequencies ω are conventionally given in the unit of $2\pi c/a$ as a normalized value, which is equivalent to a/λ, and the two components of wave-vector $\vec{k}(k_x, k_y)$ are given by:

$$\begin{aligned} \omega_{normalized} &= \frac{a}{2\pi c}\omega = \frac{a}{\lambda} \\ \vec{k}_{normalized} &= \frac{a}{2\pi}\vec{k} \end{aligned} \tag{1.2}$$

where a is the lattice constant and c the light speed in vacuum. For the simplicity, hereinafter, the written of ω and $\vec{k}$ are the normalized frequency, and normalized wave-vectors, respectively.

The bandstructure of a photonic crystal lattice is usually plotted along the main directions that are along the overall boundaries of the first Brillouin zone.

However, upon the symmetry of photonic crystals, it suffices to consider only the variation of the wave-vector $\vec{k}$ along the boundaries of the irreducible Brillouin zone, the smallest region that can be used to reproduce the first Brillouin zone. Fig.1.2. shows the bandstructure diagram of the square and the triangular lattices for both TE (red line) and TM (blue dashed line) polarizations along the main direction $\Gamma - X - M - \Gamma$ for the square lattice, and $\Gamma - M - K - \Gamma$ for the triangular lattice, respectively (the boundaries of the irreducible Brillouin zone presented as the orange regions in two insets of the two figures Fig. 1.2(a) and (b)).

The considered structure contains a photonic crystal lattice made of air holes (refractive index $n_{air} = \sqrt{\varepsilon_1} = 1$) embedded in the silicon host material ($n_{Si} = \sqrt{\varepsilon_2} = 3.45$). The hole radius for the two cases is $0.3a$. As can be seen in the figure, there is a TE band gap in the case of triangular lattice and there is no band gap for the case of square lattice. Inside the photonic bandgap, light is prohibited to propagate.

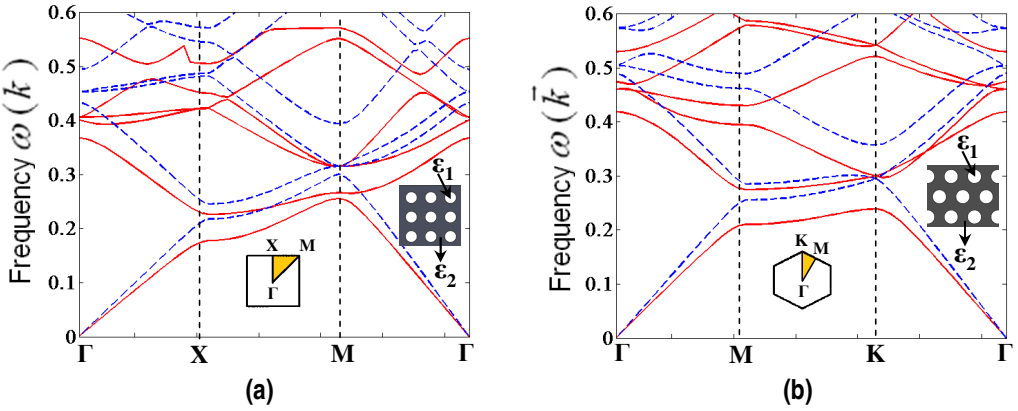

Figure 1.2.: Band structure diagram of 2D photonic crystal structures made of air hole ($r = 0.3$; $n_1 = \sqrt{\varepsilon_1} = 1$) in silicon (Si) host material ($n_2 = \sqrt{\varepsilon_2} = 3.45$) calculated by the Plane wave expansion method for the two both polarizations TE (red line) and TM (blue dashed line) of (a) the square lattice, (b) the triangular lattice.

1.1.3. Conservation of parallel wave-vector at the interface between two media

To study the properties of photonic crystal structures, in particular, the propagation of light inside photonic crystal structures, it is necessary to consider the coupling condition from the incident medium to the photonic crystal area. Let us first remind the simplest case: the condition for light coupling at the interface between two homogeneous media with refractive index of n_1 and n_2 in case of injecting one plane wave of frequency ω at incident angle θ_{in}. The reflection $\theta_{reflect}$ and the transmission angle θ_{trans} of light are then determined by the Snell-Descartes' laws in the following form:

$$n_1 \sin\theta_{in} = n_2 \sin\theta_{trans}$$
$$\theta_{reflect} = \theta_{in} \tag{1.3}$$

These laws represent in fact the conservation of the parallel component of the wave-vector at the interface between the two media:

$$k_{//} = k_{//(in)} = k_{//(reflect)} = k_{//(trans)} \tag{1.4}$$

In a homogeneous medium, the dispersion relation has the form of

$$k = n\frac{\omega}{c} \tag{1.5}$$

or :

$$k^2 = k_x^2 + k_y^2 = k_\perp^2 + k_{//}^2 = n^2\frac{\omega^2}{c^2} \tag{1.6}$$

that makes the so-called iso-frequency contours at constant frequencies in the (k_x, k_y) plane to be circles.

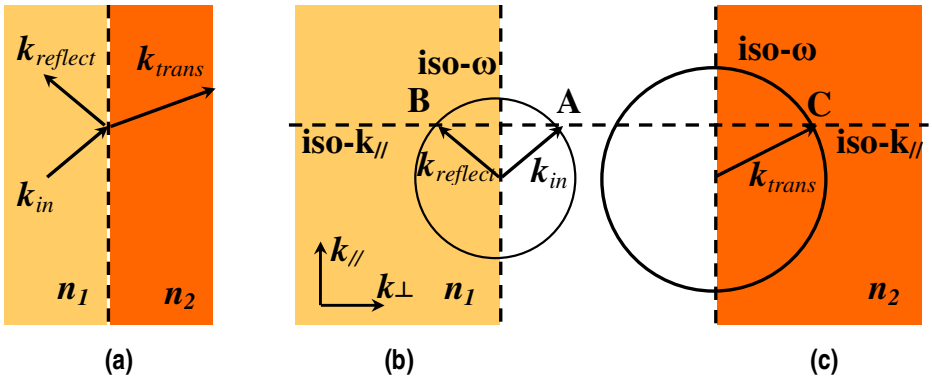

Figure 1.3: Propagation principle of a plane wave between two dielectric media (with refractive index n_1 and n_2): (a) Schematic wave-vector of incident, reflected and refracted (transmitted) waves; (b) Iso-frequency contour and parallel wave-vector in incident medium; and (c) Iso-frequency contour and parallel wave-vector in refracted medium

Fig. 1.3 presents the coupling principle at the interface of two homogeneous media relying on the conservation of parallel wave-vector. The incident wave-vector is at point A of the iso-frequency contour; the related input parallel wave-vector intersects the iso-frequency contour of the incident medium at point B, and the one of the refraction medium at point C, yielding the direction of reflected and transmitted waves.

It can be seen that the concept of iso-frequency contour is useful in defining the refraction effect between two media. In all cases, with respect to photonic crystal structures, the dispersion diagram is an important tool to characterize their dispersion properties.

In the following, the relationship between the concept of iso-frequency contour and the dispersion diagram of photonic crystals will be discussed to serve for the purpose of coupling light waves from an incident medium into 2D photonic crystals.

1.1.4 Equi-frequency surfaces and refraction at the interface with a photonic crystal

In section 1.1.2, for the plot of dispersion diagrams (bandstructures) of photonic crystal structures, only the main propagation directions being along the boundaries of the irreducible Brillouin zone defined by three critical points ($\Gamma(0,0)$, $X(0,0.5)$ and $M(0.5,0.5)$ for square lattice, and $\Gamma(0,0)$, $M(0,0.5)$, and $K(-1/3,1/3)$ for triangular lattice) were considered (see again Fig. 1.2). However, the Brillouin zone is a two-dimensional region of wave-vectors, and thus the dispersion diagram is actually made of surfaces as seen in Fig. 1.4(a). Each wave-vector $\vec{k}$ defined by a set of two components (k_x, k_y) in the wave-vector plane corresponds to one value of frequency of each discrete band of the photonic crystal, while for one frequency ω of each photonic band, there is a loci of wave-vectors $\vec{k}$. By projecting the dispersion surfaces of each photonic band onto the wave-vector plane, we can get the two-dimensional contours corresponding to the loci of allowed wave-vectors $\vec{k}(k_x, k_y)$ at fixed frequency ω in the reciprocal space. These contours are called the **Equi-Frequency Surfaces** (EFSs). It can be said that EFSs give a 2D visualization of the dispersion surfaces and they contain all possible wave-vectors at a given frequency.

As an example, Fig. 1.4(b) and 1.4(d) respectively map out the EFS diagram of the first and second TE bands of a square lattice photonic crystal made of air holes ($r = 0.3a$) in a silicon host material. Visually, we see that EFSs have different shapes for different frequencies and different bands.

If the band structure of photonic crystals gives information mainly on the photonic band gap, showing which frequency is allowed or prohibited to propagate inside the periodical medium, the EFS diagrams of photonic crystals bring more information on dispersive phenomena of such structure in allowed frequency ranges. Within a photonic crystal medium, the propagation of light can indeed be determined by the relationship [1]:

$$\vec{V}_G = \left(\frac{\partial \omega}{\partial k}\right) = grad_{\vec{k}}\left(\omega\left(\vec{k}\right)\right) \tag{1.7}$$

where $\vec{V}_G$ is the group velocity.

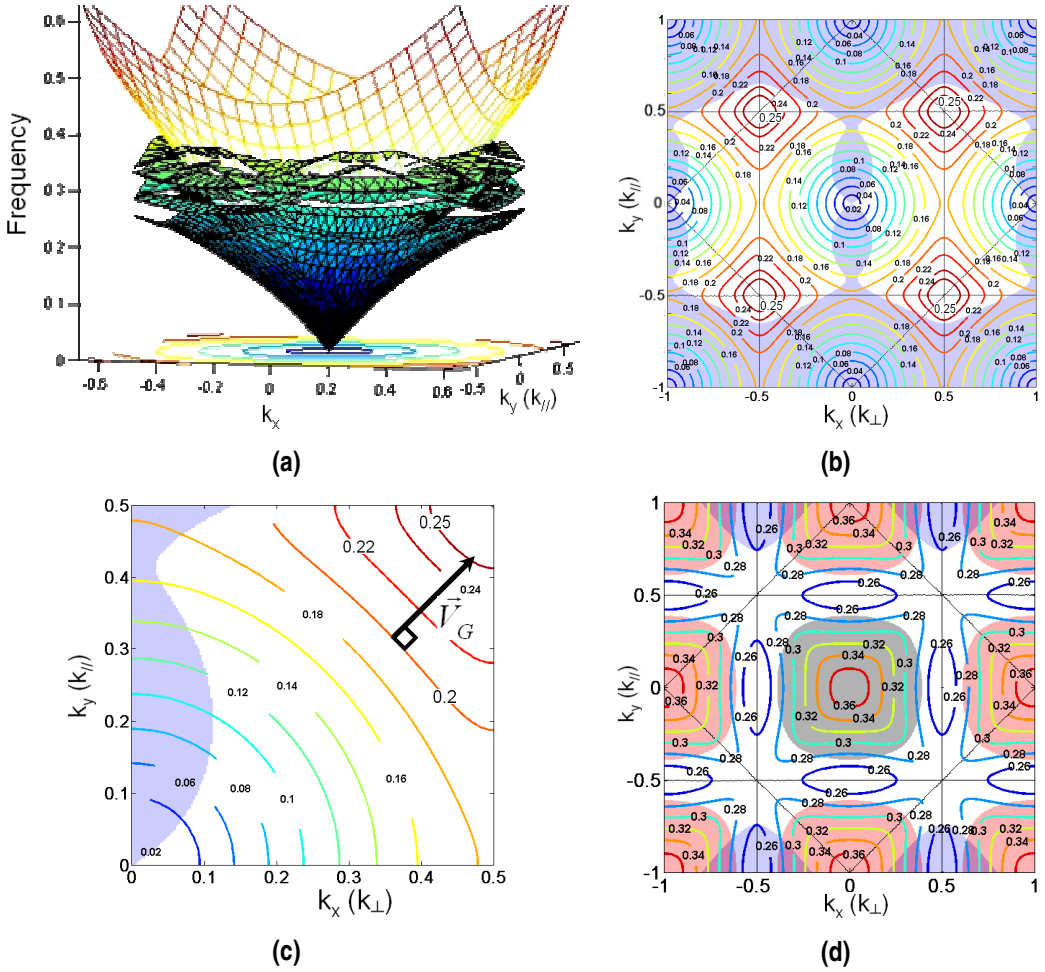

Figure 1.4: 2D square lattice photonic crystal made of air holes ($n_{air} = 1$, $r / a = 0.3$) in a silicon host material ($n_{Si} = 3.45$): (a) Dispersion surfaces; (b) Equi-frequency surfaces (EFSs) diagram for the first TE band; (c) EFSs diagram in the first quarter of 1st Brillouin zone for the first TE band with one group velocity at a given point; and (d) EFSs diagram for the second TE band.

The group velocity is therefore determined by the normal line to the EFS $\omega(k) = \omega_0$ at point $k(k_x, k_y)$, as presented in Fig. 1.4(c). The concavity of the EFSs then plays an important role. We will come back to this last point, which is important for the study of dispersive properties of GPhCs in Chapter 3 and Chapter 4.

Now, let us consider the case where an incident plane wave of frequency ω strikes an interface of a photonic crystal medium as figured out in Fig. 1.5(a). To couple the plane wave from a homogeneous medium into the PhC medium, it is needed to consider first of all which energy band the frequency ω is in. For example, light waves will be totally reflected if their frequency is inside the photonic bandgap. On the contrary, outside the photonic bandgap, some light can be transmitted or refracted, then propagating within the photonic crystal medium.

Secondly, the condition of conservation of parallel wave-vector $k_{//}$ must be matched at the interface between the two media. This condition is regulated by the

initial injected point and the incident angle of the light beam. As long as the $k_{//}$ conservation condition is satisfied, light is allowed to propagate inside the photonic crystal medium with a Bloch wave directed along the group velocity direction, i.e. along to the normal line to the EFS of frequency ω. Fig. 1.5 shows a typical example of this kind of situation. As can be seen, a plane wave of normalized frequency $\omega = 0.276$ is injected into a 45°-rotated square photonic crystal lattice with an incident angle θ from air. Frequency ω corresponds to the black circle iso-frequency contour in air (incident medium) and the red EFS in the photonic crystal medium. The excited EFS has the form of a circle, centred at the edge of the first Brillouin zone. With the condition of matched parallel wave-vector $k_{//}$, the direction of reflected waves and refracted waves are determined and presented by the dark blue and red vectors, respectively. It can be also seen that, the refracted wave is in the same side with respect to the incident wave, disobeying to the Snell's law, meaning that we have here a negative refraction effect.

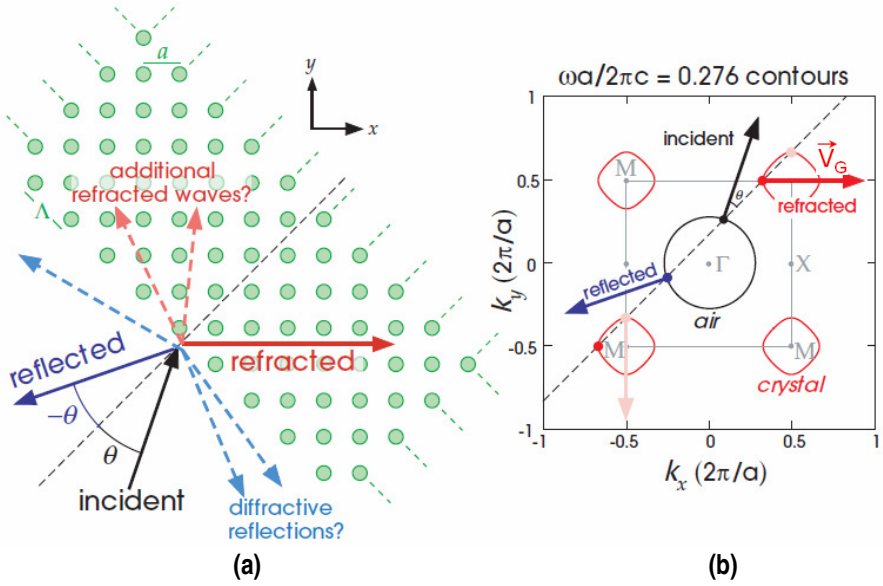

Figure 1.5: (a) Schematic of light propagation (reflection and refraction) when injecting an incident plane wave into a square lattice photonic crystal rotated by 45°. (b) With the condition of conservation of the wave-vector component parallel to the interface, the reflected and refracted waves are determined by two vectors normal to the iso-frequency contour in the homogeneous medium and EFS in the photonic crystal medium, respectively.

Due to the periodicity of photonic crystals, the incident beam will excite reflected and transmitted waves with parallel wavevectors of the form $k_{//} + p.2\pi/\Lambda$, where Λ is the periodicity along the interface of photonic crystal structure and p is an integer. Thus, each incident plane wave of frequency ω with two components of wave-vector $(k_{//}, k_{\perp})$ will yield some reflected and diffracted waves with the same frequency ω, as seen in Fig. 1.5(a).

The shapes of equi-frequency surfaces in photonic crystals is an important characteristic when using the EFS diagram for the study of photonic crystal

properties, and they can be simple or complex depending on the type of photonic crystals, the considered polarization and the given frequency.

For low frequencies in the first photonic band away from the band edge, where the lattice period is much smaller than the wavelength scale, the theorem of effective medium can be applied to study the properties of photonic crystals. In this regime, a photonic crystal structure can be considered as an effective medium with one (or two) effective refractive index (indices), and the EFSs in this range of frequency are centered at the $\Gamma(0,0)$ point. In this range of frequencies, photonic crystals are said to work in the **long-wavelength** $a/\lambda << 1$ (or **homogenizable**) regime.

For frequencies near the band edge or in higher photonic bands, photonic crystal structures can be no more considered simply as effective media. Depending on the curvature of EFSs of these frequencies, one can observe different dispersive phenomena inside PhC structures, as illustrated in Fig. 1.6. The convex (Fig. 1.6(a)) or concave (Fig. 1.6(b)) EFSs can spread the light beam or produce the lensing effect inside photonic crystals, while when working with the EFSs one can conserve the beam width and making an initially divergent beam becoming collimated (Fig. 1.6(c)). Photonic crystals, in this frequency range, are said to work in the **short-wavelength** (or **non-homogenizable**, or **diffraction**) regime.

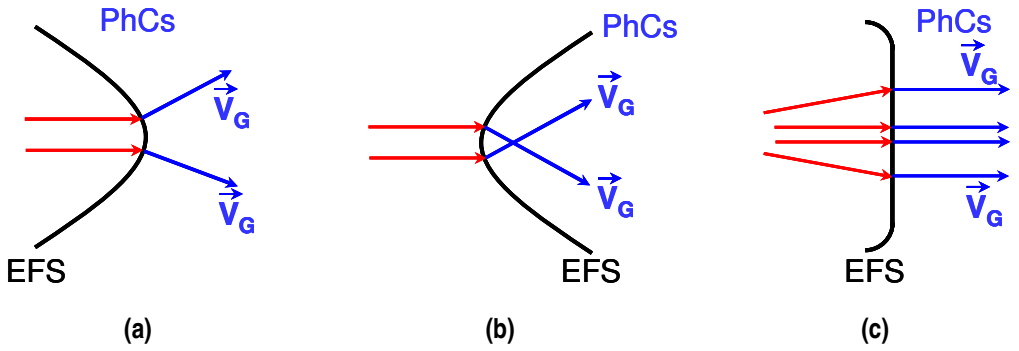

Figure 1.6: EFS curvatures inducing dispersive phenomena in photonic crystals (a), (b) convex and concave EFSs corresponding to negative refraction effect; and (c) flat EFS corresponds to self-collimation effect

These two working regimes will be mentioned in Chapter 2, which presents the adopted methodology for the study of photonic crystals and graded photonic crystals in this thesis. In the following section, some examples on dispersive phenomena in relation with EFSs of photonic crystals will be figured out.

1.1.5. Some examples of dispersion effects in photonic crystals

In these examples as well as in the rest of this thesis, we frequently model the spatial extent of input optical guided modes by Gaussian distributions. It is worth reminding that if a Gaussian beam in the real space has a form:

$$f_{gauss}(x) = \exp\left(\frac{-x^2}{\sigma_x^2}\right) \tag{1.8}$$

where σ_x is the beam waist, then in the reciprocal space, we also have a distribution of wave-vector $\vec{k}$ as a Gaussian function:

$$F_{gauss}(k) = \frac{1}{\sqrt{\pi}\sigma_k}\exp\left(\frac{-k^2}{\sigma_k^2}\right) \tag{1.9}$$

These two equations are presented in Fig. 1.7. Between two parameters σ_x and σ_k we have the uncertainty principle:

$$\sigma_x.\sigma_k = 2 \tag{1.10}$$

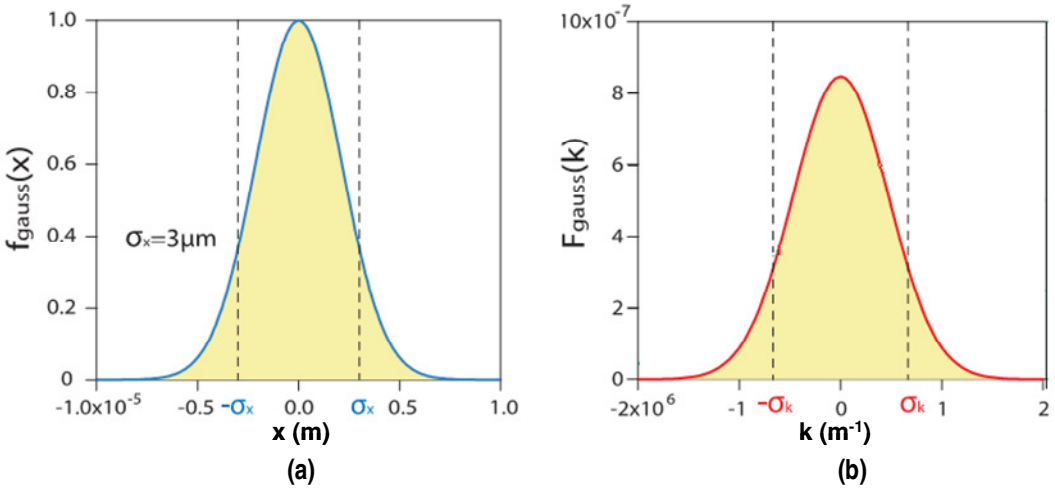

Figure 1.7: (a) Spatial profile of a Gaussian beam with beam waist $\sigma_x = 3\mu m$ and (b) Corresponded spectral profile (wave-vector distribution) of this Gaussian beam.

Eq. 1.10 shows that if a Gaussian beam has a large variance in space, then its transform in reciprocal space has a low variance – the uncertainty principle between the spatial distribution of Gaussian beam and the distribution of wave-vector in reciprocal space. The spectral width of a Gaussian beam is very important for the study of light propagation because it induces the beam divergence. For a Gaussian beam, the angle of divergence is expressed in terms of its beam waist:

$$\theta_0 = \frac{\lambda}{n\pi\sigma_x} \tag{1.11}$$

where λ is the wavelength, and n the refractive index of the medium.

It means that a Gaussian beam may excite a Bloch wave with several values of wave-vector $\vec{k}$ (several values of parallel wave-vectors $k_{//}$) at different angles. This point will be seen in the following examples.

1.1.5.1. Negative refraction

Fig. 1.8 gives an example of the negative refraction effect inside a two-dimensional square lattice photonic crystal structure made of air holes ($a = 300nm$, $n_{air} = 1$, $r_{air-hole} = 92.5nm$) embedded in dielectric host material ($n_{host-material} = 3.03$). The lattice is rotated by 45°, with an interface along the $\Gamma - M$ direction. EFS diagram of the first TE band is presented in Fig. 1.8(a). It can be seen in the figure that near the edge of the first Brillouin zone, a frequency $\omega = 0.195$ is used to excite a Bloch wave with wave-vector $k_{0,0}$ and giving the group velocity V_G, leading to a case of negative refraction.

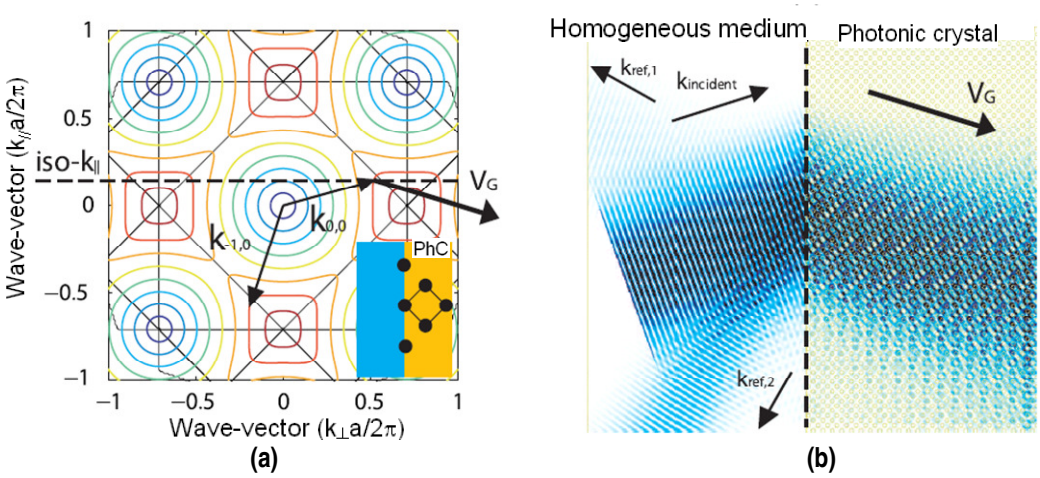

Figure 1.8: Negative refraction effect: (a) Equi-frequency surfaces diagram of a 2D 45°-rotated square lattice photonic crystal made of air holes (periodicity $a = 300nm$, hole radius $r = 92.5nm$) in dielectric ($n = 3.03$) host material. The conservation of parallel wave-vector gives an excitation of a Bloch wave corresponding to negative refraction phenomena; and (b) Negative refraction of a light wave ($\lambda = 1540nm$) which is injected from homogeneous medium (air) into the photonic crystal structure with an incident angle of $\theta_i = 20^o$ (two-dimensional FDTD simulation).

Fig. 1.8(b) presents the FDTD simulation result for the considered case. A continuous Gaussian beam is injected into the photonic crystal structure from a homogeneous medium with an incident angle $\theta_i = 20^o$. We can see the negative refraction effect inside the photonic crystal structure and also two reflected waves due to the grating effect at the homogeneous medium-photonic crystal interface, as discussed before.

1.1.5.2. Self-collimation effect

Fig. 1.9 presents a self-collimation effect in a structure of a 2D 45°-rotated square lattice photonic crystal ($a = 300nm$) made of air holes ($r = 92.5nm$) in a dielectric ($n = 3.03$) host material with $\Gamma - M$ interface. An EFS with square shape is

excited by several wave-vectors corresponding to different incident angles. All of the Bloch waves excited by these wave-vectors propagate in the same direction, perpendicular to the interface as seen in Fig 1.9(a). We can see that the self-collimation effect occurs in wave-vector space when the equi-frequency contour is flat (the curvature is zero). The EFS with a zero curvature in this photonic crystal structure has the wavelength $\lambda_{collim} = 1.39\mu m$. The self-collimation phenomenon is illustrated by 2D FDTD simulation presented in Figs. 1.9(b) and 1.9(c).

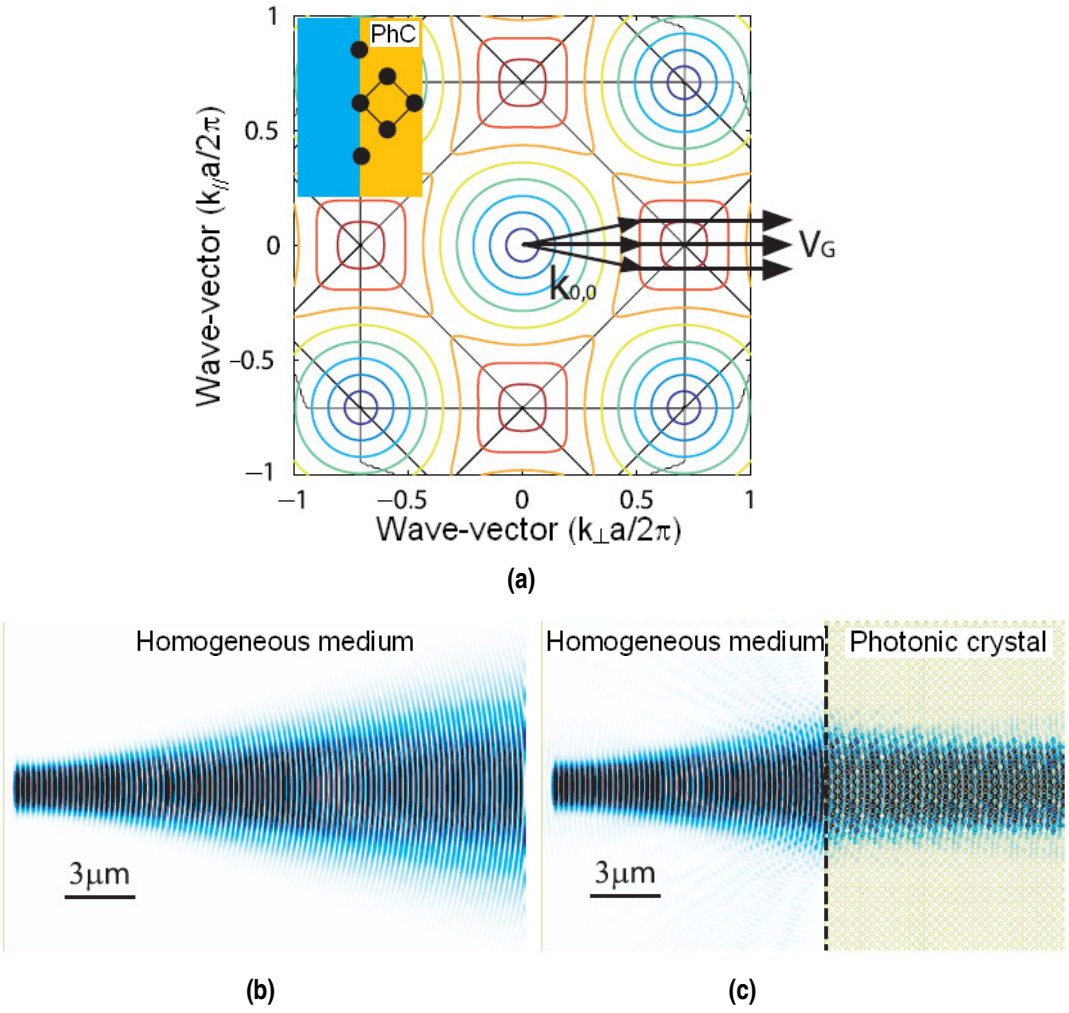

Figure 1.9.: Self-collimation effect: Equi-frequency surfaces diagram of a 2D 45°-rotated square lattice photonic crystal made of air holes (periodicity $a = 300nm$, hole radius $r = 92.5nm$) in dielectric ($n = 3.03$) host material. For a light beam of different incident angles, the conservation of parallel wave-vector $k_{//}$ gives an excitation of some Bloch waves with collinear group velocities; and (c) Electric intensity of a Gaussian beam at collimation wavelength $\lambda_{collim} = 1.39\mu m$ in the homogeneous medium of index $n = 3.03$; and (d) The same Gaussian beam propagates inside the photonic crystal medium without divergence (2D FDTD simulation).

1.1.5.3. Superlensing effect

Fig. 1.10 presents the superlensing effect in a 2D 45°-rotated square lattice photonic crystal ($a = 465nm$) made of air holes ($r = 139.5nm$) in a dielectric host material ($n = 3.03$) with $\Gamma - M$ interface.

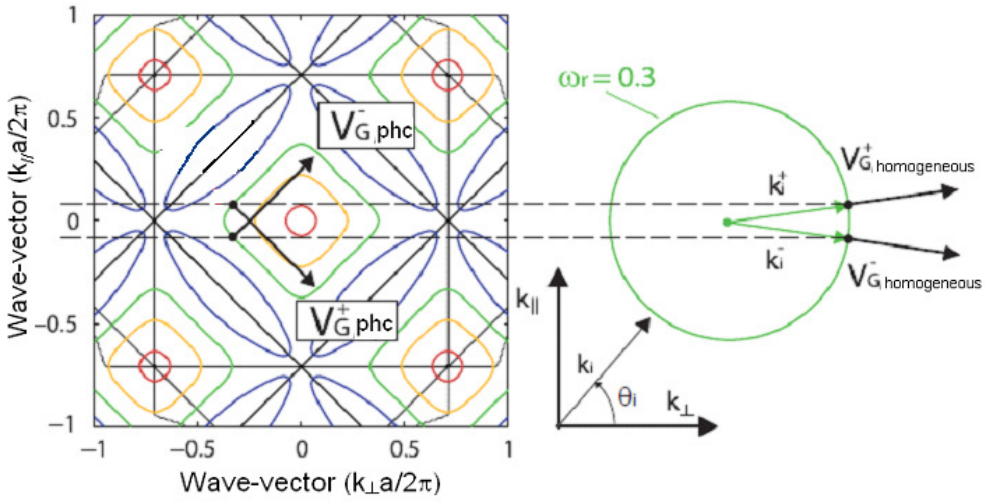

(a)

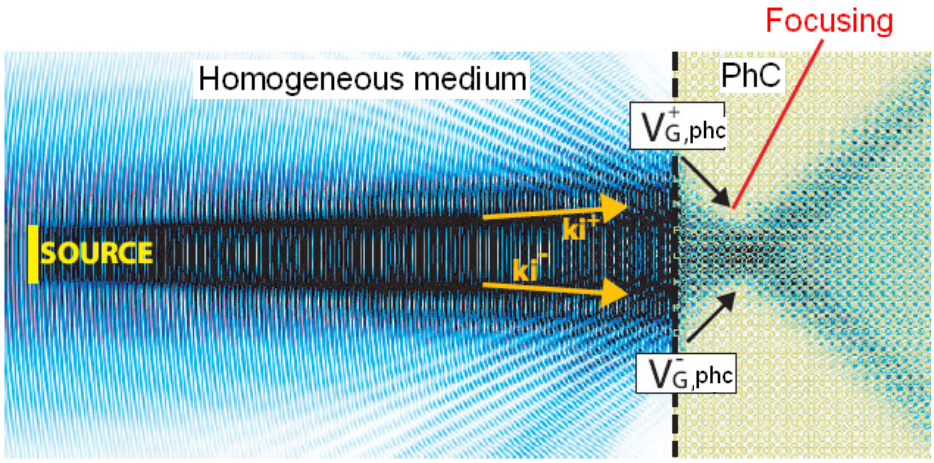

(b)

Figure 1.10: Superlensing effect: (a) Equi-frequency surfaces diagram of the second TE band of a 2D 45°-rotated square lattice photonic crystal $a = 465nm$ made of air holes $r = 139.5nm$ in dielectric $n = 3.03$ host material. One plane wave of wave-vector k_i^+ (positive incident angle $\theta_i > 0$) excites one Bloch wave of group velocity V_G^+ to propagate at negative angle $\theta_{phc} < 0$; and (b) Intensity of electric field of a continuous beam with focusing wavelength $\lambda_{focus} = 1.55\mu m$ which is divergent before propagating inside the considered photonic crystal structure

A divergent source of frequency $\omega = 0.3$ (in the second TE band) in the homogeneous medium is represented by two incident wave-vectors k_i^+ and k_i^-.

When propagating in the homogeneous medium, these two waves propagate

with V_G^+ and V_G^- group velocities. At the interface between the two (the homogeneous and the PhC) media, the wave with wave-vector k_i^+ is coupled with the Bloch wave of group velocity $V_{G,\varphi}^+$ so the group velocity is directed towards negative $k_{//}$ (negative refraction). The Bloch wave $V_{G,\varphi}^-$ and the wave of wave-vector k_i^- have symmetric behaviours. These two Bloch waves have the propagation directions as illustrated in Fig 1.10(a).

The superlensing effect in the considered photonic crystal structure is illustrated in Fig. 1.10(b). A Gaussian source with wavelength $1.55\mu m$ and beam width $2.5\mu m$ in a homogeneous medium with an index $n = 3.03$ is injected into the photonic crystal structure. It can be seen that the group velocities in the photonic crystal medium are much more anglularly separated than in the homogeneous medium and the focusing point of the beam in the photonic crystal is much closer to the interface in comparison with the source in the homogeneous medium.

1.1.5.4. Superprism effect

In certain cases, the refraction angle is largely tuned with a small variation of incident angle or of light frequency. We call this phenomenon the super-angular (or frequency) dispersion, or the superprism effect [2-5]. In general, the superprism effect occurs when a strong curvature zone of equi-frequency surface is excited. A variation of incident angle generates the variation of parallel wave-vector. The strong curvature of equi-frequency surfaces induces a strong variation of the group velocities which are normal to these equi-frequency surfaces, resulting in a strong variation of the overall propagation direction of light.

Fig. 1.11 shows an example of the frequency superprism effect in a 2D square lattice photonic crystal made of air holes with a $\Gamma - M$ interface. The first TE band is excited at several frequencies with an incident angle of 15^o. When the conservation condition of parallel wave-vector $k_{//}$ is satisfied, a line in the Bloch wave space is excited (Fig. 1.11(a)). At the border of the Brillouin zone, EFSs have curvature such that refraction angle can be strongly varied from $\theta_1 = 15°$ to $\theta_2 = -90°$ with frequency increase from $\omega_1 = 0.17$ to $\omega_1 = 0.22$ as seen in Fig. 1.11(b).

Fig. 1.11(c) and 1.11(d) present the field intensity of a $8\mu m$-width beam propagating in the considered photonic crystal structure at the two wavelengths $\lambda_1 = 1.5\mu m$ and $\lambda_2 = 1.41\mu m$, showing the frequency superprism effect. The light beam with wavelength $\lambda_1 = 1.5\mu m$ is refracted inside the photonic crystal structure with an angle of -5° while the light with wavelength $\lambda_2 = 1.41\mu m$ propagates at refractive angle of -45°. The beam is more spreading for the shorter wavelength $\lambda_2 = 1.41\mu m$. This effect can be explained by the fact that the excited zone of the EFS of the wavelength $\lambda_1 = 1.5\mu m$ is flatter than the one obtained for the wavelength $\lambda_2 = 1.41\mu m$.

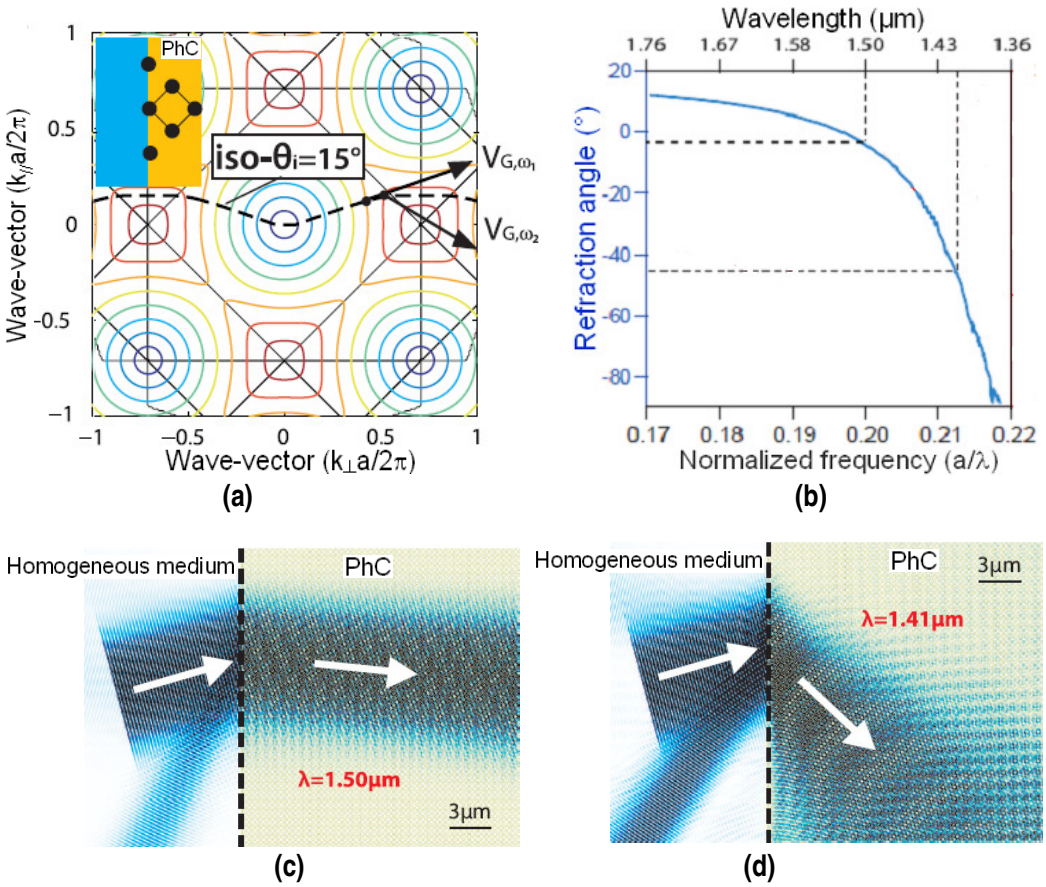

Figure 1.11: Superprism effect: (a) Equi-frequency surfaces of a 2D 45°-rotated square lattice photonic crystal ($a = 300nm$) made of air hole $r = 92.5nm$ in dielectric host material $n = 3.03$. Wave-vector space k excited by a source of incident angle $-15°$ and the variation of frequency is indicated by doted line; (b) Refraction angle as function of frequency; (c) Refraction of a Gaussian beam at wavelength $1.5\mu m$, beam width $8\mu m$ in the considered photonic crystal structure. As can be seen in (b), refraction angle is lightly negative with an angle of $-5°$. (d) Refraction angle of a Gaussian beam (as in (c)) at wavelength $1.41\mu m$, refraction angle is around $-45°$.

The strong beam spreading effect that can be seen in Fig. 1.11(d) is typically what we would like to circumvent. We will come back on this point later in the manuscript.

1.2. Planar two dimensional photonic crystals

Because of the infinite size in the vertical direction, two dimensional photonic crystals are not physical objects to be used in practice. In order to be used in integrated circuits with light coupling from a slab waveguide, they are implemented as planar two dimensional photonic crystals in which the 2D-PhCs are sandwiched betweens layers of materials with lower refractive indices: for example a SiO_2 buried oxide layer as the optical substrate and air (or SiO_2) as the superstrate, as illustrated in Fig.1.12. Since the average index in the slab waveguide core is higher than that in the

two cladding layers of lower refractive indices, light is confined in the direction without periodicity (vertical direction) by total internal reflection.

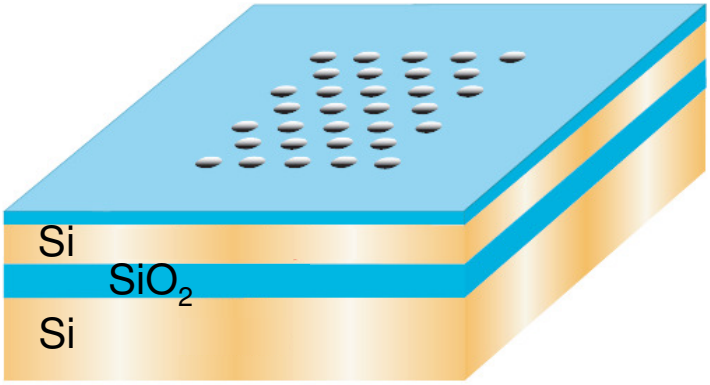

Figure 1.12: Schematic picture of a planar two-dimensional photonic crystal fabricated in a silicon slab waveguide.

Fig.1.13 presents the TE band diagram of a planar 2D square lattice PhC made of air holes ($r/a=0.3$) in a SOI wafer ($n_{Si}=3.45$, $n_{SiO_2}=1.45$) together with the light line, which is defined by $\omega = ck/n_{cladding}$. The region that is above the light line is called the light cone. It corresponds to the frequency region where the modes are not confined in the slab but can escape vertically and introduce intrinsic losses. Below the light line, modes are well confined and guided in the planar 2D-PhC structure; thus we will mainly consider these modes in the following of the manuscript.

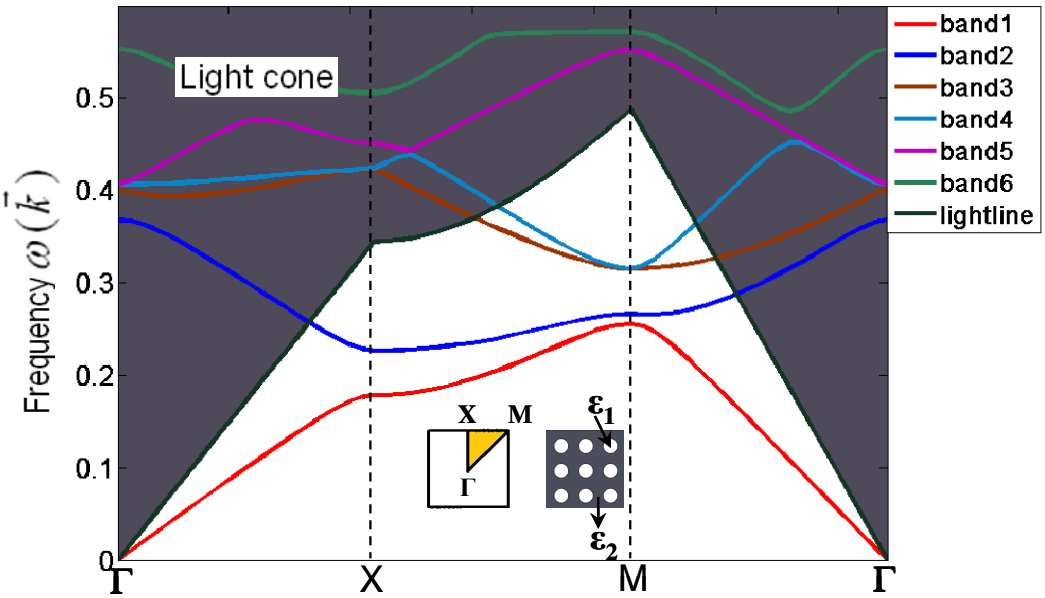

Figure 1.13: TE band diagram of a planar 2D square lattice photonic crystal made of air holes $r=0.3a$ on SOI wafer. Light line is define by $\omega = ck/n_{SiO_2}$. The region above the light line is called the light cone. Below the light line, modes are well confined.

In this thesis, silicon on insulator (SOI) 2D planar PhCs are considered in all cases from simulations to fabrications. The reason of choosing this is that silicon has a high refractive index contrast relative to both air (on top) and silica (SiO_2 – at the bottom); thus, light modes are well confined. Moreover, the fabrication of planar 2D-PhCs on SOI is CMOS compatible and can be done based on a developed and controllable fabrication platform.

1.3. Introduction to Graded Photonic Crystals

1.3.1. Introduction

Manipulating electromagnetic waves at optical frequencies has become a topic of strong interest in some years. It is motivated by the purpose of exploiting original electromagnetic phenomena, easing the fabrication, reducing the losses, and the possibility of integrating several optical functions onto one single device. The use of metamaterials [6-10] coupled with the formalism of transformation optics have shown the possibility to mold the flow of electromagnetic waves in almost arbitray shape waveguiding structures or in cloaking configurations [11-15]. However, at optical frequencies, the use of this method faces several challenges [16]. First of all, strongly anisotropic metamaterials with complicated permittivities and permeabilities are needed, while the potential benefit brought by the use of photonic metamaterials is mitigated by the strong optical losses induced by the use of metals. For this reason, experimental results have only been obtained by reducing the target to the use of broadband all-dielectric structures [17, 18]. This resulted in the use of sub-wavelength dielectric structures to control the local average refractive index of planar optical waveguides. It is interesting to work in these conditions and then obtain a broadband operation meaning working in the long-wavelength regime, but this is not the choice that was retained in the present PhD thesis.

To work in the diffraction regime, photonic crystals are also a possible approach. As presented in the previous section, the dispersion properties of photonic crystals can be used for the manipulation of light. The anisotropy of the dispersive bands and their sensitivity to frequency can enhance light deflection inside PhCs.

In the homogenizable (long-wavelength) regime mentioned above, gradual structures are used for the purpose of manipulating light. In order to work in the diffraction (short-wavelength) regime, we need to increase the frequency $\omega = a/\lambda$. The structure in this case is no more presented as a gradual map of index but a gradual map of band structure (EFSs). We can achieve this by introducing a modulation of the PhC lattice parameters. The result is called a graded photonic crystal (GPhC). It was proposed in [6, 19, 20]. The understanding of controlling light in graded photonic crystals in most cases can be explained relying on the fact that the modulation of lattice parameters results in the change of the band diagram, giving a deformation of EFSs.

There are many degrees of freedom to define GPhC structures by modulating the lattice parameters: the **aspect ratio** between two basis vectors $\vec{a}_1$ and $\vec{a}_2$ of the lattice, the **angle** $\theta_{lattice}$ between these two vectors $(\vec{a}_1, \vec{a}_2)$, and the **size (filling factor)** (or even the **shape**) of scattering elements. Fig. 1.14 shows an example of a

graded photonic crystal medium consisting of a spatial variation of the hole filling factor in a triangular lattice photonic crystal.

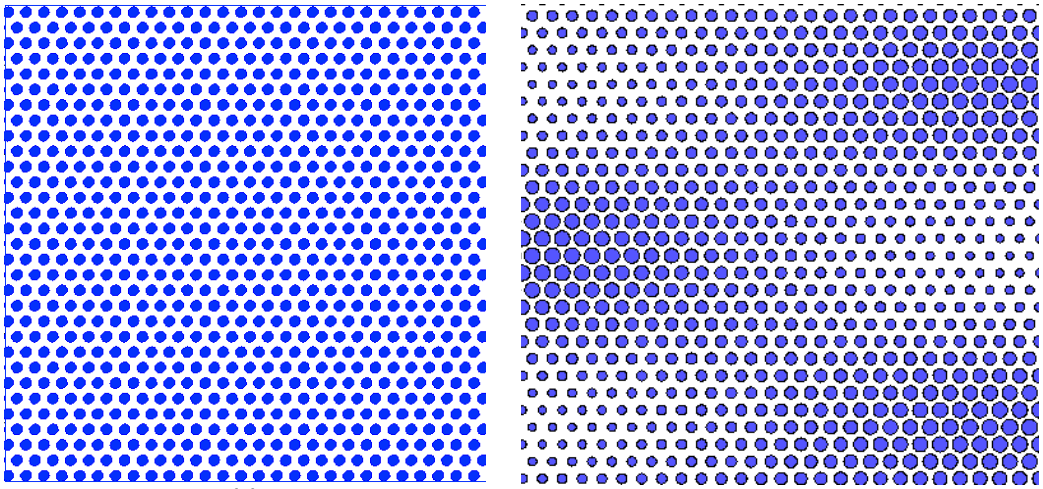

Figure 1.14: (a) Triangular lattice photonic crystal ($|\vec{a}_1| = |\vec{a}_2| = a$; $\theta_{lattice} = (\vec{a}_1, \vec{a}_2) = 60^0$; $r/a = 0.3$) and (b) a graded photonic crystal medium made of triangular lattice photonic crystal with a profile of filling factor $r/a = f(x, y)$

In this thesis, we aim at investigating the deformation of EFSs by changing lattice parameters and then propose a methodology for the study of GPhCs properties for the control of electromagnetic waves at optical wavelengths. For this, different photonic crystals made with a large set of different parameter values have been considered for the calculation of dispersion surfaces and for the observation of EFS deformations, which is worth for the studies of all the rest of this thesis. In the following sections, we will present some representative examples related to the deformations of EFSs.

1.3.2. Equi-frequency surface deformations

As just pointed out above, we will briefly introduce in this section some examples of EFS deformations as a function of lattice parameter changes to have an overview on the study of GPhCs which will be discussed in detail in forthcoming sections and chapters.

1.3.2.1. Equi-frequency surface deformations by changing the angle between the two primitive lattice vectors

We first begin by the observation of EFS diagrams of two common 2D photonic crystal lattices: the square and the triangular lattices made of air holes in a SOI wafer.

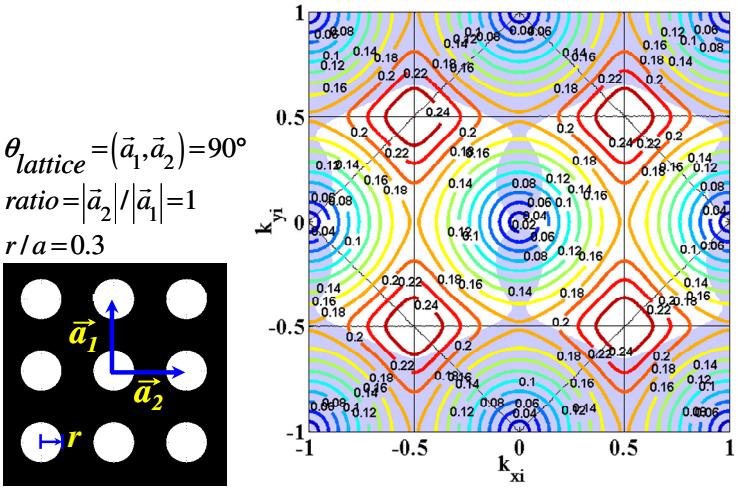

Figure 1.15: EFS diagrams of the first TE band of two 2D photonic crystal lattices: (a) the square and (b) the triangular made of air holes ($r/a = 0.3$) on SOI wafer ($n_{Si} = 3.45$, $n_{SiO_2} = 1.45$).

The EFS diagrams of the first TE band of the two 2D photonic crystal lattices are presented in Fig. 1.15 with their dielectric maps in real lattice. We can see that, for low frequencies, the EFSs of these two lattices are quite similar, having circle shapes and centered at the Γ point. Near the band edge (the edge of the first Brillouin zone), their EFSs are centered at high symmetric point (M for square lattice and K for triangular lattice), yet, their shapes are different.

Between these two considered photonic crystal lattices, the only different parameter is the angle $\theta_{lattice} = (\vec{a}_1, \vec{a}_2)$ between the two primitive lattice vectors.

Now, we introduce some chirps on the lattice parameters of photonic crystal lattices to have a qualitative insight to the deformation of EFSs that is the key point for the study of graded photonic crystals – the main topic of this thesis.

First of all, let us imagine that we are able to generate a GPhC medium by chirping the $\theta_{lattice}$ parameter from 45° to 90°.

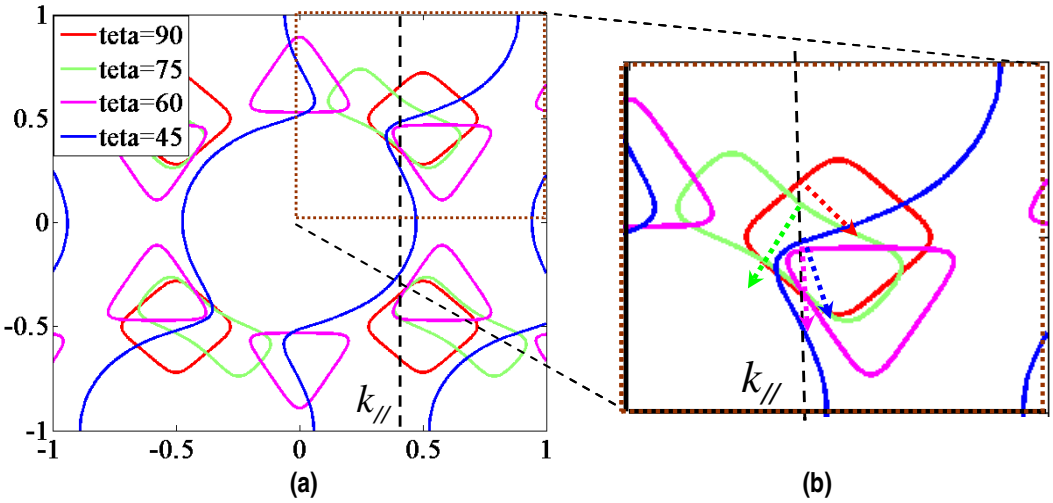

Figure 1.16: (a) Equi-frequency surfaces (EFSs) of different lattices: the square lattice $\theta_{lattice} = 90°$, the 75°-lattice $\theta_{lattice} = 75°$, the triangular lattice $\theta_{lattice} = 60°$, and the 45°-lattice $\theta_{lattice} = 45°$ and at frequency $\omega = 0.22$. Other parameters ($ratio = |\vec{a}_1| / |\vec{a}_2| = 1$; $r/a = 0.3$) are the same for these lattices. (b) Group velocities of light waves at this frequency in these photonic crystal lattices.

Fig. 1.16(a) shows the EFSs of four photonic crystal lattices: square lattice ($\theta_{lattice} = 90°$), 75°-lattice ($\theta_{lattice} = 75°$), triangular lattice ($\theta_{lattice} = 60°$), and 45°-lattice ($\theta_{lattice} = 45°$) at frequency $\omega = 0.22$. Changing the angle $\theta_{lattice}$ between the two primitive lattice vectors from 45° to 90°, it can clearly be seen that EFSs have a huge modification. Assuming that a Bloch wave propagates in these photonic crystals excited by this frequency with a parallel wave-vector $k_{//}$, because of the large differences among these EFSs, the directions of Bloch modes defined by the group velocities can be different by nearly 75°, as seen in Fig. 1.16(b).

1.3.2.2. Equi-frequency surface deformations by changing the aspect ratio between the two primitive lattice vectors

Considering a modification of the lattice ratio of a rectangular lattice, Fig. 1.17 illustrates the EFS deformations at frequency $\omega = 0.23$ of rectangular lattices (with aspect ratios of 1; 1.05; 1.1 and 1.2). The shapes of EFSs in this case are not much different, but their sizes and their centers are modulated and shifted a lot. The direction of Bloch waves propagating inside GPhCs made by these photonic crystal lattices can be bended by 90° as presented in Fig. 1.17(b).

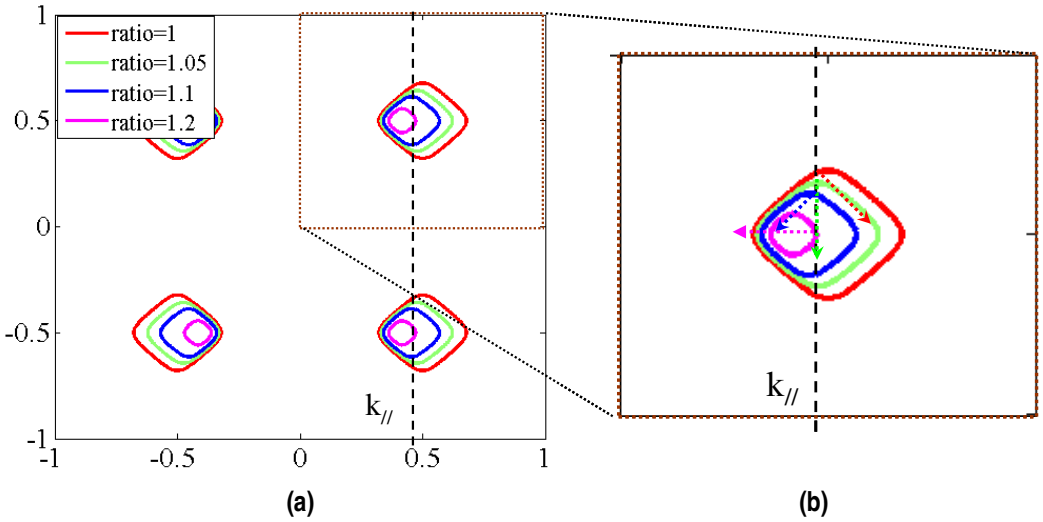

Figure 1.17: (a) Equi-frequency contours (EFSs) at frequency $\omega = 0.23$ of rectangular lattices with **aspect ratio** of 1(square lattice); 1.05; 1.1 and 1.2. Other parameters ($\theta_{lattice} = 90^o$; $r/a = 0.3$) are the same for these lattices; and (b) Group velocities of light wave at this frequency in these photonic crystal lattices.

1.3.2.3. Equi-frequency surface deformations by the gradient of photonic crystal filling factor

Now let's consider the square lattice photonic crystal structure made of air holes with a filling factor chirp $r/a = 0.2; 0.25; 0.3; 0.35$. Making such a variation, we can also get a deformation of EFSs, as presented in Fig. 1.18 for the frequency $\omega = 0.24$.

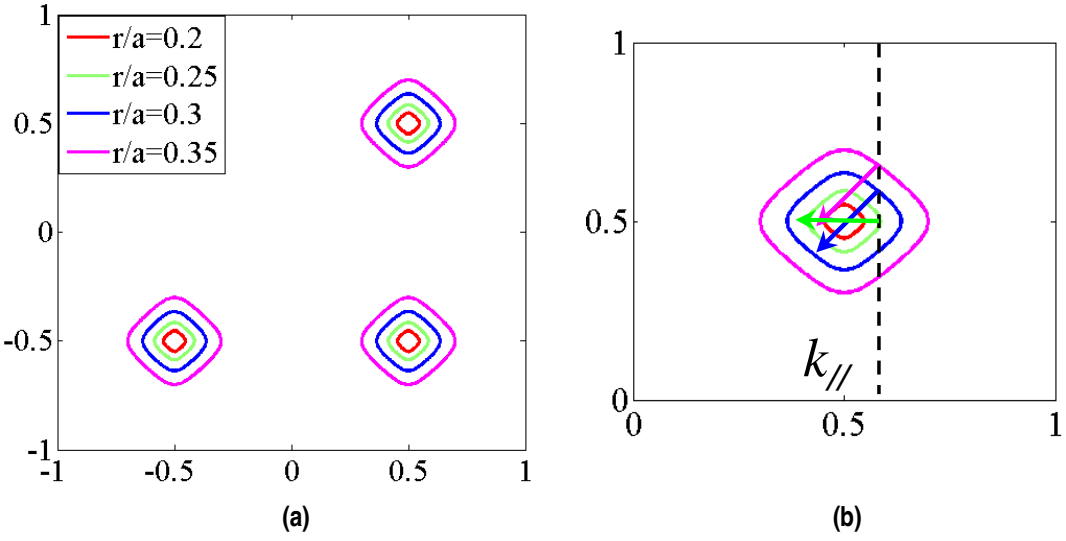

Figure 1.18: (a) Equi-frequency contours at frequency $\omega = 0.24$ of square lattice with different air holes radius r/a=0.2; 0.25; 0.3 and 0.35. Other parameters ($ratio = |\vec{a}_1|/|\vec{a}_2| = 1$; $\theta_{lattice} = 90^o$) are the same for these lattices; and (b) Group velocities of light wave at this frequency in these photonic crystal lattices.

The air hole radius is varied from 0.2 to 0.35, resulting in a modulation of EFFs size with a small change in the shape and without changing the center of them. We can see that, in comparison with the two former cases, the lattice change is simpler, the deformation of EFSs is smaller. However, we still get a large difference on direction of Bloch waves excited in GPhCs medium made with a gradient of filling factor.

This case will be considered to generate the graded photonic crystals used for the study of this thesis, which will be presented in the following chapters.

1.4 Conclusion

In this chapter, we have presented the general concepts related to planar two-dimensional photonic crystals and graded photonic crystals and some dispersive phenomena in 2D photonic crystals. We see the rich variety of dispersive effects in connection with the equi-frequency surface shapes in PhCs. We also see the rich variety of EFS deformations that we can have with GPhCs. And it is possible to combine them for the study of molding the flow of light using graded photonic crystals mainly working in the diffraction regime.

At the beginning of my PhD work, GPhCs were proposed by [6, 19-21], especially with a 1D-chirp (lattice periodicity in one dimension), and there was no experimental demonstration of the predicted phenomena at optical frequencies. In this thesis, we have chosen a simple configuration (*square lattice, variable filling factor, working at in the first band*) with the aim to demonstrate the light bending (mirage) effect with 2D-chirps of one lattice parameter (modulation of filling factor in x-y space), the possibility to use dispersive phenomena in GPhCs, and start out the exploration of the issues related to the light polarization in GPhCs. These points will be developed in forthcoming chapters.

We begin first in Chapter 2 by describing the method that we relied on for the study of light propagation in GPhC structures.

Chapter 2

Hamiltonian optics-assisted ray tracing in graded photonic crystals using the local photonic bandstructure

This chapter aims at presenting a simple modal approach for the study of light propagation in graded photonic crystals (GPhCs) focusing on GPhCs mainly operating in the diffraction regime.

In principle, artificial optical materials can be studied by using the formalism of transformation optics [13, 17, 18]. This method either requires a precise control of the electric permittivity and magnetic permeability or an appropriate choice of the chosen coordinate transformation. Using this method, studied devices usually work with a broadband operation without sensitivity to wavelength. For the study of light propagation in GPhCs, it is also possible to use the Finite-Difference Time-Domain (FDTD) method. Yet, it is applicable only for the validation but not for the prediction of light propagation in GPhCs.

The method of Hamiltonian optics ray propagation has been proposed for the study of non-uniform photonic crystal structures in [6, 19], the so-called Hamiltonian being related to the local dispersion relationship of the graded photonic crystal. We have adopted this approach in the present thesis.

In this chapter, the principle of Hamiltonian optics will firstly be described. The use of Hamiltonian method for the study of GPhCs is considered for two different regimes: the homogenizable regime and the diffraction one. Since the Hamiltonian is related to the dispersion relationship of GPhCs, in applying this method, it is convenient to have an analytical expression of EFSs as a function of varied lattice parameters. The extraction of EFSs of one particular case of square photonic crystal with a varying filling factor profile will be presented as an example. Then, a configuration of GPhC is proposed to be studied by the method of Hamiltonian optics and then to be compared with results obtained using FDTD simulation.

2.1. General principle of Hamiltonian optics

Hamiltonian optics is a semi-analytical approach that can be applied for the study of light propagation inside inhomogeneous structures with slowly spatially varying parameters, meaning that the local dispersion relation is known. Using this method, light propagation can be described through the two following Hamiltonian's equations:

$$\begin{aligned} \frac{d\boldsymbol{r}}{d\sigma} &= \nabla_k H = grad_k\left(H(\boldsymbol{k},\boldsymbol{r})\right) \\ \frac{d\boldsymbol{k}}{d\sigma} &= -\nabla_r H = -grad_r\left(H(\boldsymbol{k},\boldsymbol{r})\right) \end{aligned} \tag{2.1}$$

where $\boldsymbol{r}$ is the position in space, $\boldsymbol{k}$ the wave-vector and σ is a quantity related to time, and $H(\boldsymbol{k},\boldsymbol{r})$ is the local Hamiltonian in $(\boldsymbol{k},\boldsymbol{r})$ space.

It can be seen from the first equation in Eq. (2.1) that the optical light path is directed along the group 'velocity' $grad_k\left(H\left(\boldsymbol{k},\boldsymbol{r}\right)\right)$. Using this method, a slow varying inhomogeneous structure can be considered more or less as a continuous set of different media between which the parallel wave-vector is naturally matched at each interface. This is the meaning of the second equation in Eq. (2.1). An implicit hypothesis in applying the method of Hamiltonian optics is that the special gradient is supposed to be slow enough, so that light properties like group velocity can be locally defined. The first Hamiltonian's equation in (2.1) can be rewritten in Newtonian form by taking the second order of the differential of the position $\boldsymbol{r}$ in related to the 'time' parameter σ:

$$\frac{d^2\boldsymbol{r}}{d\sigma^2} = \left[\nabla_k \nabla_k H\right] : \left(-\nabla_r H\right) = \left[1/m^*\right] : \boldsymbol{F} \tag{2.2}$$

or:

$$\left(-\nabla_r H\right) = \boldsymbol{F} = m^* \frac{d^2\boldsymbol{r}}{d\sigma^2} \tag{2.3}$$

where the reciprocal effective mass tensor $\left[1/m^*\right]$ depends on the position in real and reciprocal spaces. This shows that Eq. (2.2) is an equation of motion in which the gradient of Hamiltonian H is equivalent to a force $\boldsymbol{F}$ acting on ray path [19, 22].

The Hamiltonian *H* is related to the dispersion relation of the studied structure, particularly the photonic band structure in case of photonic crystal media. An important question is the relation between *H* and $\omega(\boldsymbol{k})$. It should be noted that the structure in GPhCs changes point by point, meaning that the photonic band structure depends on the position; $\omega(\boldsymbol{k})$ thus becomes $\omega(\boldsymbol{k},\boldsymbol{r})$. From Eq. (2.1), it is shown that the light propagation ensures:

$$\begin{aligned} dH &= grad_k\left(H\right).d\boldsymbol{k} + grad_r\left(H\right).d\boldsymbol{r} \\ &= \frac{d\boldsymbol{r}}{d\sigma}.d\boldsymbol{k} - \frac{d\boldsymbol{k}}{d\sigma}.d\boldsymbol{r} = 0 \end{aligned} \tag{2.4}$$

Eq. (2.4) shows that the Hamiltonian H is constant and that if we want to use the Hamiltonian optics method to describe light propagation at a given frequency ω, we need to choose the Hamiltonian H related to ω in such a way that $dH=0$ implies $d\omega=0$. Thus, the main point in applying this method is to know the photonic band structure $\omega(\boldsymbol{k},\boldsymbol{r})$ and to choose a proper Hamiltonian H related to $\omega(\boldsymbol{k},\boldsymbol{r})$. This problem is presented in the next section.

2.2. Hamiltonian optics for graded photonic crystals

As mentioned in Chapter 1, light propagation in photonic crystal structures can be classified into two regimes:

- **the long-wavelength regime** (homogeneous regime) where the wavelength of propagating light is much larger than the lattice periodicity ($a/\lambda \ll 1$) usually met for low frequencies of the first photonic band; and,
- **the short-wavelength regime** (diffraction regime) in which $a/\lambda > 0.2$ (typically), corresponding to frequencies near the first band edge or at higher photonic band.

For the study of light propagation in graded photonic crystals using the method of Hamiltonian optics, we consider these two regimes just hereafter.

2.2.1. Hamiltonian optics for graded photonic crystals operating in the homogeneous regime

In the homogeneous regime, the periodicity of photonic crystals does not have an important role and a graded photonic crystal can be presented as an effective (gradual) medium in space with a distribution of average refractive index $n(x,y)$. The local band structure at each point of the gradual medium is given by:

$$|\boldsymbol{k}| = \sqrt{k_x^2 + k_y^2} = n(x,y)\frac{\omega}{c} \tag{2.5}$$

where k_x and k_y are the two components of the wave-vector $\boldsymbol{k}$, $n(x,y)$ is the local average effective index, ω the light frequency, and c the speed of light in vacuum.

Fig. 2.1 shows the schematic picture of problem under consideration in which the light path is being known through a parametric curve $[x(\sigma), y(\sigma)]$ and the question is how we can modulate the average refractive index $n(x,y)$ of the gradual medium to support this given light path. Solving this problem is somehow similar to the one using the transformation optics approach for the design of photonic metamaterials working at optical frequencies [18]. The main common point of these two approaches is that a refractive index map is required to be designed appropriately to control the light propagation.

To apply the Hamiltonian optics method on manipulating light in a gradual homogenizable medium, there are several possible choices for the Hamiltonian H in

relation with the local band structure $\omega(\boldsymbol{k})$. It can be straightforwardly chosen $H=\omega(\boldsymbol{k})$ because if $d\omega=0$ then $dH=0$. However, this is not a convenient choice in most cases, since the calculation and combining of the partial differentials of $H\left(=\omega(\boldsymbol{k})\right)$ is not easy. Another choice for H can be:

$$H=\frac{\omega^2}{c^2}=\frac{k_x^2+k_y^2}{n^2(x,y)} \tag{2.6}$$

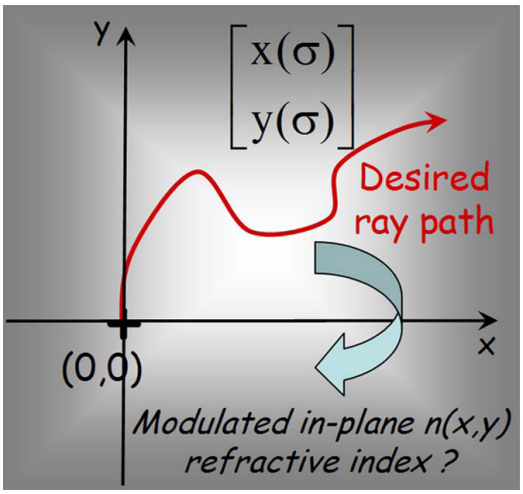

Figure 2.1: Schematic picture of the problem under consideration: light path being known through a parametric curve $\left[x(\sigma),y(\sigma)\right]$; Hamiltonian optics propagation is considered to derive the required in-plane refractive index distribution $n(x,y)$.

Given this choice, equation (2.1) becomes:

$$\begin{aligned}\frac{dx}{d\sigma}&=\frac{\partial H}{\partial k_x}=\frac{2k_x}{n^2(x,y)}\\ \frac{dy}{d\sigma}&=\frac{\partial H}{\partial k_x}=\frac{2k_y}{n^2(x,y)}\end{aligned} \tag{2.7a}$$

$$\begin{aligned}\frac{dk_x}{d\sigma}&=-\frac{\partial H}{\partial x}=2\frac{\partial n(x,y)}{\partial x}\left(k_x{}^2+k_y{}^2\right)\frac{1}{n^3(x,y)}\\ \frac{dk_y}{d\sigma}&=-\frac{\partial H}{\partial y}=2\frac{\partial n(x,y)}{\partial y}\left(k_x{}^2+k_y{}^2\right)\frac{1}{n^3(x,y)}\end{aligned} \tag{2.7b}$$

For a given light path $\left[x(\sigma),y(\sigma)\right]$ and the in-plane refractive index profile $n(x,y)$, the relationship (2.7a) can be reformulated as:

$$k_x = \frac{n^2(x,y)}{2}\frac{dx}{d\sigma}$$
$$k_y = \frac{n^2(x,y)}{2}\frac{dy}{d\sigma} \qquad (2.8)$$

These expressions show that the wave-vector $k = (k_x, k_y)$ along light path has to follow a prescription given by the group velocity-like $\boldsymbol{V}_G = (dx/d\sigma, dy/d\sigma)$. At the same time, the variation of the local wave-vector $(dk_x/d\sigma, dk_y/d\sigma)$ values have to be consistent with the tangential wave-vector conservation law, i.e. must obey to relationships (2.7b).

Eliminating k_x and k_y in the two sides of (2.7b) using equation (2.8) gives the final following result:

$$\frac{\partial \ln(n(x,y))}{\partial x} = \frac{\frac{d^2x(\sigma)}{d\sigma^2}}{\left(\frac{dx(\sigma)}{d\sigma}\right)^2 + \left(\frac{dy(\sigma)}{d\sigma}\right)^2}$$
$$\frac{\partial \ln(n(x,y))}{\partial y} = \frac{\frac{d^2y(\sigma)}{d\sigma^2}}{\left(\frac{dx(\sigma)}{d\sigma}\right)^2 + \left(\frac{dy(\sigma)}{d\sigma}\right)^2} \qquad (2.9)$$

Equation (2.9) is a direct formulation of the required bi-dimensional refractive index distribution to make light follow a prescribed trajectory [23]. Contrary to other approaches making use of numerical calculations, an analytical expression for $n(x,y)$ can be deduced from equation (2.9).

To present the validity of using Hamiltonian optics approach for controlling light in a gradual homogenizable medium, we consider a circular light bending governed by $x(\sigma) = R.\sin(\Omega\sigma)$ and $y(\sigma) = R.\cos(\Omega\sigma)$. Eq. (2.9) then becomes:

$$\frac{\partial \ln(n(x,y))}{\partial x} = -\frac{x}{x^2+y^2}, \quad and \quad \frac{\partial \ln(n(x,y))}{\partial y} = -\frac{y}{x^2+y^2} \qquad (2.10)$$

then the required index map can be given by: $n(x,y) = \frac{C}{\sqrt{x^2+y^2}}$ (2.11)

with C is a constant. This index profile for a circular bending obtained by the Hamiltonian optics approach is exactly the same as the one reported in [VAS-10] by using the method of transformation optics. However, noted that a circle can be described as $x^2 + y^2 = R^2$, then Eq. (2.10) also becomes:

$$\frac{\partial \ln(n(x,y))}{\partial x} = -\frac{x}{R^2}, \quad and \quad \frac{\partial \ln(n(x,y))}{\partial y} = -\frac{y}{R^2} \qquad (2.12)$$

Then, the index profile needed to support the circular bend is:

$$n(x,y) = n_0 . \exp\left(-\frac{x^2 + y^2}{2R^2} \right) \tag{2.13}$$

in which n_0 is a constant index.

This index profile can be approximated by a 2D planar square lattice PhC medium made of circular air holes in which the filling factor f is given by $f=\pi(r/a)^2$; and r is the hole radius and a the PhC lattice parameter on SOI wafer. The air hole radius profile that approximately matches the index profile in Eq. (2.13) is then given by:

$$\frac{r}{a}(x,y) = \sqrt{\frac{1}{\pi} \frac{n_{slab} - n_{slab} . \exp\left(-\frac{x^2 + y^2}{2R^2} \right)}{n_{slab} - n_{hole}}} \tag{2.14}$$

in case of considering a SOI slab PhCs with $n_{slab}=2.95$, the effective refractive index for slab waveguide with a thickness of silicon layer of $260nm$ at wavelength $\lambda = 1,55\mu m$ in TE polarization, and $n_2 = n_{hole} = 1.0$.

Figure 2.2(a) shows the dielectric permittivity of the related square lattice graded photonic crystal structure made of air holes with a radius profile presented in Eq. (2.14) in a SOI slab and for the case $R=40a$. Hole radius is limited to $0.5a$ to prevent overlapping between neighbouring holes. Figure 2.2(b) shows the steady-state field obtained at normalized frequency $a/\lambda=0.13$, meaning a lattice parameter around 200nm for an optical wavelength near $\lambda=1.5\mu m$ ($\approx 7.5a$), when a Gaussian beam with a beam waist of $W_0 = 5a$ is injected into the GPhCs medium. It can be seen from Fig. 2(b) that light is bended by 90° as predicted by the analytical calculation using Hamiltonian optics.

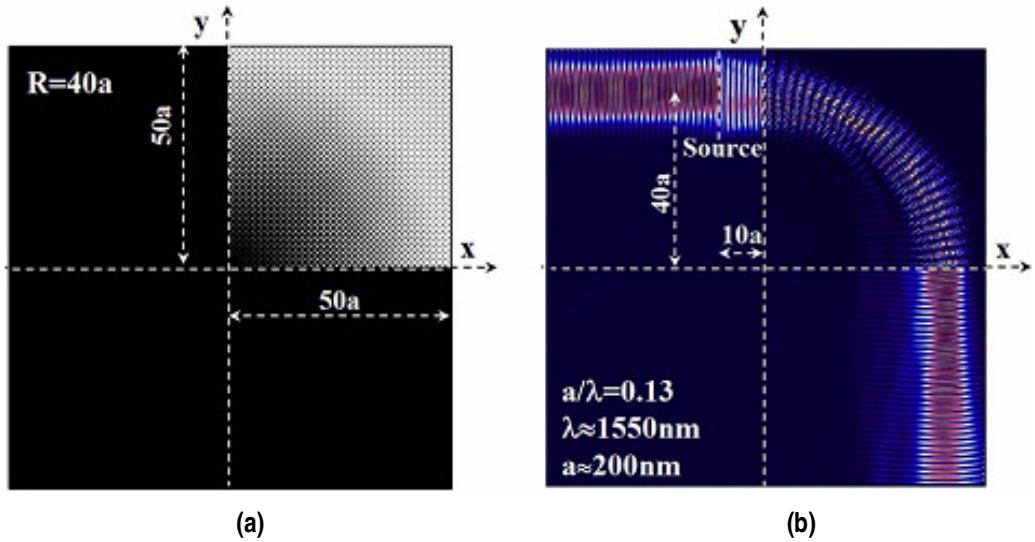

Figure 2.2: (a) Dielectric permittivity diagram and (b) field steady state at frequency $\omega = a / \lambda = 0.13$ the considered 90°-circular-turn graded photonic crystal structure of square lattice made of a filling factor profile presented in Eq. (2.14) (2D FDTD simulation)

A gradual homogenizable medium made by scattering elements with sub-wavelength periodicity makes difficult the practical fabrication if one want to work at optical wavelengths (the periodicity is then normally smaller than *200nm*). Moreover, the in-plane refractive index has no strong dependence with wavelength so that light path will not vary much with the variation of frequency. This gives an advantage of broadband operation, but also a disadvantage since no path sensitivity is obtained. In other words, no benefit is taken from the unusual dispersive effects of periodic media such as superlens, superprism or self-collimation properties.

In this PhD, attention has been thus more focused on GPhCs working mainly in the diffractive regime.

2.2.2. Hamiltonian optics for graded photonic crystals in the diffractive regime

The schematic picture of light propagation inside a perfect periodic medium is given in Fig. 2.3(a), where a light ray of frequency ω is injected into the PhC medium from a homogeneous medium. The condition for light to be coupled into and propagate inside the photonic crystal medium has been discussed in section 1.1.4 of Chapter 1.

The method of Hamiltonian optics can be applied in this case for the description of the propagation of a light ray. However, only the first equation in Eq. 2.1 $d\boldsymbol{r}/d\sigma = \nabla_k H = grad_k\left(H\left(\boldsymbol{k},\boldsymbol{r}\right)\right)$ is used, since the band structure is constant everywhere in a perfectly periodical medium. Then, a light ray has a straight trajectory following the direction of the group velocity of the excited Bloch wave that is normal to the photonic crystal equi-frequency surface at frequency ω, as can be seen in Fig. 2.3(a).

But it is not the case for the propagation of a light ray inside a graded photonic crystal (GPhC) where the photonic band structure spatially varies point by point. It makes varying the local band structure and probably introducing new virtual interfaces, thus making the parallel wavevector $k_{//}$ tuned along the light path. Light path propagating in the GPhC medium can thus be represented in Fig. 2.3(b).

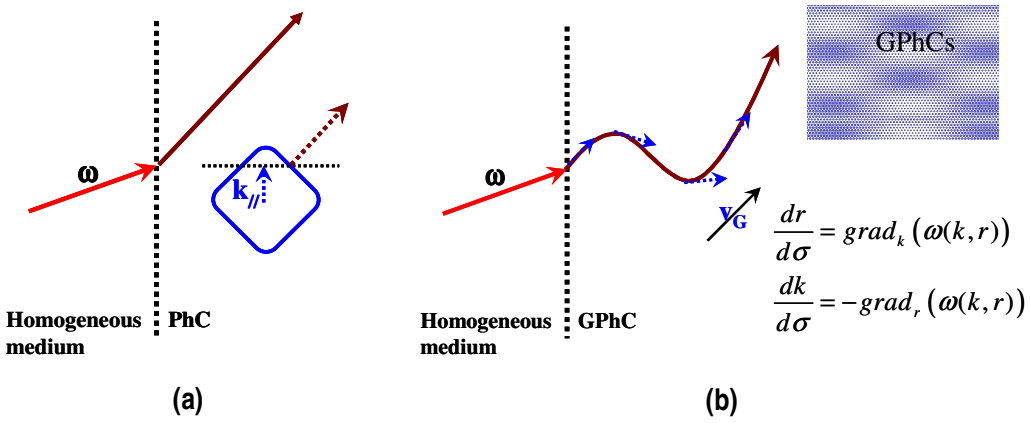

Figure 2.3: Light propagation in (a) periodic structure (photonic crystal) and (b) non-uniform periodic structure (graded photonic crystal)

The first conditions of frequency in the allowed energy band and the matching of parallel wave-vector $k_{//}$ at the interface between the homogeneous medium and GPhC medium are the same as in the PhC case. But since the parallel wave-vector $k_{//}$ is changed along the light path, the group velocity which determines the direction of propagation is then varied too, resulting in a non-straight light path. This shows the possibility of manipulating light propagation inside the GPhC medium "at will" by introducing some variation of PhC parameters.

It was presented in [6] that the Hamiltonian optics method can be applied for the study of light propagation inside non-periodic photonic structures and for the calculation of beam width along the light path. This work relied on a numerical calculation of Bloch wave dispersion relationships locally at each position of the structure and the dispersion relationship being known, Hamiltonian's equations could be used to calculate the beam path or the propagation of a light ray. Yet, the problem of seeking for a gradual photonic crystal medium to support a desired light path was not mentioned.

To try getting the connection between desired light paths and required artificial media using the Hamiltonian approach, it is convenient to define analytically the dispersion relationship $\omega(\boldsymbol{k},\boldsymbol{r})$, or in other words, to have an analytical description of EFSs as a function of varied parameters of the GPhC medium.

2.2.2.1. Calculation of EFSs

To get all EFSs in the reciprocal space of a photonic crystal lattice, first, the band structure is calculated for every point inside the first Brillouin zone. Then, EFSs of one particular frequency can be plotted by projecting the surface of the band diagram on the $\left(k_x, k_y\right)$ space (as seen in Chapter 1). The main question is to find the analytical relationship of the wave-vector $\boldsymbol{k}$ as a function of lattice parameters of that graded photonic crystal structure.

It has been presented in [22] that the analytical calculation of EFSs can be approximately accessible by reducing drastically the number of partial plane waves in the Bloch wave expansion near the photonic crystal band edge. It is necessary to highlight here that this work addressed the calculation of EFSs around the high symmetric point (M point for the square lattice and K point for the triangular lattice) of the first Brillouin zone. Using this method, the dispersion relation has the form:

$$3\delta_y^2 = \left(\delta_x + \vartheta\right)^2 + \frac{2\kappa^2\left(4\kappa - K/\sqrt{3}\right)}{2\delta_x - \vartheta} \tag{2.15}$$

in the case of the triangular lattice photonic crystal and the form of:

$$\delta_y^2 = \delta_x^2 + \left(\vartheta/\sqrt{2}\right)^2 \pm 2\left(\vartheta/\sqrt{2}\right)\sqrt{\delta_x^2 + 2\kappa^2} \tag{2.16}$$

for a square lattice photonic crystal, in which δ_x, δ_y are the displacement of EFS curve (k_x, k_y) from the vertices (M or K points) of the first Brillouin zone, and κ and

ϑ denote the coupling constant and the dephasing constant, respectively, which are related to the average wave-vector $k_0 = n_0 \frac{\omega}{c}$ in the structure and to the lattice vectors.

However, the two parameters κ and ϑ were only qualitatively introduced, giving no strong basis for the design of practical structures.

Another approach can be started directly from the dispersion band structure $\omega(k_x, k_y)$ of photonic crystal geometries obtained by the Plane Wave Expansion method (PWE). With this approach, the analytical expression of EFSs as function of chirped parameters can be achieved in some cases.

2.2.2.2. Analytical extraction of EFSs for one particular case

As mentioned in Chapter 1, there are many degrees of freedom to make vary the lattice parameters of photonic crystal geometries to obtain a GPhC medium. These parameters are mainly the two basis vectors $\boldsymbol{a_1}$, $\boldsymbol{a_2}$, the aspect ratio $|\boldsymbol{a_2}|/|\boldsymbol{a_1}|$, the angle between the two basis vectors $\theta_{lattice} = (\boldsymbol{a_1}, \boldsymbol{a_2})$, and the normalized radius r/a or the filling factor of lattice elements. For the analytical extraction of EFSs, we firstly considered a common and simple case: the square lattice photonic crystal made of air holes with $|\boldsymbol{a_1}| = |\boldsymbol{a_2}| = a$, $\theta_{lattice} = (\boldsymbol{a_1}, \boldsymbol{a_2}) = 90^o$, and made the filling factor r/a vary. Doing this, we obtained a GPhC medium made of a square lattice with a spatial filling factor profile.

Assuming this consideration, we calculate here the relationship between the PhC EFSs near the band edge as a function of the air hole filling factor. To do that, it is necessary to have first all dispersion diagrams of square lattice photonic crystals made of different filling factors.

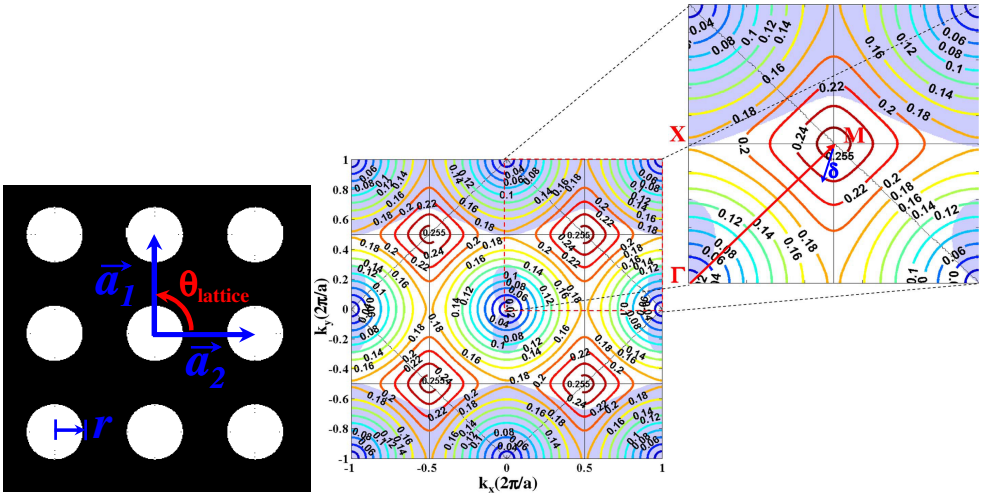

Figure 2.4: (a) Dielectric diagram of a 2D square lattice photonic crystals made of air holes $r/a = 0.3$ on silicon on insulator wafer and (b) Equi-frequency surface diagram of the first TE band of that lattice and EFSs near the M point (inset figure).

Fig. 2.4(a) shows the dielectric diagram of a square lattice photonic crystal made of air holes of normalized radius $r/a = 0.3$ in a silicon on insulator (SOI) host material, and Fig. 2.4(b) presents the EFS diagram of the first TE band obtained by considering an effective refractive index of the slab waveguide $n_{slab} = 2.95$ (this value is obtained as the refractive index of a slab waveguide of 260nm-thickness silicon on insulator at the wavelength $\lambda = 1.55\mu m$).

Within the first Brillouin zone (zone limited by $k_x(-0.5,0.5)$ and $k_y(-0.5,0.5)$), each point on the EFS curves is associated with a unique travelling Bloch wave and each wave-vector in the first Brillouin zone has an infinite number of associated wave-vectors in each higher order Brillouin zone. Thus the full wave-vector diagram is obtained by tiling the first Brillouin zone to cover all of wave-vectors in space as can be seen in Fig. 2.4(b).

We can see in Fig. 2.4(b) that EFSs at low frequencies have a circle shape centred at the Γ point. This frequency range is called the homogenizable regime as mentioned in Chapter 1. Due to the strong periodic corrugation, above the homogenizable regime, EFSs are square then depart to circles shape. Close to the M points (normalized frequencies a/λ>0.26), EFSs tend to disappear for increasing normalized wavelengths, and simultaneously recover the shape of small circles centred at M points in k-space. It is proposed here to approximate this behaviour by the following relationship:

$$\delta_x^2 + \delta_y^2 = \eta^2 \left(\omega_0^2 - \omega^2 \right) \tag{2.17}$$

where $\delta = (\delta_x, \delta_y) = (\pm 0.5 - k_x, \pm 0.5 - k_y)$ designates the wave-vector component shift from M points to the considered EFSs of (k_x, k_y), and η and ω_0 are two introduced parameters.

In spite of a similar linear relationship between the wave-vector square and frequency square $k^2 = n^2\omega^2$, the difference is two-fold in comparison with the dispersion relationship of a homogeneous or a homogenized optical material. First, the concavity of the band is downwards, i.e. the amplitude of shifted wave-vector δ decreases with the increase of frequency. Second, EFSs are not centred at Γ point, but at M points which are vertices of the first Brillouin zone. In analogy with semiconductor physics, it can be said that the related dispersion relationship is similar to what would be obtained with the effective mass theory close to a valence energy band minimum centred at some nonzero wave-vector.

Equation (2.17) gives the relationship of (δ, ω) or $(\boldsymbol{k}, \omega)$ in an analytical form in which there are two unknown quantities ω_0 and η. The next use of Hamiltonian optics to describe light propagation in case of a gradual medium thus requires estimating these quantities as a function of the chirped lattice parameter. This means that, in the considered case, ω_0 and η are needed to be estimated as a function of the normalized hole radius r/a.

The first unknown parameter ω_0 is the maximum value of frequency of the first TE band where the displacement from the EFS of this frequency to M point of the first Brillouin zone is around 0. A close inspection to EFSs given in Fig. 2.4(b)

near the M points shows that ω_0 is around 0.26 for $r/a = 0.3$. Increasing the normalized radius r/a of air holes makes the effective in-plane index decrease, so that frequencies of PhC dispersion bands tend to increase, thus makes ω_0 increased. Varying the value of filling factor r/a from 0.20 to 0.35, results of PWE calculations using the MPB software showed that a parabolic approximation can be applied for the relation of ω_0 as a function of the varied air-hole filling factor as following:

$$\omega_0\left(\frac{r}{a}\right) = 0.2792 - 0.3862\frac{r}{a} + 1.068\left(\frac{r}{a}\right)^2 \tag{2.18}$$

The filling factor range [0.2; 0.35] considered here is chosen for the purpose of practical feasibility in forthcoming fabrication steps, since the periodicity of the photonic crystal is around *400nm*.

The dependence of η is a little bit more complicated, as for a given r/a value, EFS curves depend on the chosen frequency ω below ω_0 (see the inset of Fig.2.4(b). This means that the parameter η both depends on the filling factor r/a and the frequency ω. For each frequency ω, η could be fitted by a linear relationship in the form: $\eta = \gamma_1\left(\frac{r}{a}\right) + \gamma_2$. Numerical results showed that γ_1 and γ_2 can be fitted by a parabolic law with respect to frequencies ω that are lower than the maximum frequency ω_0. The final result obtained is:

$$\eta\left(\frac{r}{a},\omega\right) = \left[2170.4\omega^2 - 1158.5\omega + 155.7\right]\frac{r}{a} + \left[-673.1\omega^2 + 355.4\omega - 46.1\right] \tag{2.19}$$

As a whole, the overall analytical dispersion relationship of the considered GPhC is given by equations (2.17), (2.18) and (2.19). The main advantage of such a form is that the effect of the air hole chirp can be directly related to the band diagram (k,ω) relationship for some frequencies ω and at some (x,y) location where r/a is known. It has been used in most of ray tracing calculations performed in forthcoming sections and has induced most of results presented in Chapter 3 and Chapter 4.

2.2.2.3. Hamiltonian optics-assisted ray tracing in the chosen GPhC operating in the diffractive regime near the photonic bandgap

The dispersion relationship extracted previously and summarized by equation (2.17-19) is applied here for the study of light propagation using the method of Hamiltonian optics. We chose the Hamiltonian H as following:

$$H = \omega^2 = \omega_0^2 - \frac{\delta_x^2 + \delta_y^2}{\eta^2} \tag{2.20}$$

Given this choice, Hamiltonian's equations in (2.1) are rewritten as:

$$\frac{dx}{d\sigma} = -\frac{2\delta_x}{\eta^2(x,y)}$$
$$\frac{dy}{d\sigma} = -\frac{2\delta_y}{\eta^2(x,y)} \tag{2.21}$$

$$\frac{d\delta_x}{d\sigma} = -2\left[\omega_0 \frac{\partial\omega_0}{\partial\left(\frac{r}{a}\right)} + \frac{\left(\delta_x^2+\delta_y^2\right)}{\eta^3}\frac{\partial\eta}{\partial\left(\frac{r}{a}\right)}\right]\frac{\partial\left(\frac{r}{a}\right)}{\partial x}$$
$$\frac{d\delta_y}{d\sigma} = -2\left[\omega_0 \frac{\partial\omega_0}{\partial\left(\frac{r}{a}\right)} + \frac{\left(\delta_x^2+\delta_y^2\right)}{\eta^3}\frac{\partial\eta}{\partial\left(\frac{r}{a}\right)}\right]\frac{\partial\left(\frac{r}{a}\right)}{\partial y} \tag{2.22}$$

In Eqs. (2.21-2.22), the quantities $\partial\eta/\partial(r/a)$ and $\partial\omega_0/\partial(r/a)$ are known (from Eq. 2.17, 2.18), the only unknown quantities are *∂(r/a)/∂x* and *∂(r/a)/∂y* which describe the filling factor profile considered for a graded photonic crystal medium to support the light trajectory defined by $\left[x(\sigma), y(\sigma)\right]$.

Propagation of rays can be implemented using the Eqs. (2.21-2.22) with the initial conditions: $x(\sigma=0)=x_0$ and $y(\sigma=0)=y_0$. It should be noted here that the arbitrary bi-dimensional chirped filling factor distribution $r/a(x,y)$ considered for the graded medium is in the validity range of $0.22 \le r/a \le 0.35$, the range that we considered for the analytical calculation of EFSs.

To validate the application of Hamiltonian optics method for light propagation in graded photonic crystals in the diffractive regime, we chose a typical 2D in plane filling factor profile presented by the Gaussian function:

$$\frac{r}{a}(x,y) = 0.35\exp\left(-\frac{x^2+y^2}{2R^2}\right) \tag{2.23}$$

and we limited minimum value of $r/a = 0.22$ for every points having a distance from the (0,0) point above 0.96R.

The dielectric permittivity map of the GPhC configuration expressed by Eq. (2.23) is shown in Fig. 2.5(a). Air holes with radius law given in Eq. (2.23) are considered for $x \ge 0$, etched in a SOI wafer with the effective index of the slab waveguide $n_{slab} = 2.95$ at $\lambda = 1550nm$. With this filling factor profile, it can be seen that the maximum value of air hole radius is at the point (0,0). The interface between the slab waveguide and the GPhC medium is along the $\Gamma - X$ direction.

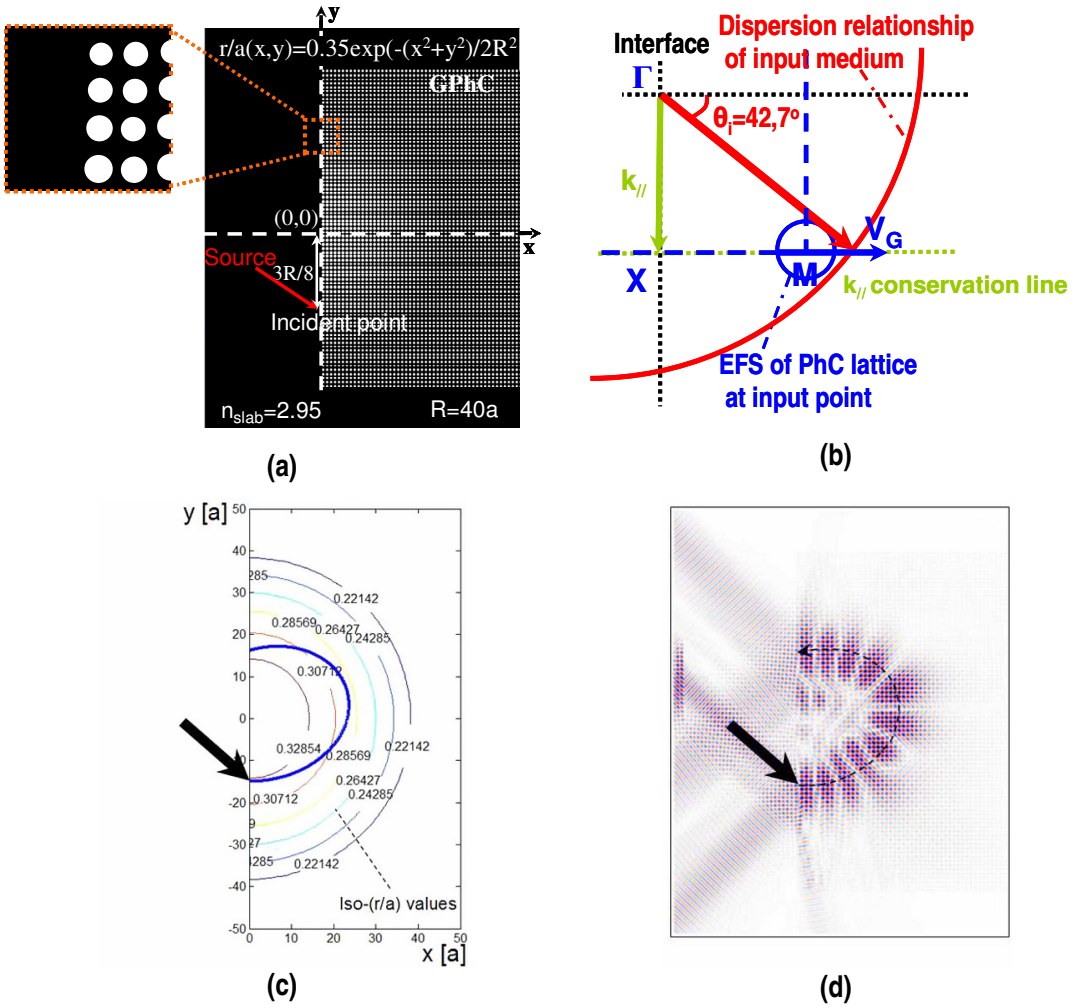

Figure 2.5: (a) Dielectric permittivity diagram of proposed GPhC configuration made with a 2D-chirp of filling factor given by Eq. (2.23); (b) Conservation wave vector law at the interface between the slab optical waveguide and the GPhC. Group velocity of the excited Bloch wave within the PhC area is depicted, (c) Propagation of a light ray in the GPhC at normalized frequency $\omega = a/\lambda = 0.25$ for input point $x = 0; y = 3R/8$ using equations of Hamiltonian optics and PhC analytical dispersion relationship (contours of iso-hole radius are presented), and (d) Light propagation in the same conditions using FDTD simulation (dotted path with arrow corresponds to the ray propagation in (c)).

The propagation of light at frequency $\omega = a/\lambda = 0.25$ was first studied by Hamiltonian optics propagation presented previously with the following chosen initial conditions. First, the initial incident point is located at $x(\sigma = 0) = 0$ and $y(\sigma = 0) = y_0 = 3R/8$. Second, the initial wave-vector is chosen as:

$$\begin{aligned} \delta_y(\sigma = 0) &= k_{//} - 0.5 = n_{slab}\omega\sin(\theta_i) - 0.5 \\ \delta_x(\sigma = 0) &= -\sqrt{\eta^2(\omega_0^2 - \omega^2) - \delta_y^2(\sigma = 0)} \end{aligned} \tag{2.24}$$

in which the parameters η, ω_0 are given by Eqs. (2.19), (2.20), and θ_i is the incident angle from the slab waveguide into the GPhC medium. The incident angle θ_i is then chosen to lead to an initial parallel wave-vector $k_{//} = 0.5$, meaning that $\theta_i = 42{,}7^o$.

Fig. 2.5(c) presents the trajectory of a light ray in the considered GPhC medium with the above chosen initial parameters. It can be seen that, light path is curved around the central region with high value of air hole radius (smaller long-range averaged refractive index region). This phenomenon illustrates a key difference with the propagation of light in the homogeneous regime presented in Section 2.2.1 where light path is bended towards the high "long-range" refractive index region.

FDTD simulation was also carried out as a comparison (validation). A Gaussian source $\omega = a/\lambda = 0.25$ of beam width $W = 7a$ was injected from the slab waveguide into the GPhC medium with an incident angle $\theta_i = 42{,}7^o$. We can see the good agreement on the light propagation (light path) realized by the Hamiltonian optics method and the FDTD simulation when comparing the two figures Fig. 2.5(c) and Fig. 2.5(d). This agreement shows that the extraction of the analytical dispersion relationship of the graded photonic crystal presented in section 2.2.2.2 and its application to describe the propagation of a ray is a good basis to describe the propagation of light in the considered graded photonic crystal.

2.3 Conclusion

The Hamiltonian optics approach for ray tracing in GPhCs employed in this thesis has been presented in this chapter for both the homogenizable and the diffractive regimes of photonic crystals. In all cases, the Hamiltonian is related to the dispersion relation of the photonic crystal medium. It is simple in the case of the homogenizable regime since the graded photonic crystal medium can be considered as an effective medium with a two-dimensional profile of refractive index. For the case of our interest – GPhCs in the diffraction regime – the photonic dispersion relationship varies in a more complicated feature in the plane of light propagation. The analytical dispersion relationship of graded photonic crystals in this case is useful for the study of light propagation. One particular case made of a square lattice photonic crystal with a variable filling factor was considered for that, and an analytical extraction of the related dispersion relationship as a function of the varied parameter was done. Hamiltonian optics method and FDTD simulation have been performed separately and a good agreement between the two approaches was obtained, meaning that the analytical extraction of the dispersion relationship is a powerful tool for the study of light propagation in graded photonic crystals.

The analytical extraction of photonic crystal EFSs in the particular case presented in this chapter, together with the Hamiltonian optics approach, will be used in the next chapter to see how light propagates inside 2D-filling factor-chirped graded photonic crystals and evaluate the possibility of utilizing their properties for the realization of integrated optical functions.

Chapter 3

Modeling and Simulation of Graded Photonic Crystals

Modeling and simulation of graded photonic crystals (GPhCs) will be presented in this chapter. As demonstrated in the last section of chapter 2, a proof-of-concept configuration of a GPhC made of a square lattice with a 2D-profile of air hole filling factor has been proposed for the validation of using the involved method to study the propagation of light in GPhCs. In this chapter, we also choose this profile of filling factor for the simulations of graded photonic crystal structures to propose several devices amenable to fabrication and experimental demonstrations.

Modeling of light propagation in GPhCs will be realized using the method of Hamiltonian optics-assisted ray tracing as well as FDTD simulation.

We will, in the first section, see the mirage effect in the studied GPhC structure and also the correlated results obtained by the two simulation methods.

The sensitivity to wavelength of the studied structures will be presented in the second part, showing the possibility of using them for wavelength demultiplexing.

Finally, the third part of this chapter is devoted to the study of the polarization properties of the considered GPhC structures.

3.1. Mirage and superbending effect in the considered square-lattice GPhC

The mirage effect, in nature, can be observed due to the modification of the air optical index induced by the atmosphere temperature. The modification of the optical index makes light rays to be curved along bended trajectories according to the Snell's law, i.e towards to high optical index regions. This results in the fact that we observe the distorted and displaced images of distant objects with a small angle below or above the horizontal plane of view through the atmosphere. An example of the natural

optical mirage effect can be seen in Fig. 3.1(a), where the driver sees the false image of a palm below the ground.

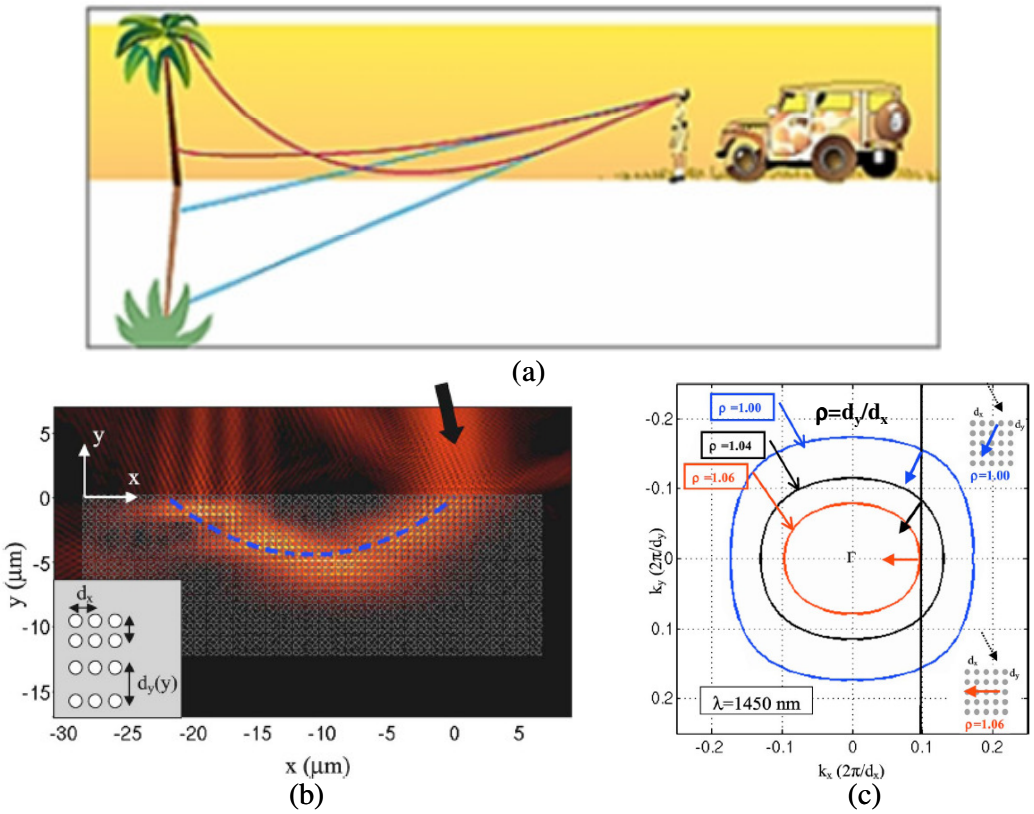

Figure 3.1: (a) An example of natural optical mirage caused by the modification of optical index induced by the atmosphere temperature, (b) An example of artificial optical mirage effect in a two-dimensional graded photonic crystal [21] and (c) operation principle of the mirage effect in this graded photonic crystal configuration.

An example of the artificial mirage effect has been theoretically proposed in [21] in a configuration of a graded photonic crystal containing a one dimensional chirp of lattice periodicity of a rectangular lattice photonic crystal as can be seen in Fig. 3.1(b). The incident light beam, after penetrating into the GPhC structure, is bended and then exits the configuration making a curved trajectory. The direction of the light path at each point can be determined by the Bloch wave group velocity which is normal to the deformed EFS due to the gradient of lattice periodicity as presented in Fig. 3.1(c). The mirage effect in this GPhC occurs at frequencies in the 2^{nd} *band*, in *TE polarization*, and has also been experimentally demonstrated in [24] at *microwave frequencies* using a similar configuration.

Restarting directly from the desired light paths, we have proposed in section 2.2.1 of chapter 2 a mirage-like beam effect. We introduced for this that light is bended to form a quarter circle path (Fig. 2.2) by propagating in a square lattice graded photonic crystal configuration operating in the long-wavelength regime of light propagation and described by the *two-dimensional profile of average refractive index* mentioned in Eq. 2.13.

Later in section 2.2.2 of chapter 2, we introduced a GPhC configuration which is in fact the reference GPhC structure of the manuscript. As a starting point for light

bending, the two-dimensional index profile $n(x,y)$ given by Eq. 2.13 was simply transposed into a similar air-hole radius profile $r/a(x,y)$ given by Eq. 2.22. And this led to the structure that is described in the next sub-section.

3.1.1 Structure design

The overview of the dielectric permittivity of the proposed reference GPhC configuration of GPhC is illustrated in Fig. 3.2(a).

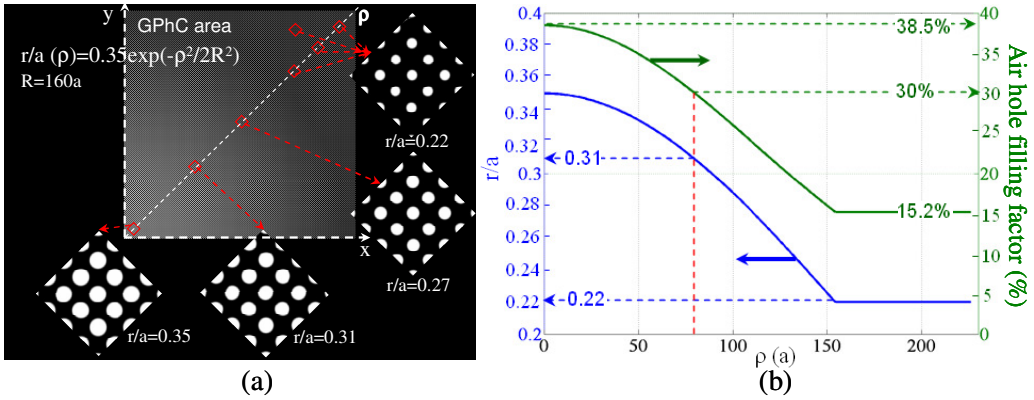

Figure 3.2: (a) Dielectric permittivity diagram of a graded photonic crystal configuration made of a 45°-rotated square lattice photonic crystal with a Gaussian-like air hole radius profile described by Eq. (3.1). The GPhC area is limited by $x \geq 0, y \geq 0$ and air hole radius is limited to the minimum value $r/a = 0.22$ for all positions in (x,y) plane that are farther to the zero point than 0.96R, and (b) The air hole radius (blue curve) and the filling factor (green curve) profiles along the distance $\rho = \sqrt{x^2+y^2}$ (in lattice unit a)

It is characterized by the following parameters:

- It is made of a air hole square lattice photonic crystal, rotated by 45°, forming the $\Gamma - M$ interface. This rotation angle is chosen to ease the problem of light coupling from a slab waveguide into the GPhC medium. It enables to have an incident angle of zero degree for light excitation with an initially horizontal group velocity.
- The normalized air hole radius profile is described by:

$$\frac{r}{a}(\rho) = 0.35\exp\left(-\frac{\rho^2}{2R^2}\right) \tag{3.1}$$

where $\rho = \sqrt{x^2+y^2}$ is the distance from the $(0,0)$ point, R is the radius of light bending curvature. Here, R is chosen $R = 160a$ (corresponds to an area of $61\mu m x 61\mu m$) to ensure a slow-enough in-plane variation of the air hole radius, provided that the minimum value of air hole radius is limited to $r/a = 0.22$ for every lattice points that are farther than 0.96R from the (0,0) point.

The air hole radius (blue curve) and the air hole filling factor (green curve) profiles of the square lattice photonic crystals along the distance ρ (in lattice unit *a*) from the GPhC left-bottom corner are presented in Fig. 3.2(b). It is shown that the filling factor of air (or the *average emptiness of the medium*) at different points inside the considered configuration varies from 38.5% (at the bottom left) down to 15.2% (corresponding to air hole radius 0.35 down to 0.22, respectively) as the distance increases. This average emptiness of the medium is one of the parameters to take into account to analyze the effects that will be presented in the simulation results in the following section.

Simulations of light propagation in the proposed GPhC configuration have been performed based on a SOI wafer with the silicon layer thickness of 260nm, the effective index of the slab waveguide being $n_{slab} = 2.95$ at the wavelength $\lambda = 1550nm$ in transverse electric (TE) polarization.

3.1.2. Circular 90°-bending GPhC structure

We started with the proposed GPhC configuration with the aim to design a circular 90°-bending light path. As we have seen in Fig. 2.5(c) of chapter 2, light beam can be bended in the proposed GPhC configuration (but not necessarily along a circular light trajectory). In this section, in order to find the desired light trajectory in this configuration, we first investigate the location of the appropriate incident point of the light beam. The estimation of losses as well as the way to enhance the transmission coefficient of the proposed GPhC configuration by adjusting input/output tapering regions are also presented in this section.

3.1.2.1. Study of the incident point to inject light into GPhC configuration

The proper position of light injection has been studied by adjusting the incident point $y(0)$ from *R* to *0* using Hamiltonian optics-assisted ray propagation.

A light ray at frequency $\omega = a/\lambda = 0.25$ (corresponding to the wavelength of $\lambda = 1550nm$) was considered to be injected into the GPhC area at different incident points ($x = 0$, y=*0* to *R*) with the incident angle $\theta_{in} = 0°$. This frequency excites a Bloch wave with the initial parallel wave-vector $k_{//} = 0$. The trajectory of this light ray in the proposed configuration can be then solved by the Hamiltonian's equations with the analytical dispersion relationship of the graded photonic crystal medium expressed by the set of three equations Eqs. (2.18), (2.19) and (2.20) presented in chapter 2.

For illustration, different light paths of light rays injected into the proposed GPhC configuration at 11 different values of $y(0)$ are presented in Fig. 3.3(a).

It can be estimated from the Eq. (2.18) that the maximum frequency value of the first band is around $\omega_{max\_1} = 0.2453$ for the lattice at the input point y(0)=R, and $\omega_{max\_1} = 0.2472$ for the lattice at the incident point y(0)=0.9R. The value of ω_{max_1} only starts to be superior to $\omega_{max\_1} = 0.25$ for $y(0) \le 0.8R$. This explains why two straight lines are adjacent to the homogeneous medium-GPhC interface, meaning that no value of ω_{max_1} can be found to satisfy the condition $\omega < \omega_{max\_1}$, and thus that light cannot enter the GPhC area.

The bending effect occurs from the incident point y(0)=0.8R, forming light paths with different curvatures. The variation of the air hole radius along each of these light paths is illustrated in Fig. 3.3(b). Among those, there is only one curve that shows a nearly-invariant air hole radius along the light trajectory, corresponding to the incident point $y(0)=0.5R$. The invariant air hole radius (around the value of *r/a=0.31*) proves that all points on the light trajectory have the same distance with respect to the origin.

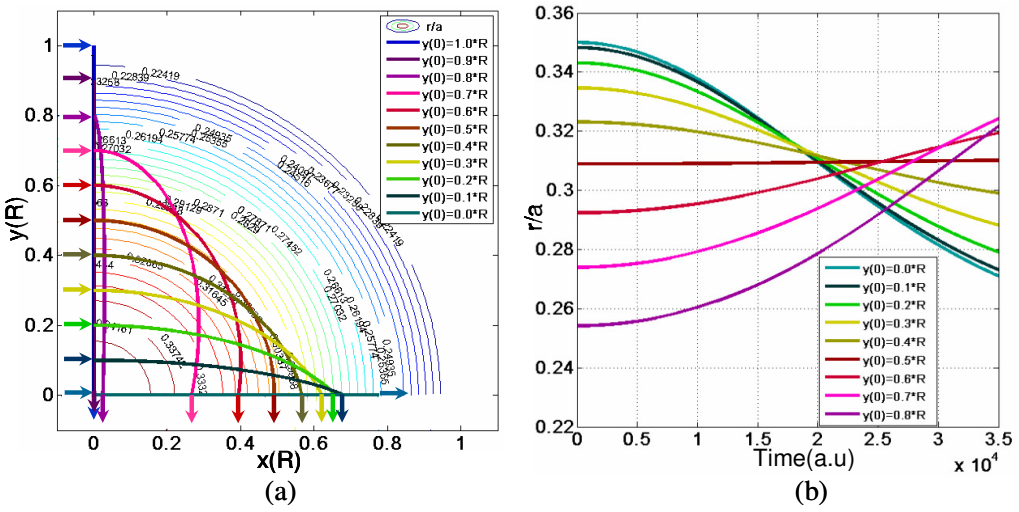

Figure 3.3: Study of the influence of the light incident point at the slab/GPhC interface: (a) Different light ray trajectories inside the considered GPhC configuration at frequency $\omega = a/\lambda = 0.25$ obtained by adjusting the incident point from $y(0) = R$ to $y(0) = 0$ and (b) Normalized air hole radius along these obtained trajectories.

These simulation curves lead to the three following conclusions:

1) Light paths are sensitive to the incident point.
2) Light injected at the incident point $y(0) = R$ does not propagate in a circular 90°-bending light path, while this incident point is the condition to obtain a quarter circle bending light path in the average-index-profile GPhC configuration in the homogenizable regime as mentioned in section 2.2.1.

In order to get the circular 90°-bending in the studied GPhC configuration, the input point should be chosen at $x(0) = 0$ and $y(0) = R/2$ in the present configuration.

Hereinafter, simulations of the proposed GPhC configuration will be considered with a TE light beam at the incident point $(x(0) = 0, y(0) = R/2)$.

3.1.2.2. Light propagation in circular 90°-bending GPhC structure

Light propagation in the proposed circular 90°-bending GPhC structure was simulated by both ray tracing and FDTD methods. The air hole radius profile of the studied configuration is color-graphically showed in Fig. 3.4(a). The EFS diagram in the first TE band of the square lattice photonic crystal (with *r*/*a*=0.31) at the incident point is figured out in Fig. 3.4(b). It can be seen that the maximum value of frequency in the first TE band is around 0.255.

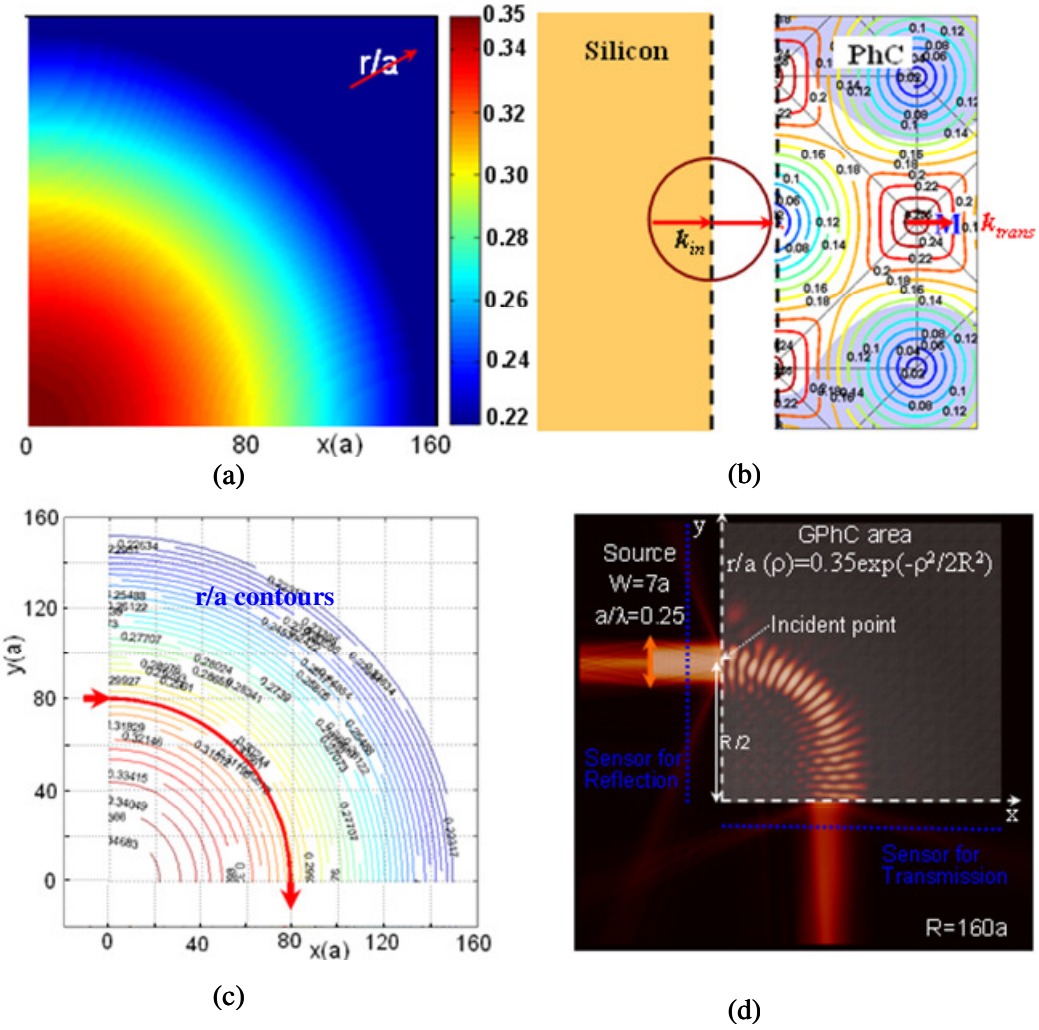

Figure 3.4: (a) Air hole radius map of the considered graded photonic crystal medium. The profile of air hole radius is governed by Eq. (3.1), the maximum value is $r/a = 0.35$ at the bottom-left corner (illustrated by dark red color) and limited to the minimum value of $r/a = 0.22$ (illustrated by blue color) for every point further from the $(0,0)$ point than $0.96R$; (b) Equi-frequency surface diagram of the first TE band of the 45-rotated square lattice photonic crystal with $r/a = 0.31$; (c) Propagation of a light ray at normalized frequency $\omega = a/\lambda = 0.25$ in TE polarization, injected at the initial point $x = 0; y = R/2$, with an incident angle $\theta_{in} = 0°$ in the studied GPhC medium using Hamiltonian optics simulation and (d) The related steady-state field of a TE Gaussian beam in the studied at normalized frequency $\omega = a/\lambda = 0.25$ with the same conditions used in Hamiltonian optics simulation.

The circular light path of the injected light ray at frequency $\omega = 0.25$ is illustrated Fig. 3.4(c) together with the iso-radius contours of the configuration in (x,y) plane. The steady-state electric field of a TE polarized Gaussian light source with a beam waist of $7a$ at frequency $\omega = 0.25$ injected into the studied GPhC structure can be observed in Fig. 3.4(d) using 2D-FDTD simulation.

The steady-state field map of the TE light beam at frequency $\omega = 0.25$ also visually shows that the optical losses of light propagating inside the considered GPhC configuration are quite low. We see only some small diffraction beams at the input and output of the configuration, as shown in Fig. 3.4(d). However, it is worth to estimate it quantitatively. This point is presented in the upcoming sub-section.

3.1.2.3. Estimation of losses and bandwidth in the 90°-bending GPhC structure

To estimate the overall losses as well as the transmission efficiency of the studied configuration after a 90°-bending, two sensors with the same size of $160a$ as the GPhC area have been placed at the input and output of the GPhC simulation area, as can be seen in Fig. 3.4(d). The input source was a TE polarized Gaussian pulse centred at $\omega = 0.25$ with the bandwidth of $\Delta\omega = 0.1$. The source is directed onto the GPhC configuration as usual at the incident point ($x = 0, y = R/2$). The sensor placed at the output is for measuring the transmission flux, and the one placed at the input is for measuring the reflection flux of light. By analyzing these fluxes, the transmission, reflection, as well as losses can be estimated.

Fig. 3.5(a) shows the overall calculated transmission (T - blue line), reflection (R-pink line) and the loss (1-T-R - red line) spectra of the GPhC area. As can be seen, the bending effect occurs in the normalized frequency range extending from 0.22 to 0.26. For normalized frequency $\omega = a/\lambda$ below 0.22, the bending effect of the GPhC is lost. The same phenomenon happens for frequencies above 0.26, which introduce a high reflection coefficient.

The power spectra obtained in Fig 3.5(a) can be explained by associating them with the photonic band structure. Within the proposed configuration, the photonic band-structure varies with the local point in space due the two-dimensional graduality of the structure. However, we care here mainly for the photonic band-structure of the photonic crystal lattice near the incident point where light is injected into the GPhC medium.

Figs 3.5(b), and 3.5(c) show the calculated band structure of the photonic crystal lattice at the incident point of light (where the air hole radius r/a is around 0.31) in TE light polarization and the calculated overall power transmission as a function of normalized frequency a/λ, respectively. As it can be seen in Fig. 3.5(b), there exists a local photonic bandgap of $\Delta\omega = 0.02$ between the first ($\omega_1 = 0.26$) and the second ($\omega_2 = 0.28$) band at the point M (edge corner of the first Brillouin zone). Since light is injected into the studied structure along the Γ-M direction, it is totally reflected for frequencies inside the photonic bandgap. A good agreement is obtained between the dispersion diagram and the calculated transmission that drops in the frequency range $0.26 < a/\lambda < 0.28$.

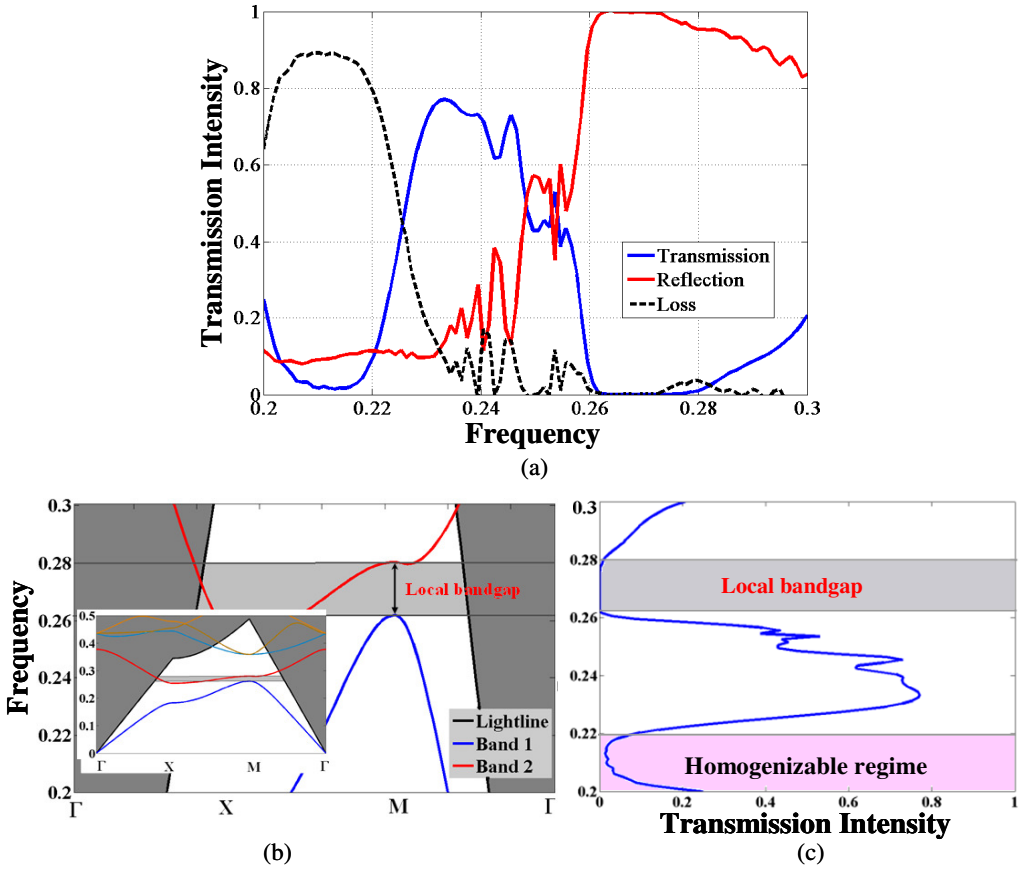

Figure 3.5: (a) Transmission spectrum of light propagating though the considered GPhC configuration, (b) TE band structure of the square lattice photonic crystal at the incident point (r/a=0.31), and (c) Frequency – Transmission intensity relationship in comparison with the photonic band structure.

Referring to Fig. 3.5(a), we see that the frequency range for which light is bended by 90° roughly extends from $\omega \approx 0.23$ to 0.257 (i.e 1500nm to 1690nm). Frequencies higher than $\omega>0.26$ ($\lambda<1490$nm) lie in the local photonic bandgap between the first band and the second band of the photonic crystal, which explains the drop in transmission. Transmission after the 90°-turn also drops for $\omega<0.22$ (wavelengths above $\lambda=1700$nm) because we then enter the long-wavelength homogenization approximation of the periodic medium, and light then propagates across the corrugated graded medium mostly in the straight direction (the transmission of light in the straight direction will be discussed again in the last section of this chapter).

The 90°-bending transmission coefficient ranges from 78% (-1.5 dB) to 40% (-4 dB). The insertion loss level of the graded photonic crystal region is thus quite low. This characteristic is due to the fact that light enters the GPhC at normal incidence angle. Highly dispersive regions of strictly periodic PhCs have often to be excited with specific input angles that make light injection into the PhC rather low. This drawback is circumvented here as light enters the gradually corrugated medium with a horizontal group velocity and is bended only after.

In spite of this interesting feature, there still remains two points to be improved:

- The insertion loss can be further minimized by eliminating the diffraction that can be seen in the Fig. 3.4(d).
- The transmission is not constant in the frequency range of the bending effect.

These two points will be considered to improve the transmission efficiency in the 90°-bending GPhC structure in the following sub-section.

3.1.2.4. Enhancement of the transmission efficiency in the 90°-bending GPhC structures

It is to be reminded that in the simulated configuration (as well as in the real fabricated configuration soon mentioned in the next chapter), light is coupled into the GPhC area from a slab waveguide that presents an impedance mismatch for incoming electromagnetic waves at the slab/photonic crystal interface. To enhance the transmission efficiency in the studied GPhC structure, it is possible to improve the light coupling efficiency into the GPhC area. To do it, the use of input/output tapers can be considered as shown in Fig. 3.6.

The underlying idea of these intermediate tapering regions is using a gradual interface in order to minimize the impedance mismatch for incoming electromagnetic waves at the slab/photonic crystal interface [25]. This approach experimentally proved to be efficient in case of Bloch wave excitation in the first PhC band [26]. A strong difference with previous situations is yet related to the fact that the PhC opto-geometrical properties are not constant over the slab/PhC interfaces, i.e. along the (x=0,y≥0) and (x≥0,y=0) half-lines.

As these considered input and output gradual tapers being identical, attention is essentially focused here on the input one. The input taper contains a linear increase in 20 steps of the air hole radius from r = 85nm (r/a = 0.22) to the hole radius value at the current point along the input interface of the GPhC area (varying itself from 136 to 85nm along the (x=0,y>0) and (x>0,y=0) interfaces according to the $r/a(\rho)$ = $0.35.\exp(-\rho^2/2R^2)$ law). By itself, the reduction of r is responsible for the decrease of the band-edge frequency of the PhC band 1, leading to strong reflection in the considered normalized frequency range around 0.25. A linear increase of the lattice period was thus simultaneously considered to maintain the normalized frequency a/λ below the band-edge limit. In practice, a linear increase of lattice periodicity a from 305nm to 390nm at the input of the GPhC area was considered.

As a whole, the designed input and output tapers are thus made of a two-dimensional chirp of the air hole radius and a one-dimensional chirp of the lattice period.

The related tapers are shown in two insets in Fig. 3.6.

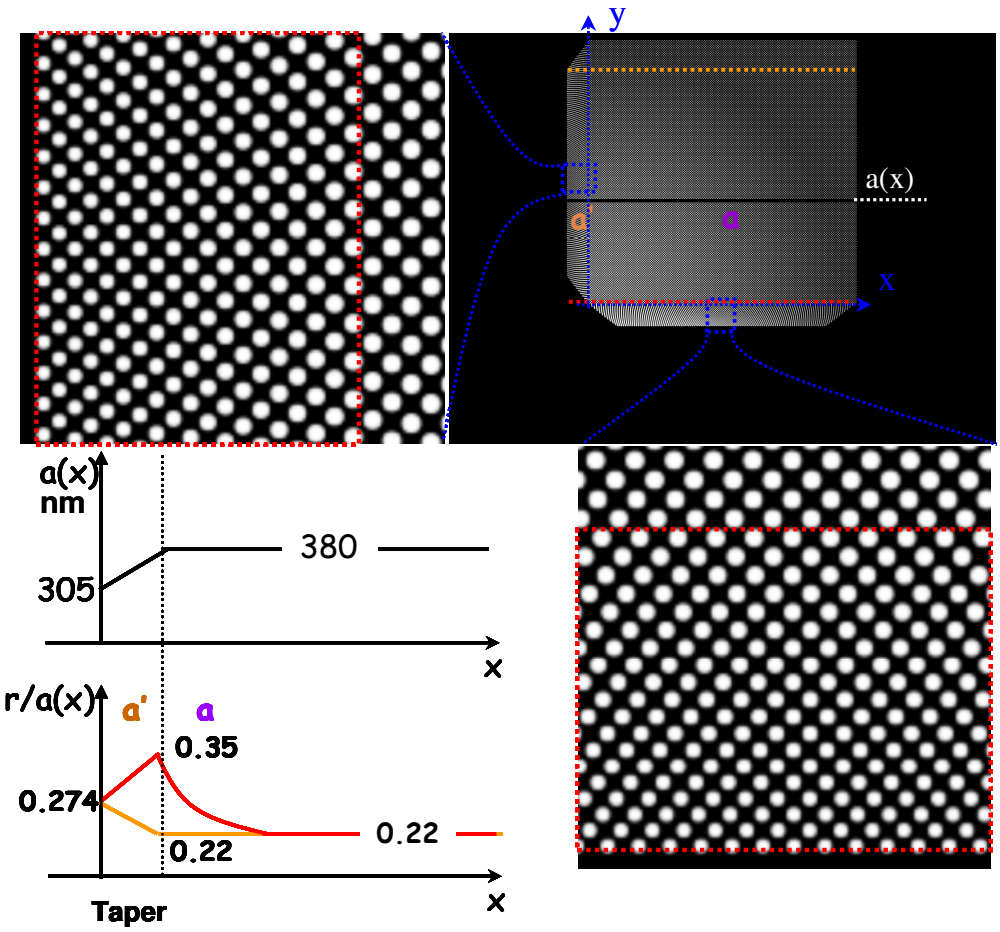

Figure 3.6: Dielectric permittivity of graded photonic crystal configuration with tapering regions at the input and output to minimize the impedance mismatch between the incoming and outcoming waves with respect to GPhC medium.

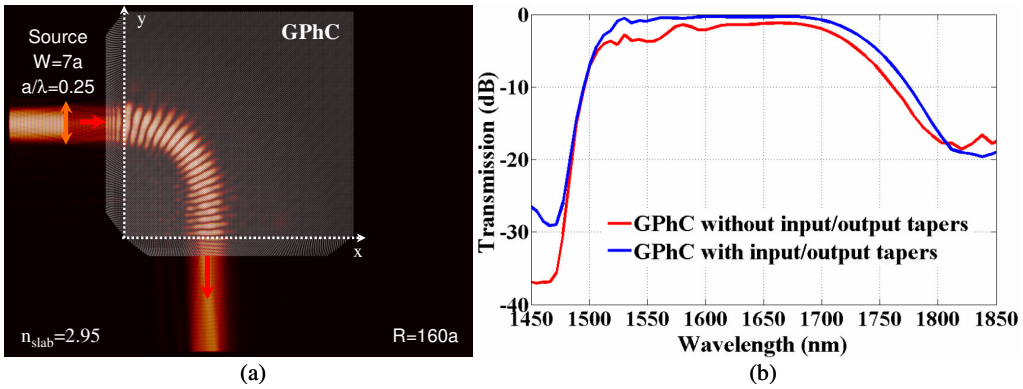

Figure 3.7: (a) Steady-state field of a light beam at frequency $\omega = a/\lambda = 0.25$ inside the proposed GPhC medium with input and output tapers; and (b) Comparison of the transmission spectra in two cases: with and without input and output tapers.

The propagation of the 7*a*-beam width Gaussian beam in the studied GPhC configuration with I/O tapers is presented in Fig. 3.7(a).

It can be seen that the diffraction beams are lower at the input and output if compared with the case without these two tapering regions. The enhancement of the transmission efficiency is shown in Fig. 3.7(b). The transmission bandwidth is quite the same but the transmission is about 2dB higher in case of GPhC with I/O tapers (up to 95%) than in the case of the GPhC configuration without I/O tapers (78%).

Because of this enhancement, in the following simulations, we will utilize the proposed configuration with I/O tapers.

3.1.3. Other configurations for light bending effect

In the latest section, we have seen the possibility of achieving a 90°-bending of light in the proposed GPhC configuration. In the following, we will present the possibility to combine several blocks of the proposed structure for bending light with different bending shapes, in particular, the 180°-bending and the 270°-bending configurations.

3.1.3.1. 180°-bending GPhC structure

To form a 180°-bending configuration using the proposed GPhC configuration presented in 3.1.2.2, it is possible to combine two blocks of that configuration, provided that its air hole radius profile is governed by the Eq. (3.1) in the area limited by $x \geq 0$. The configuration is also composed of two input and output tapering regions as proposed in the previous section. We can see the dielectric permittivity diagram of the 180°-bending configuration in Fig. 3.8(a).

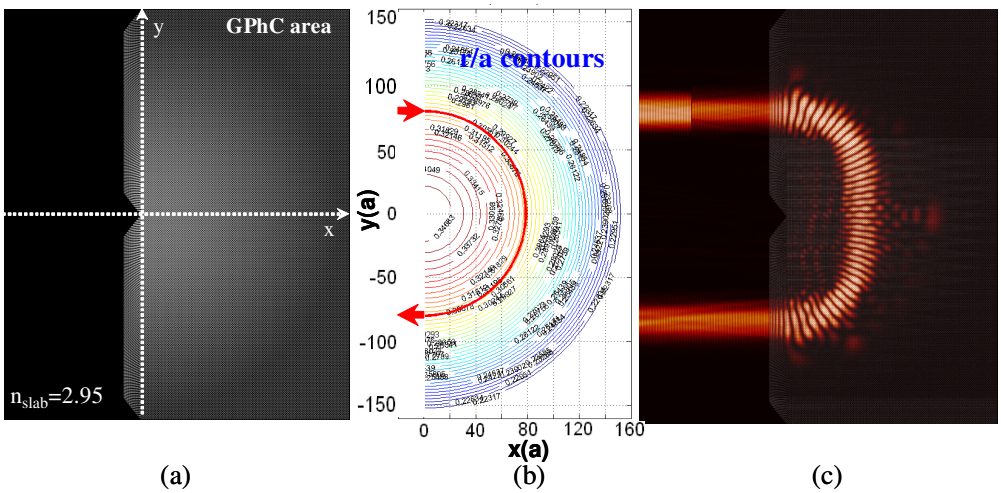

Figure 3.8: (a) Dielectric permittivity diagram of GPhC configuration for 180°-bending effect and (b) Light path of a Gaussian beam of $7a$ beam width in 180-bending GPhC structure at frequency $\omega = a/\lambda = 0.25$.

As usual, the mirage effect in this configuration is simulated using two methods: Hamiltonian optics (Fig. 3.8(b)) and FDTD (Fig. 3.8(c)) simulations. A light ray at the frequency $\omega = 0.25$ is bended inside the present GPhC configuration, making a half-circle-light-path, i.e a curvature of 180 degrees as shown in Fig. 3.8(b). The comparative result can be observed in Fig. 3.8c for the Gaussian beam of $7a$-beam waist at frequency $\omega = 0.25$. It worth to remind that, in this configuration, we still inject light into GPhC area at the incident point $x = 0, y = R/2$.

3.1.3.2. 270°-bending GPhC structure

A 270°-bending GPhC structure can be also constructed by combining three blocks of the 90°-bending GPhC configuration presented in 3.1.2.2. The diagram of dielectric permittivity of this 270°-bending GPhC structure is presented in Fig. 3.9(a). The first two blocks in the right are the same as in the configuration of the 180°-bending, the third block in the bottom left is formed by rotating the proposed 90°-bending block with an angle of -90° and shifting the (0,0) point to (0,-R).

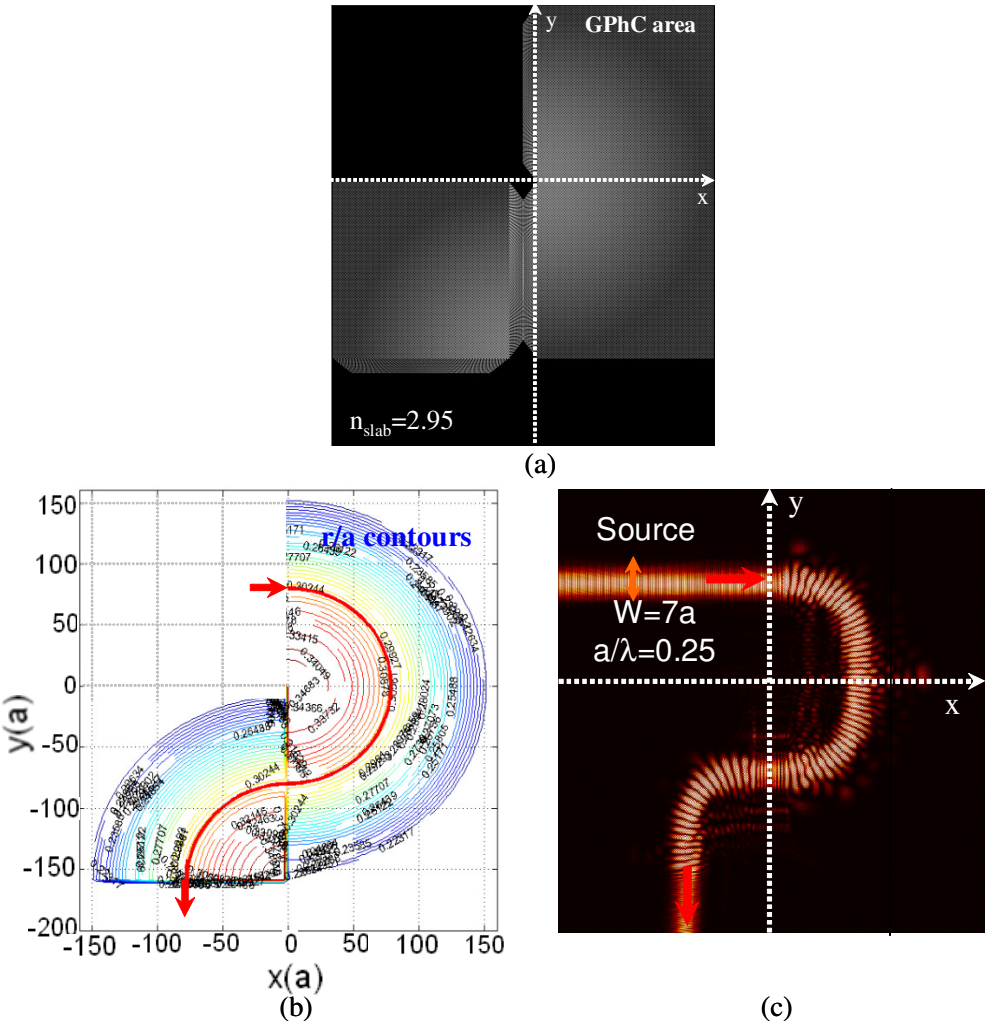

Figure 3.9: (a) Dielectric permittivity diagram of GPhC configuration for 270-bending effect; and (b) Trajectory of a light ray; and (c) Light path of a Gaussian beam of $7a$ beam width in 180-bending GPhC structure at frequency $\omega = a/\lambda = 0.25$.

Again, a good agreement between the two methods of simulation for a single light ray and a Gaussian light beam at frequency $\omega = 0.25$ is obtained.

The mirage effect presented in the two (180°- and 270°-) bending structure proves that the proposed configuration for 90°-bending can be flexibly combined and utilized for curving and shaping the light beam propagating inside graded photonic crystals.

In addition, hereinbefore, we mentioned and proposed only one profile of *r/a*, thus there is a richness of configurations that could be used for the purpose of controlling light beams inside graded photonic crystals.

3.2. Wavelength dispersion sensitivity of graded photonic crystals

In all of the above simulations on graded photonic crystal configurations described in this chapter, we have mentioned and considered only one single frequency $\omega = 0.25$ (corresponding to the wavelength $\lambda = 1550nm$). Yet, we can see that the mirage effect can be observed in different configurations and in a bandwidth of $\Delta\omega = 0.04$. Due to the deformation of EFSs of frequencies in this band (as can be seen in Fig. 3.4(b), the proposed configuration is predicted to be sensitive to wavelength.

Thus, in this section, we study the possibility of the proposed GPhC configuration to deflect light beams by tuning the optical frequency (light wavelength) within this bandwidth. Doing this, we exploit the short-wavelength light propagation regime characterizing the studied GPhC configuration.

3.2.1. Sensitivity to wavelength

The expected frequency range for exploring the sensitivity to wavelength of the studied GPhC structure is the range in which light is bended while propagating in the medium. For this, we tuned the input wavelengths from 1500nm to 1700nm with an increasing step of 10nm. The evolution of light paths for these wavelengths in the studied configuration obtained by the Hamiltonian optics propagation method is presented in Fig. 3.10(a). The input and output points are now indicated in µm. We observe that longer wavelengths propagate with longer trajectories and that a shift of about $40\mu m$ is obtained for the considered wavelength range.

The outputs of the longer wavelengths (low frequencies) are collected at farther positions from the $(x = 0, y = 0)$ point in comparison with those related to short wavelengths (high frequencies).

Near the incident point, all light rays of different wavelengths indeed experience the same air hole filling factor r/a (meaning the same ω_{max_1}) but different η (since this value depends on both *r/a* and ω: see Eq. (2.19)) due to the different values of ω. As a consequence, the different light paths begin to split, meaning that different values of hole filling factor are seen afterwards, and thus different values of

both of ω_0 and η, which reinforces the splitting effect between the different wavelength-dependent rays. As a whole, it can be said that the different rays cross "different optical periodic media", as shown in Fig. 3.10(b). In the plane of light propagation considered here and presented in the Fig. 3.10(b), it can be seen that the hole radius is roughly constant around r/a=0.31 along ray path for $\lambda = 1550nm$ (ω=0.25) due to the nearly circular trajectory, while it decreases down to the minimum value r/a=0.22 for the wavelength $\lambda = 1700nm$ (ω=0.228). The two dispersion PhC parameters ω_0 and η vary consistently.

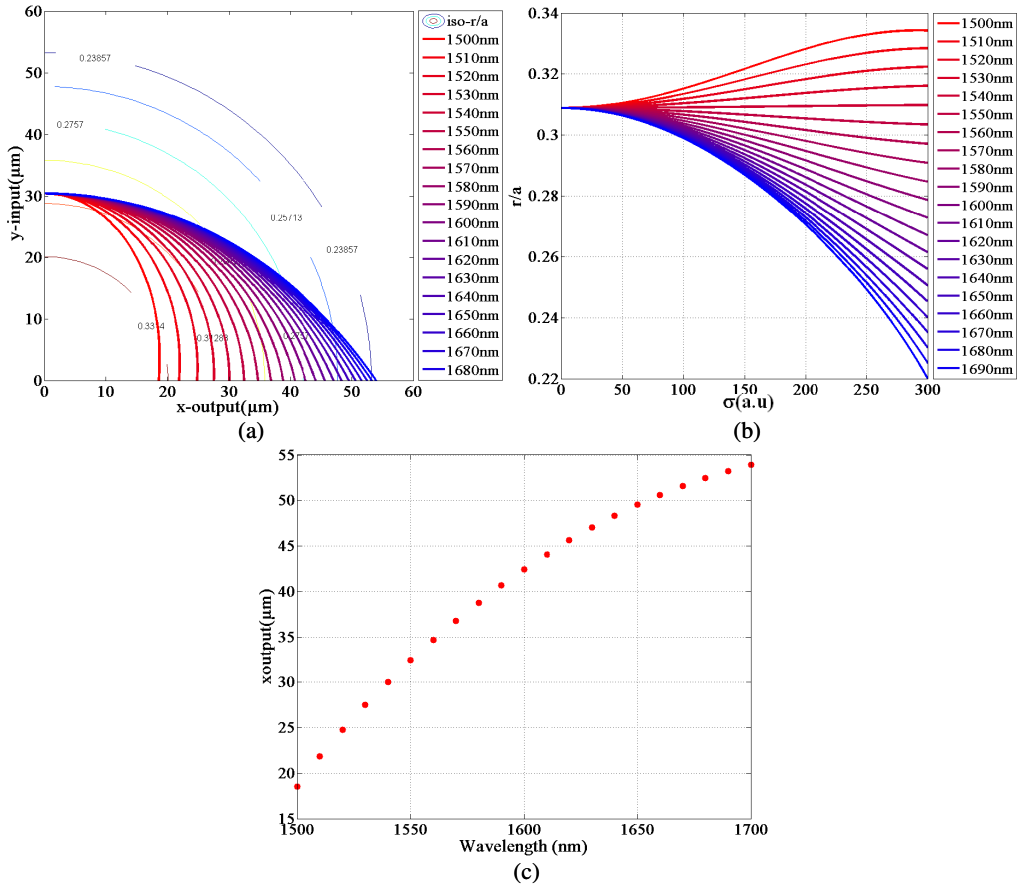

Figure 3.10: (a) Light paths for different wavelengths from 1500nm to 1700nm, using Hamiltonian optics simulation; and (b) Values of air hole radius along the different ray trajectories, and (c) Wavelength dispersion sensitivity of the studied configuration of graded photonic crystal

Fig. 3.10(c) shows the relationship between the output position and the tuning input wavelength. A sub-linear relationship is obtained for the tuning frequency range from 1500nm to 1700nm, introducing a dispersive coefficient of 0.2µm (output-shift)/nm (wavelength tuning).

To prove the sensitivity to wavelength of the studied configuration, FDTD simulations were realized for different frequencies. We show here the case of two frequencies ω=0.25 (1550nm) and ω=0.24 (1616nm). The different optical trajectories and the shifted output positions of these two frequencies can be seen in Fig. 3.11.

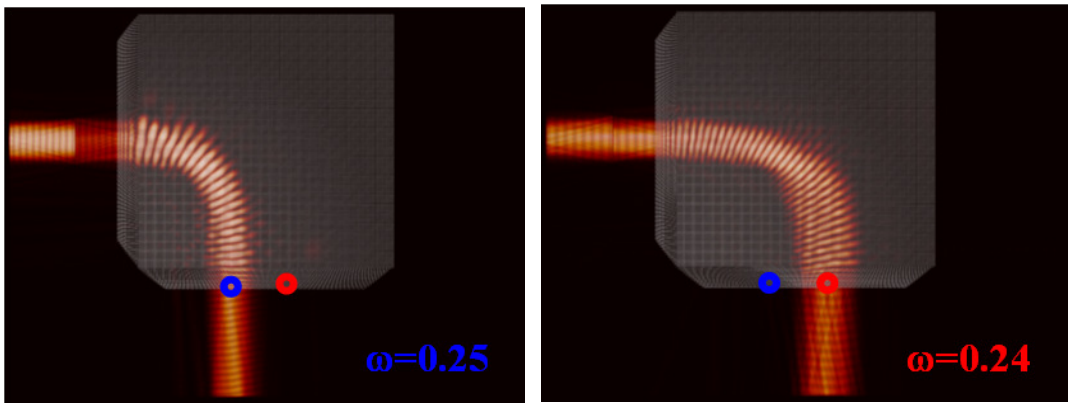

Figure 3.11: Light paths of two Gaussian beam with beam waist 7a inside the considered graded photonic crystal configuration at two frequencies (a) $\omega_1 = 0.25$ and (b) $\omega_2 = 0.24$ using FDTD simulation.

3.2.2. Two-channel demultiplexing

With a wavelength dispersion of 0.2µm/nm as mentioned in the previous sub-section, it is possible to utilize this configuration of GPhC for demultiplexing. We first present here this possibility for two channels.

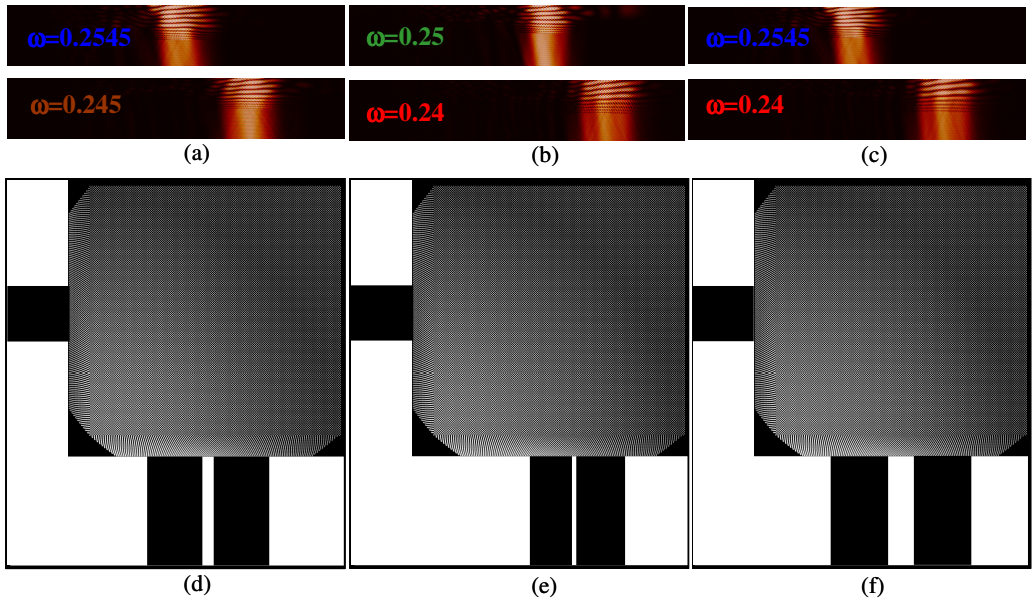

Figure 3.12: (a), (b), (c) Three sets of light paths inside the proposed graded photonic crystal configuration (0.2545; 0.245), (0.25; 0.24); (0.2545; 0.24) for the purpose of wavelength demultiplexing; (d), (e), (f) Dielectric permittivity diagrams of three two-channel demultiplexing devices based on the studied graded photonic crystal configuration. Two output channels are placed at proper positions using the calculation results presented in Fig. 3.10(c).

Three sets of two different frequencies (0.2545; 0.245), (0.25; 0.24), and (0.2545; 0.24) have been chosen to be simulated by FDTD in order to provide a sufficient separation (more than 12µm) at the outputs, as can be seen in Figs. 3.12(a), (b) and (c).

The dielectric permittivity diagrams of three basic two-channel demultiplexers corresponding to three sets of light paths of two frequencies given in Fig. 3.12(a), (b) and (c) are illustrated in Figs. 3.12(d), (e) and (f), respectively. Strip waveguides have been additionally considered at the input and output of the graded PhC area to inject and collect the light into and from the graded photonic crystal area. The two output waveguides of each demultiplexing configuration are placed at proper positions based on the prediction by Hamiltonian optic propagation and FDTD simulations. An optical source with a waist of 7a served to excite electromagnetic fields within the structure and sensors were placed at right locations to calculate power transmissions at two channels: channel 1 (T_1) and channel 2 (T_2).

Fig. 3.13 shows the optical transmission spectra of the three proposed GPhC structures presented in Fig. 3.12. Results show that two centred wavelengths of each demultiplexer are well separated and collected at the two output channels with a low loss (0.5dB) and low crosstalk (less than -20dB) levels.

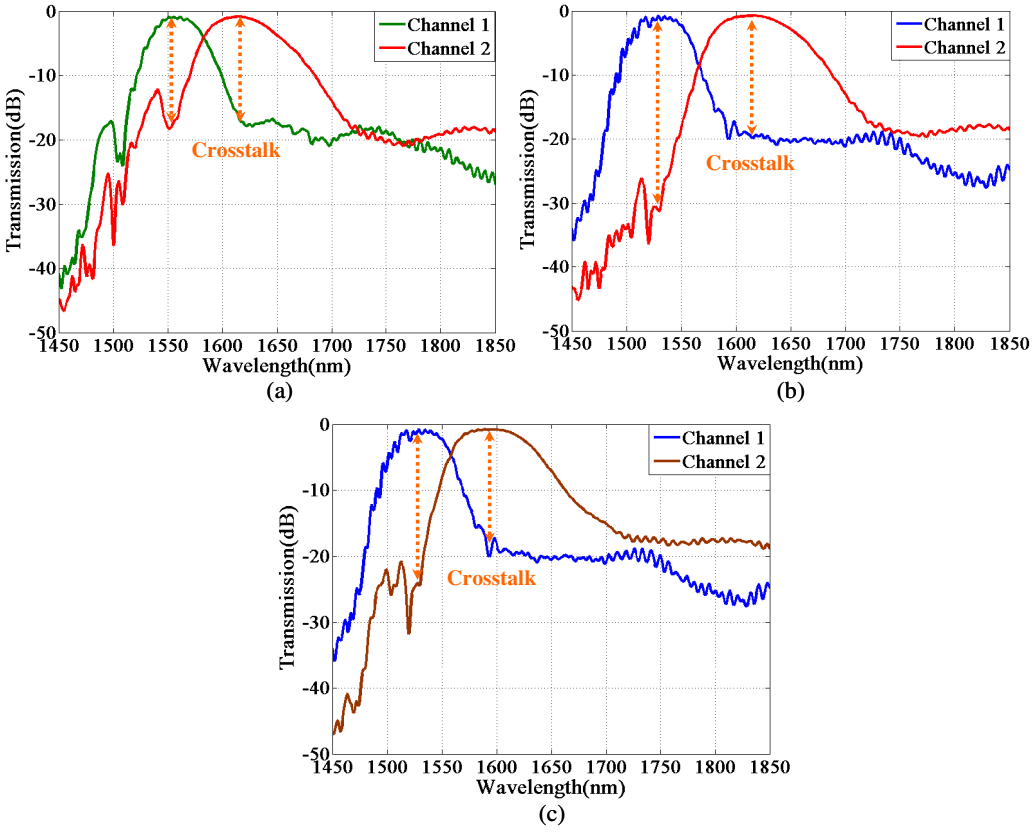

Figure 3.13: Operation of three considered 2-channel demultiplexing devices (a) Channel 1 $\omega_1 = 0.25$ ($\lambda_1 = 1550nm$) and Channel 2 $\omega_1 = 0.24$ ($\lambda_1 = 1616nm$); (b) Channel 1 $\omega_1 = 0.2545$ ($\lambda_1 = 1526nm$) and Channel 2 $\omega_1 = 0.24$ ($\lambda_1 = 1616nm$); and (c) Channel 1 $\omega_1 = 0.2545$ ($\lambda_1 = 1526nm$) and Channel 2 $\omega_1 = 0.245$ ($\lambda_1 = 1585nm$)

Beyond the possible operation of these devices as basic demultiplexers, the obtained results once again prove that the light paths within the proposed and studied GPhC area are sensitive to wavelength tuning.

3.2.3. Four-channel demultiplexing

These above demultiplexing configurations were chosen based on a simple configuration (90°-bending structure) with a square lattice and one particular air hole profile, for two-wavelength channel structures. To improve their operation and add several channels, we come back here to the 270°-bending structure which was presented in Fig. 3.9.

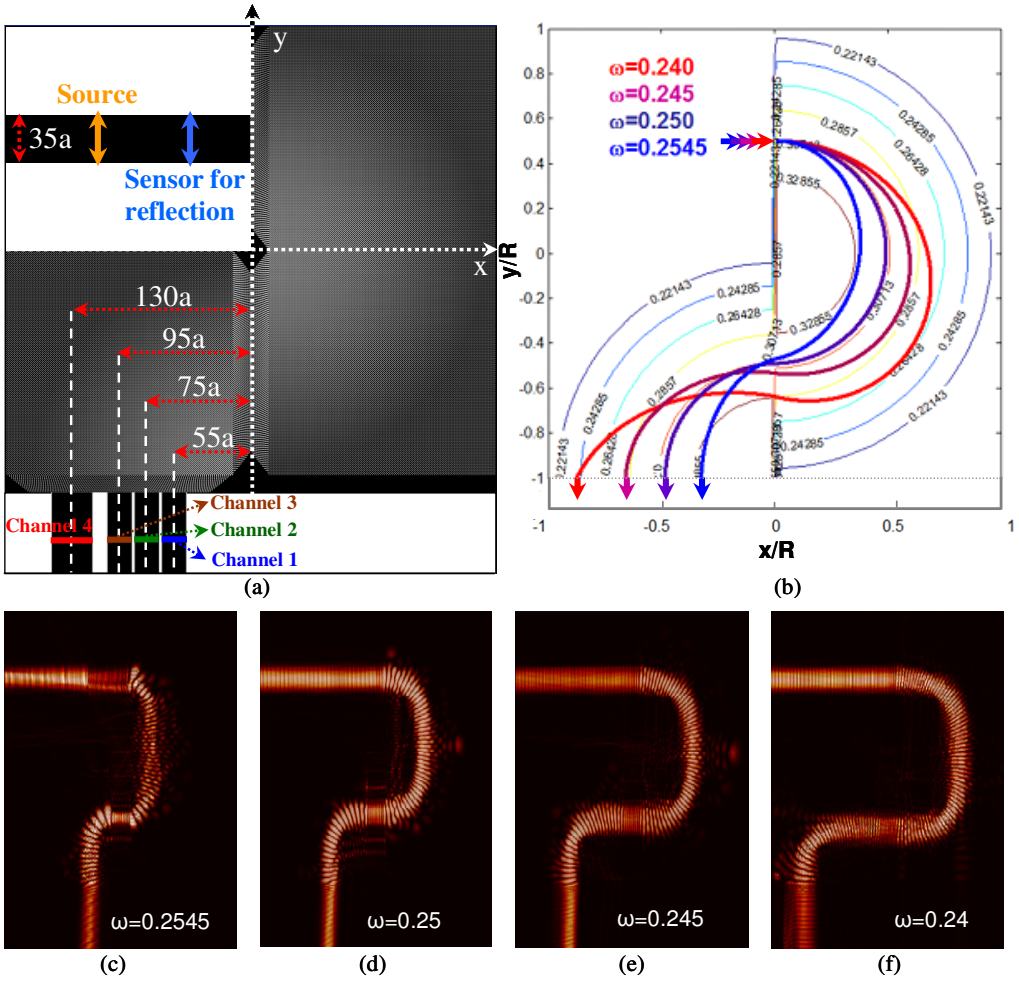

Figure 3.14: Dielectric permittivity diagram of a four-channel demultiplexing device based on 270°-bending graded photonic crystal configuration; (b) Ray trajectories obtained for four frequencies $\omega_1 = 0.2545$, $\omega_1 = 0.25$, $\omega_1 = 0.245$, and $\omega_1 = 0.24$, (c), (d), (e) and (f) Light paths of a Gaussian beam of 7a beam waist at four frequencies $\omega_1 = 0.2545$, $\omega_1 = 0.25$, $\omega_1 = 0.245$, and $\omega_1 = 0.24$, respectively, inside the studied device simulated using the FDTD method.

This structure was simulated using FDTD simulation. Input/output waveguides were considered (Fig. 3.14(a)) and placed at the predicted positions obtained from Hamiltonian optic simulation. Fig. 3.14(b) presents light trajectories of four frequencies $\omega_1 = 0.2545$, $\omega_2 = 0.25$, $\omega_3 = 0.245$, and $\omega_4 = 0.24$ obtained by Hamiltonian optics propagation method, while Figs. 3.14(c), (d), (e) and (f) show the steady-state fields obtained for the four chosen wavelengths using FDTD simulation. The demultiplexing operation is visible by the left to right shift of the beam for decreasing normalized frequencies.

Fig. 3.15 shows the calculated transmission spectra for the proposed four-channel demultiplexing in the 0.240 to 0.2545 frequency range. The overall insertion loss is around -3dB for each of the four channels, while inter-channel crosstalk is around -10dB.

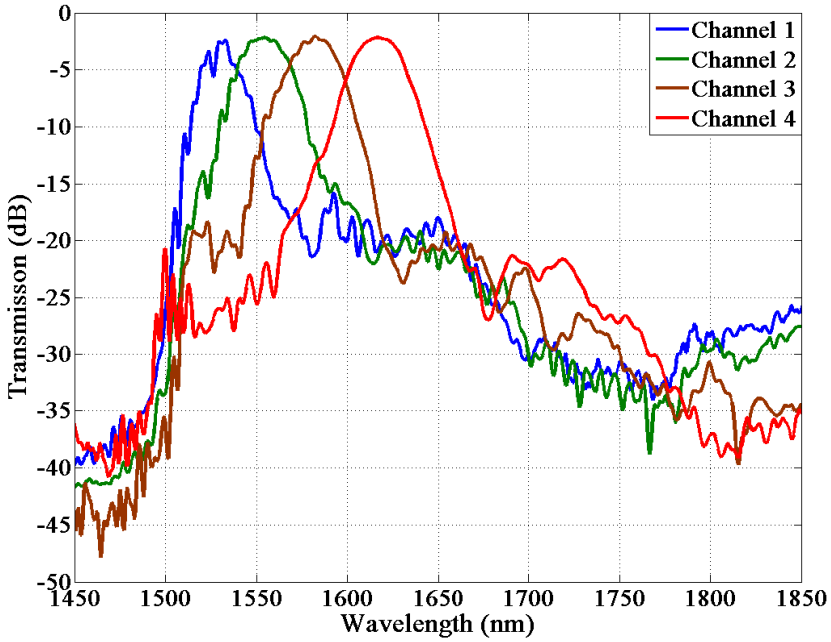

Figure 3.15: Demulitplexing operation of the proposed four-channel demuliplexing device

Simulation results on the properties of wavelength-sensitivity of the proposed GPhC configuration as well as the possibility of applying this property into demultiplexing purpose are the preparation basis for the fabrication and characterization steps that will be introduced in chapter 4. We also see that, even with a particularly simple profile of the GPhC filling factor, we already have some richness on controlling light in the configuration.

3.3. Polarization properties of graded photonic crystals

Polarization properties and managing the light polarization in photonic circuits are important issues in the on-going development of integrated silicon photonics. The aim consists in separating, managing the two polarizations of light (polarization splitting) and/or converting one polarized light to the other one (polarization convertion). In the context of polarization beam splitting, polarization modal

birefringence property in SOI waveguides, which is due to the strong index contrast between the waveguide core (Si) and cladding (air or SiO_2), is mostly used. This property has been exploited for the design of various polarization beam splitters (PBS) based on directional couplers (DCs), which coupling gaps and lengths were optimized to drop only one polarization on the DC cross port [27, 28]. One drawback of this approach is related to the tight required control of inter-waveguide gaps, coupling lengths, and waveguide cross-sections to ensure reasonable bandwidth, low inter-polarization crosstalk, and low insertion loss [29].

Another approach to design PBS is based on the use of planar photonic crystals (PhCs) which are known to have strongly birefringent properties. Several solutions have been explored in this direction, including the use of the superprism effect [30], polarization-dependent refraction [31], and bandgap frequency sensitivity to light polarization [32, 33]. As mentioned in Ref. [33], the straightforward implementation of this concept for the design of PBS proved to be ineffective. The reason for this is due to in-plane diffraction frequently occurring due to the grating-like interface between the optical slab waveguide and the 2D PhC area. In addition to this, optical beams tend to significantly spread into the corrugated medium. The most effective adopted approach to circumvent these drawbacks was to consider PhC heterostructures with all PhCs operating in self-collimating regime in addition to the bandgap property for TE/TM splitting [32, 33].

With respect to our work, as presented so far in the thesis, we have already considered the propagation of light in graded photonic crystals and also their wavelength dispersion properties. Yet, for all of those, results have been presented for only *one polarization* of light where the electric field is on the x-y plane, and the magnetic field is perpendicular to it (TE polarized light). Since the considered GPhC structures are also based on the SOI platform, we are sure that the configuration would also be sensitive to the polarization of light and with some potential interest for TE/TM polarization splitting. In the following, the study and exploration of polarization properties of the considered GPhC configuration is presented.

We started with the band diagrams for the two polarizations (red lines for TE polarization and blue dash lines for TM polarization) calculated using the MIT Photonic Band (MPB) software, as shown in Fig. 3.16a. The calculations were performed for a 2D square lattice with normalized radius of air hole r/a=0.31 in SOI material with effective refractive indices of 2.95 and 2.267 for TE and TM polarizations, respectively.

As well known, we can see in Fig. 3.16(a) the difference on frequency ranges between the first bands of TE and TM polarized light. The maximum frequency of the first TM band is much higher than the maximum frequency of the first TE band.

Figs. 3.16(b) and 3.16(c) show more clearly this difference by presenting the EFSs in the 1st Brillouin zone of the first TE and the first TM bands, respectively. As can be seen, EFSs of the first band for the two light polarizations are nearly circular close to M-points and turn to square shapes as farther to the M-point. The difference here is that frequencies having circular-shape EFSs are higher in the case of TM polarization (around ω=0.31) in comparison with those of TE polarization (around ω=0.255).

As the group velocity of light is normal to the EFSs, this difference in band diagrams will make light of the different polarizations at that range of frequencies propagate with different trajectories.

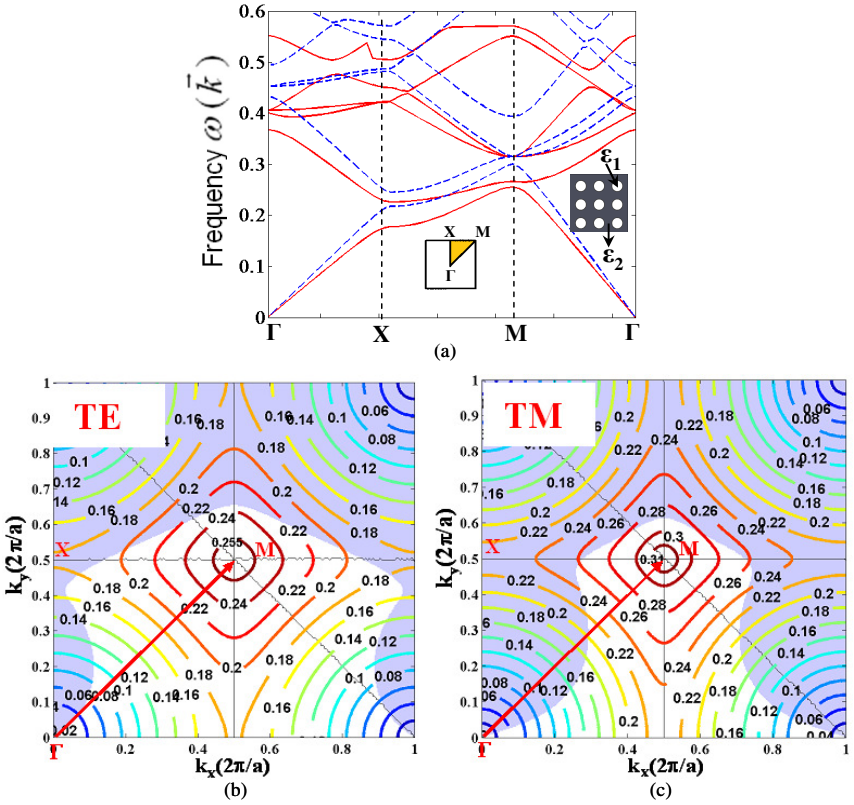

Figure 3.16: Equi-Frequency Surfaces of the first band in (a) TE light polarization and (b) TM light polarization of a square lattice photonic crystal made of air holes with normalized radii r/a=0.31 in a 2.95 (for TE) and 2.267 (for TM) effective index slab waveguide.

It was shown that this configuration makes TE polarized light beam bended by 90° in a frequency range of 0.22-0.26. As can be seen in the EFSs map for the first TM band, in this range of frequencies, the concavity of the EFSs is different from the one of the TE polarized waves (the concavity being positive in case of TM polarization whereas negative in case of TE polarization). It is thus predicted that TM-polarized light goes straight forward while TE-polarized light is bended to make a curvature path.

To verify the above prediction, the propagation of TM light beam in the proposed GPhC configuration was simulated using FDTD simulation. Figs. 3.17(a), (b) and (c) show the EFS diagram for the first TE and TM band, respectively. Figs.3.17(d) and (e) show the simulated energy distribution within the GPhC structure excited by TE and TM polarized Gaussian beams at same frequency ω=0.25 (λ=1550nm), respectively. It is shown that TE and TM light are separated into two different paths with a separation angle of 90°: TE light is bended towards the center point, while TM light goes straightly to the right. Hereinafter, we call the output for collecting bended light beam being the ***bended channel*** and the ***straight channel*** referring to the output on the right.

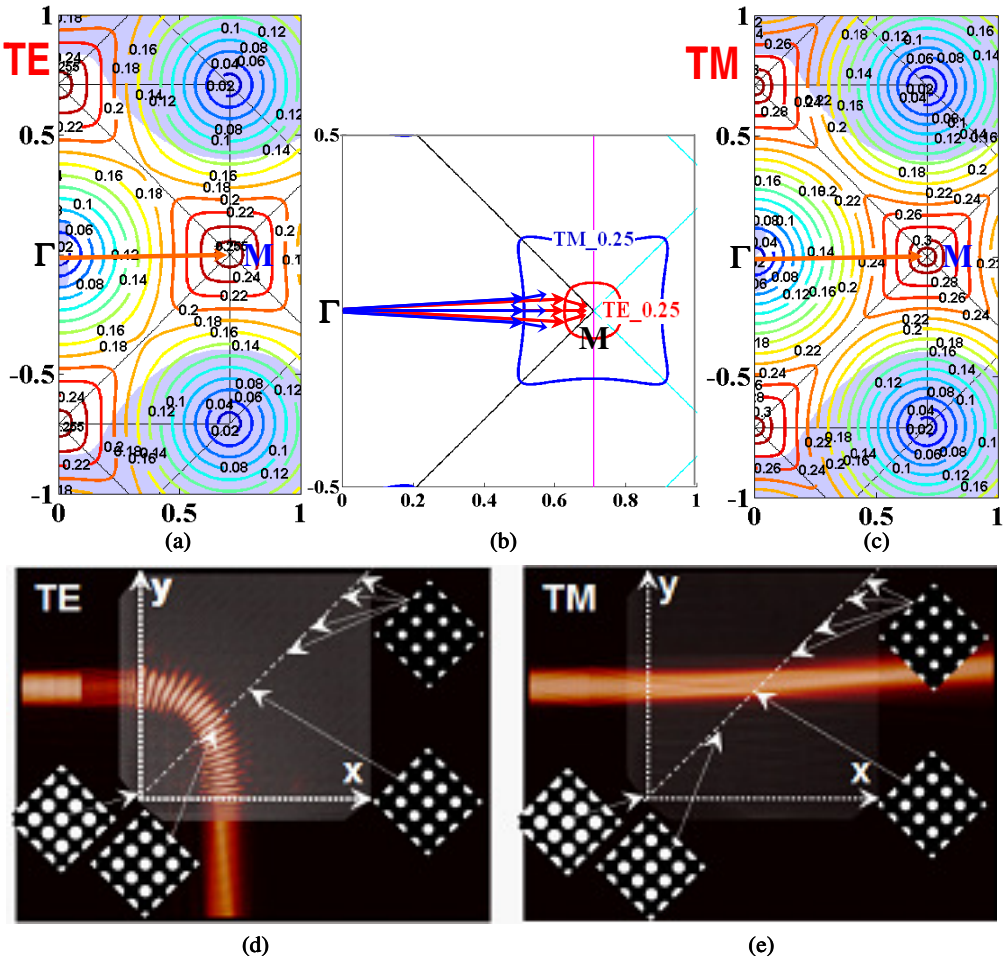

Fig. 3.17: (a), (b) and (c) EFS diagram of the first TE and TM band of the square lattice photonic crystal considered at the incident point $y(0)=R/2$. FDTD simulation of the propagation of TE-TM polarized light in the considered graded photonic crystal configuration with input/output tapers: (d) propagation of TE light and (e) propagation of TM light at ω=0.25 (λ=1552nm).

Transmission and reflection spectra for both polarizations are presented in Fig. 3.18. As figured out in Fig. 3.18(a), the blue and the green curves stand for power transmission of TE polarized light at the bended channel and at the straight channel, respectively.

One can see that at the bended channel power transmission of TE polarized light is as high as 95% in the frequency range ω=0.22 to 0.26. In case of TM polarization, light can be transmitted and collected at the straight channel with high transmission (power transmission is almost 100%) in the frequency range of ω=0.2-0.28 whereas at higher frequencies, transmission of TM light at the straight channel drops and can be collected at both two channels. This result is in good agreement with the above discussion, i.e. at high frequencies (i.e near M-point, and EFSs for TM polarization transform to circles), TM light is bended with the same principle as TE light polarization at lower frequencies (around 0.25).

The result shows that the proposed 90°-bending GPhC configuration can serve as a *polarization beam splitter*.

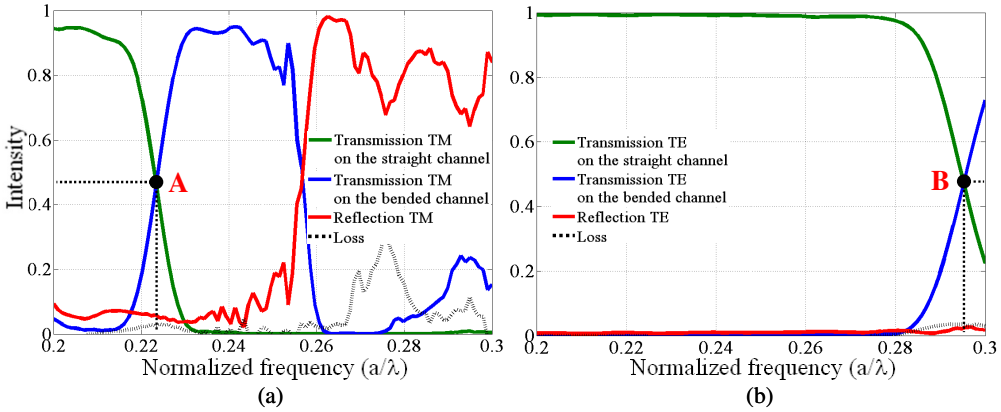

Figure 3.18: Polarization sensitivity of the proposed GPhC structure (a) Transmission of TE mode and (b) Transmission of TM mode of the proposed GPhC structure

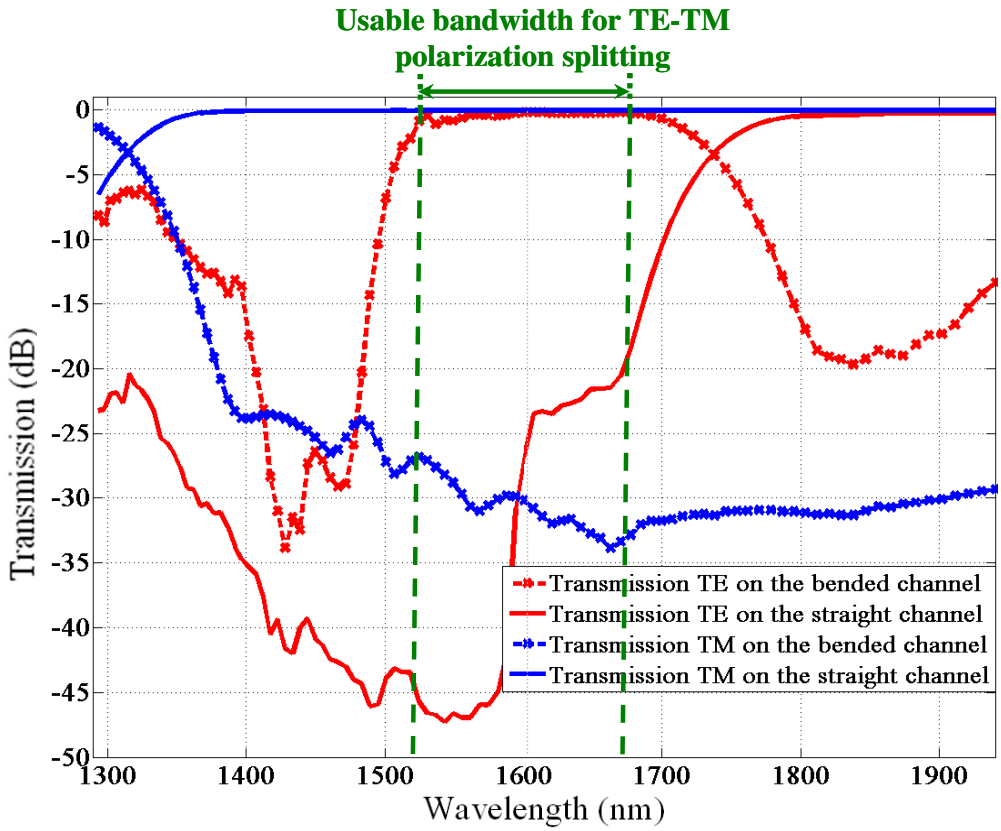

Figure 3.19: Crosstalk between TE-TM polarized lights in the proposed polarization beam splitting configuration.

The quality of a polarization beam splitter is decided by not only the high power transmission for both polarizations but also the low crosstalk of one polarization on the channel of the other one. We can see in Fig. 3.19, the insertion losses for both polarizations at two channels are lower than 0.5dB for the wavelength range of 1500nm-1680nm. And in this wavelength range, the crosstalk of TM polarization on bended channel is smaller than -30dB and the crosstalk of TE polarization on the straight channel lower than -22dB. This shows that this

configuration can probably operate with high efficiency in a large bandwidth of 180nm.

Beside the polarization splitting property, there is an interesting information contained in the transmission spectra of TE and TM light polarization of the proposed configuration presented in Fig. 3.18: the two light polarizations can be independently collected at the two output channels (straight and bended channels) with similar intensities (nearly 50%/50%). It is around the frequency ω=0.225 for TE light polarization and ω=0.295 for TM light polarization. These frequencies are the thresholds at which the configuration roughly transits from the homogenizable regime to the diffractive regime for each of the two polarizations. We will come back later and discuss this point in chapter 4.

3.4. Conclusion

Pursuing the approach presented in chapter 2, modeling and simulations of light propagation in graded photonic crystal structures have been realized in this chapter.

Simulations have been restrictively applied to one single simple case: a 2D-chirp (Gaussian profile) of the air hole filling factor of a square lattice photonic crystal operating in the first band. Despite its simplicity, this configuration is already rich in the potential it brings to shape electromagnetic fields at optical frequencies.

Light propagation in given configurations was simulated using the method of Hamiltonian optics and then verified using FDTD simulation, showing an excellent agreement between the simple ray propagation and the full electromagnetic computation, meaning that ray propagation relying on analytical dispersion relationships is a powerful method to predict electromagnetic mechanisms in complicated configurations.

Sensitivity of light paths to optical wavelength was studied, and demultiplexing issues were also explored. A possible structure using the studied square lattice GPhC has a typical surface 160a-length (61µmx 61µm) with two output wavelength channels was proposed to operate at wavelengths around 1550nm. A configuration for four-wavelength demultiplexing was also proposed.

The polarization properties of the studied graded photonic crystal configuration have been also explored. Simulation results show that the two polarizations of light are well separated by 90° after propagating through the studied graded photonic crystal configuration. The proposed polarization beam splitter designed on a silicon on insulator platform with high power transmission for two both polarizations (i.e. low insertion loss) and low crosstalk can be seen as an efficient polarization splitter.

These interesting properties inside a simple configuration of graded photonic crystal shows the possibility to envisage in future works more complicated 2-D chirps of PhC parameters using the same method to produce more advanced functions.

These simulations are the first step that enables us to design and fabricate devices based on the proposed GPhC configuration. The contents on design, fabrication and characterisation of GPhC devices are presented in chapter 4.

Chapter 4

Fabrication and Characterization of Graded Photonic Crystals

This chapter is devoted to the presentation of the fabrication and the experimental investigation of graded photonic crystal structures proposed in last chapters and achieved during this thesis.

With the aim of experimentally investigate the simulation results on the super-bending effect, and the dispersive and polarization-dependency properties of the considered GPhC configurations, the fabrication process has been first realized in the CTU IEF/Minerve clean room of the Institute of Fundamental Electronics (IEF) laboratory with the great involvement of Xavier Le Roux. Then, the characterization phase has been performed at two different places including the *Micro-Nanophotonique group* (*MINAPHOT)* IEF group and the *Groupe de Champ Proche Optique*, Laboratoire Inter-disciplinaire Carnot de Bourgogne (ICB).

The fabrication of GPhC samples will be presented in the first part of this chapter. It was done using e-beam lithography (EBL) and Reactive Ion Etching (RIE) technologies. In this process, we carefully took into account the proximity effects in the design and e-beam exposing stages, which were previously presented in the PhD manuscript of Damien Bernier, a former PhD student of the *MINAPHOT* group. During this thesis, we pursued these technological efforts for the fabrication of GPhC structures in which photonic crystal parameters slowly and gradually vary. SEM images of GPhC samples prove that our technical parameters are reasonable to well define the GPhC structures in the range of this thesis.

Various samples have been designed and fabricated including:

- A normalization-sample without GPhC area in order to evaluate the transmission efficiency and insertion losses of light propagating though the sample from the input to the output fibers of the butt-coupling experimental setup, including the full strip waveguide circuitry.
- Samples of GPhC configurations with the air-hole filling factor profile mentioned earlier in chapter 3 and with and without input/output tapering

regions. These samples were prepared for testing the light bending effect in GPhC structures.

- Samples of the several GPhC configurations with several output waveguides for investigating the demultiplexing performances of the studied GPhC configurations.

The second part of this chapter is to present the obtained experimental results from the fabricated GPhC devices. First, far field measurements using an optical bench were utilized to investigate the GPhC transmission efficiency and to experimentally investigate the super-bending effect at optical frequencies. This stage was carried out using the facilities in *MINAPHOT* group of IEF. The second method – based on Scanning Near-field Optical Microscopy (SNOM) was performed at *ICB* and allowed providing the direct observation of the light bending effect in the studied GPhCs, as well as the analysis of GhC dispersive properties and the possible observation of the transition between the homogenizable and dispersive regimes of light propagation in the investigated GPhC structures.

4.1. Description of fabrication process of considered GPhC structures

The techniques used for the fabrication of GPhC structures are presented in this section. The fabrication objective was to define precisely photonic crystal elements with lattice period around 400nm. In microelectronics, the technique of lithography is often used for the reproduction of a pattern onto a support. Several lithography technologies can be used to define photonic crystal structures, mainly including deep UV Optical lithography (DUV) and Electron Beam Lithography (EBL). EBL was chosen since it provides the reasonable necessary resolution and a versatility in designing the structures since it does not require a physical mask.

Our main technique was based on the electron beam lithography process using the RAITH150 system available in the CTU IEF-Minerve clean room.

The fabrication process of each GPhC structure contained generally three main stages:

1) First, an electronic mask was designed and created (based on the parameters mentioned in chapter 3) that was loaded into the RAITH150 system to serve as a mask in order to define the structure pattern onto a SOI wafer.
2) The second stage was the lithography process to insolate the structure by a scanning of an electron beam controlled by the equipment system.
3) The last stage was the etching step to transfer the structure pattern into the SOI substrate.

The detailed steps of the employed fabrication process will be figured out in the last part of this section after the general introduction of the fabrication techniques.

4.1.1. Mask design

GPhC samples were designed based on the proposed configuration of GPhC mentioned in chapter 3 with a maximum normalized air hole filling factor of *r/a=0.35* and a minimum normalized air hole filling factor of *r/a=0.22*. In practice, the lattice parameter was chosen as $a \approx 390nm$. Thus, the variation of air hole size ranged from *r=136 nm* down to *r=85nm,* as figured out in Fig. 4.1. The photonic crystals have been fabricated by starting with a SOI wafer with a silicon layer of 260nm thickness and a 2µm thick buried oxide layer.

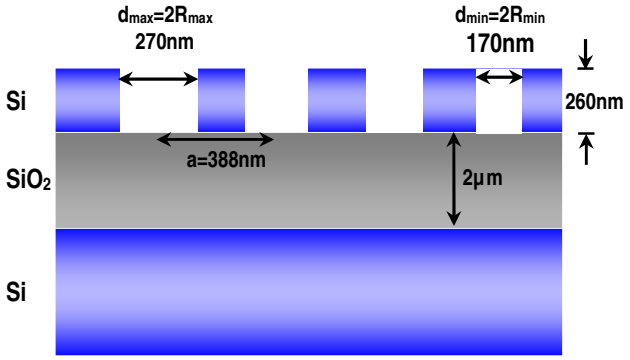

Figure 4.1: Schematic diagram of the main min/max dimensions of the air hole GPhCs

In practical point of view, we intended to use the optical bench facilities in our group for the characterization of the fabricated GPhC structures. This optical bench will be introduced in detail in the following section. In brief, we will adopt the butt-coupling technique where the input light is injected into the fabricated samples through a lensed-fiber. Then, output light is collected at the other side of the sample.

This practical employment led to the following requirement parameters:

- The sample (chip) needs to have a *3mm* to *4mm* length,
- Input and output waveguides are needed for the injection and collection of light, respectively.

Taken these conditions into account, we have designed the GPhC samples which are amenable to characterization as shown in Fig. 4.2 and Fig. 4.3. As can be seen in Fig. 4.2(a), the window is referred to the overall sample of *3mm*x*4mm* (width x length) size. We have added strip waveguides into the considered GPhC configuration (blue area). The strip waveguide circuitry was chosen to provide the lowest possible losses and operate mainly on the waveguide fundamental mode. Its parameters were optimized as following:

- For the purpose of injecting and collecting light into/from the GPhC structures, we needed first the access (input) and output waveguides. They were chosen as strip waveguides of *3µm* width.
- To filter out high order optical modes and guarantee, as best as possible, the single-mode excitation of the final waveguide enlightening the GPhC, a waveguide of *400nm* width was included into the photonic circuit.
- To excite the Bloch modes of the GPhC structures, the access waveguide close to GPhC area was chosen with a width of *15µm*.
- Various strip waveguides were introduced, with width varying from *400nm* to *15µm*. Some tapered waveguides were thus introduced in order to connect these waveguides. The length of each tapered waveguide was chosen to minimize the optical losses.

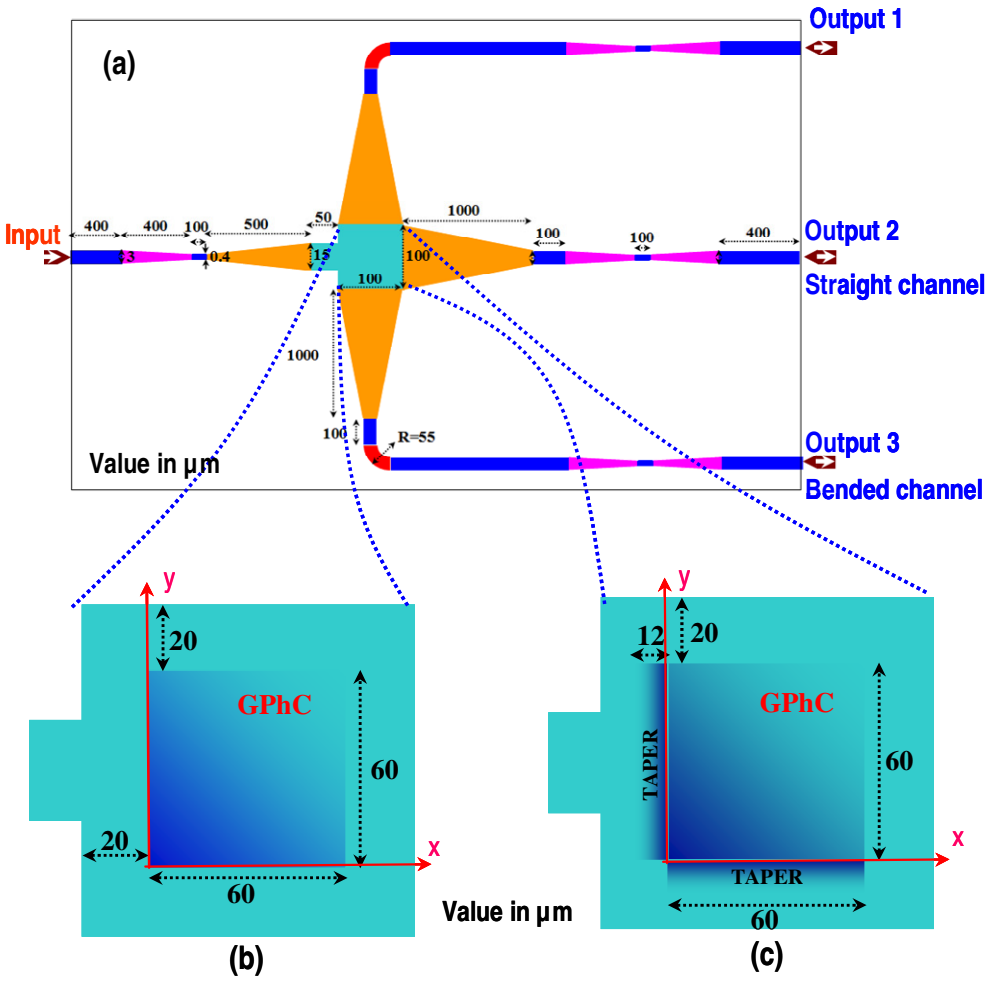

Figure 4.2: Dimensions of GPhCs structure present on the designed mask: (a) Overall view of the fabricated GPhC structure with input and output waveguides, (b) Dimension of the GPhC part and (c) dimension of the GPhC part in case of adding input and output tapering regions to the graded photonic crystal. This design is aimed to characterize the overall transmission of the GPhC configuration.

- Since the butt-coupling technique is used for the optical characterization of samples, input and output waveguides needed to be oriented horizontally with respect to the lensed-fiber. That is the reason why we chose the design of sample with the overall shape presented in Fig. 4.2(a). From simulation results presented in the last chapter, we expected to collect light power after the bending effect, which is the output 3 as figured out in the figure. To do that, a bending waveguide of 3µm width with a curvature of R=55µm was inserted. Hereinafter, we will call this output the ***bended channel*** since it corresponds to the light collection output after light propagation and bending through GPhC area. Output 2 is the straight channel to collect light that goes straight forward after entering into the GPhC area. To verify if unexpected phenomena could also occur, an upward output channel was also considered in the design (output 1).

Figs. 4.2(b) and (c) show the dimensions of the GPhC area containing the "reference" GPhC configuration in the cases of without or with tapering photonic

crystal regions, respectively. This GPhC structure was intended to investigate the overall power transmission out of the bended channel.

For the study of the dispersion properties of the GPhCs, other GPhC samples were designed as shown in Fig. 4.3.

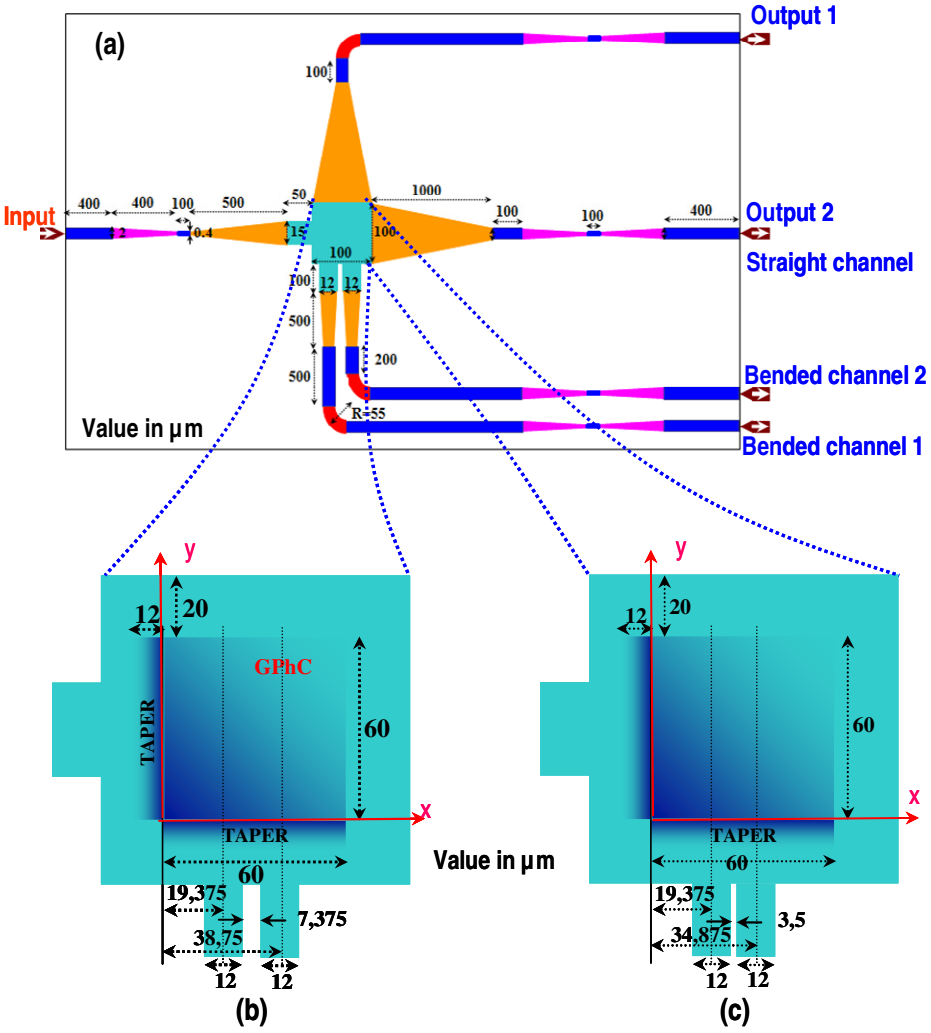

Figure 4.3: (a) Schematic diagram of the GPhC samples to be fabricated and characterized with two-wavelength channels corresponding to two output waveguides, and (b) Dimensions of the GPhC part and of the two output channels.

Two bended output waveguides (or two bended channels) were added to replace the only bended channel previously collecting the overall transmission as mentioned in Fig. 4.2. These two bended channels were placed at the proper positions relying on the calculations and predictions reported in chapter 3 using the ray tracing Hamiltonian optics- assisted and FDTD simulation methods.

These parameters were included in an electronic file defining the structures being fabricated, ready to be loaded into the RAITH150 system for the next stage.

4.1.2. Fabrication process in CTU clean room

4.1.2.1. Overview of fabrication process of the GPhC sample

The process we employed for the fabrication of the studied GPhC structures is schematically presented in Fig. 4.4.

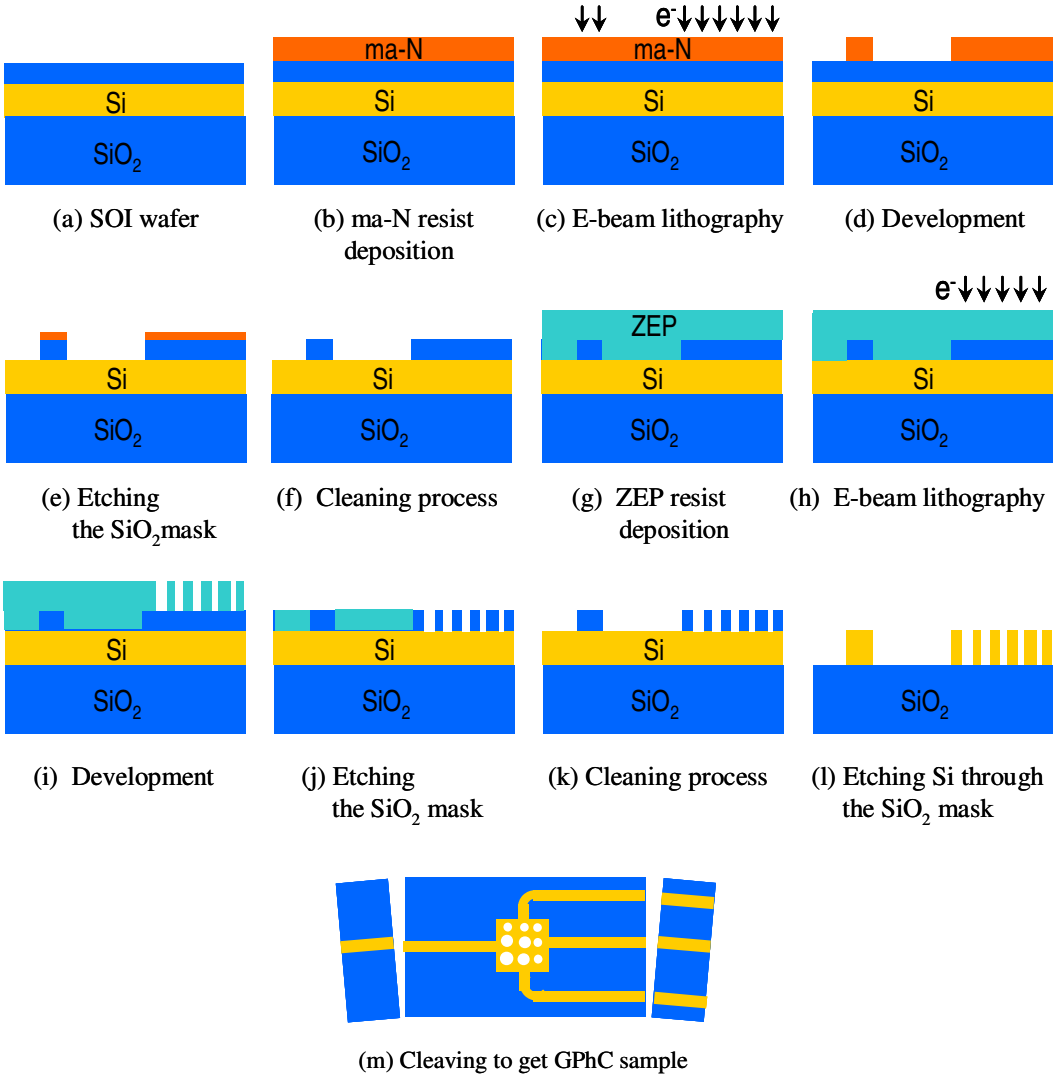

Figure 4.4: Overview of fabrication process of studied GPhC structure: (a) starting from a SOI wafer with 260nm-thick silicon and 150nm SiO2 on top, (b) to (f) Reproduction of the SiO2 mask for waveguide system, (g) to (k) Reproduction process of the SiO2 mask for photonic crystal area, (l) Transfer the structure pattern onto silicon layer, and (m) Cleaving the edge to get the GPhC sample ready for characterization

We started with a SOI wafer of diameter *Φ=6inches*, with a 260nm of silicon (Si) layer and a 2µm buried silica (SiO_2). The wafer was treated to have a SiO_2 layer of 150nm-thick on top of the Si layer. This SiO_2 layer was used as a hard mask to transfer the pattern of studied configuration onto the Si layer as seen in Fig. 4.4.

The fabrication of GPhC sample (with the strip waveguide circuitry mentioned above) was achieved as following:

1) First, strip waveguides were defined using the RAITH150 e-beam process using the negative resist *ma-N2403* as following (Fig. 4.4(b) to (f)):
   - Deposition of *ma-N2403* (Fig. 4.4(b)) on SOI wafer using a spin-coating technique in *t*=30s, with the rotation speed *v*=3000rpm. The wafer was then placed on a hot plate of 90^{o} in 90s. It then had a *ma-N* resist layer of *400nm* thick.
   - Insolation of the designed pattern of the waveguide circuitry and of the overall GPhC area using the RAITH150 e-beam lithography system. (Fig. 4.4(c))
   - Development of the studied structure in *AZ726MIF* solvent in 30s (Fig. 4.4(d)).
   - The photoresist pattern was then transferred to the 150nm thick top silica layer using a reactive ion etching system (Fig. 4.4(e)).
   - Cleaning the sample using H_2SO_4:H_2O_2 and O_2 plasma (Fig. 4.4(f)).
2) The photonic crystal structure was then separately insolated by means of a lithography process with the positive resist ZEP520A (Fig. 4.4(g) to (k)):
   - Deposition of ZEP520A (Fig. 4.4(g)) on the sample using a spin-coating technique in *t*=30s, with the rotation speed *v*=5000rpm. The wafer was then placed on a hot plate of 170^{o} during 3 minutes. The sample then had a positive resist layer of around 300nm thick.
   - Insulation of the designed pattern of GPhC using the RAITH150 e-beam lithography system. (Fig. 4.4(h)).
   - Development of the studied structure in the ZED-N50 solvent during 40s, then in MIPK/IPA (1:3) solvent in *30s* (Fig. 4.4(i)).
   - The photoresist pattern was then transferred to the 150nm thick top silica layer using a reactive ion etching system to define the hard mask for the forthcoming etching of the GPhC area (Fig. 4.4(j)).
   - Cleaning the sample using H_2SO_4:H_2O_2 and O_2 plasma (Fig. 4.4(k)).
3) The silicon film was etched through a SF_6/O_2 anisotropic etching process (Fig. 4.4(l)).
4) After the cleavage step, the sample was ready for the optical characterization (Fig. 4.4(m)).

In the lithography process, the interaction of electrons with the resist and the substrate is responsible for several phenomena that disperse them in a wider area than that of the incident beam [34]. This leads to the so-called proximity effects that need to be considered and corrected in the lithography step. To overcome these effects, the exposure dose as well as the designed size on the mask are carefully taken into account.

Proximity effects in photonic crystal structures have been studied in the work of Damien Bernier during his PhD in the MINAPHOT group. During the present thesis, we pursed this task to allow the correct fabrication of structures in which photonic crystal parameters slowly and gradually vary in space.

In the following, we detail the related study of proximity effects in the fabricated GPhCs.

4.1.2.2. Proximity effecs in e-beam lithography process

We focused in the EBL process on the correction of proximity effects. To do this, we studied the *factor of dose* that is suitable for the optimization of the air hole photonic crystal diameter all over inside the GPhC area. Fig. 4.5 shows the result of this optimization process.

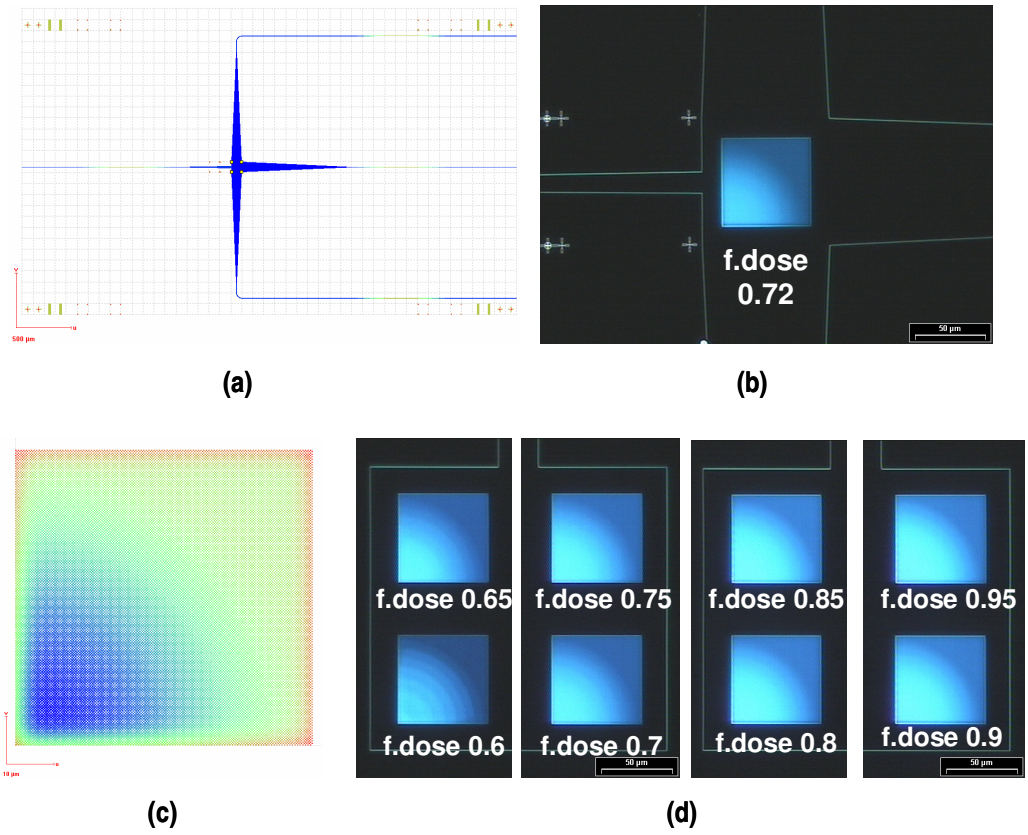

Figure 4.5: Study of the proximity effects in the fabrication process of GPhC areas: (a) Sample structure overview on the mask; (b) Image of GPhC area after the exposure of e-beam lithography process with the factor of dose 0.75 and with a dose correction (c), and (d) Effect of different studied dose factors.

Then, the sizes of the air holes in the different samples were characterized through SEM images by using the Alicona software. The measured values of difference GPhC fabricated with these above dose factors were compared with the designed sizes of the air holes on the mask.

Fig.4.6 shows the SEM images taken different regions (see the inset figure) of GPhC area fabricated with the dose factor of 0.75. The measured values of air holes are indicated in each Figs. 4.6(a) to (d).

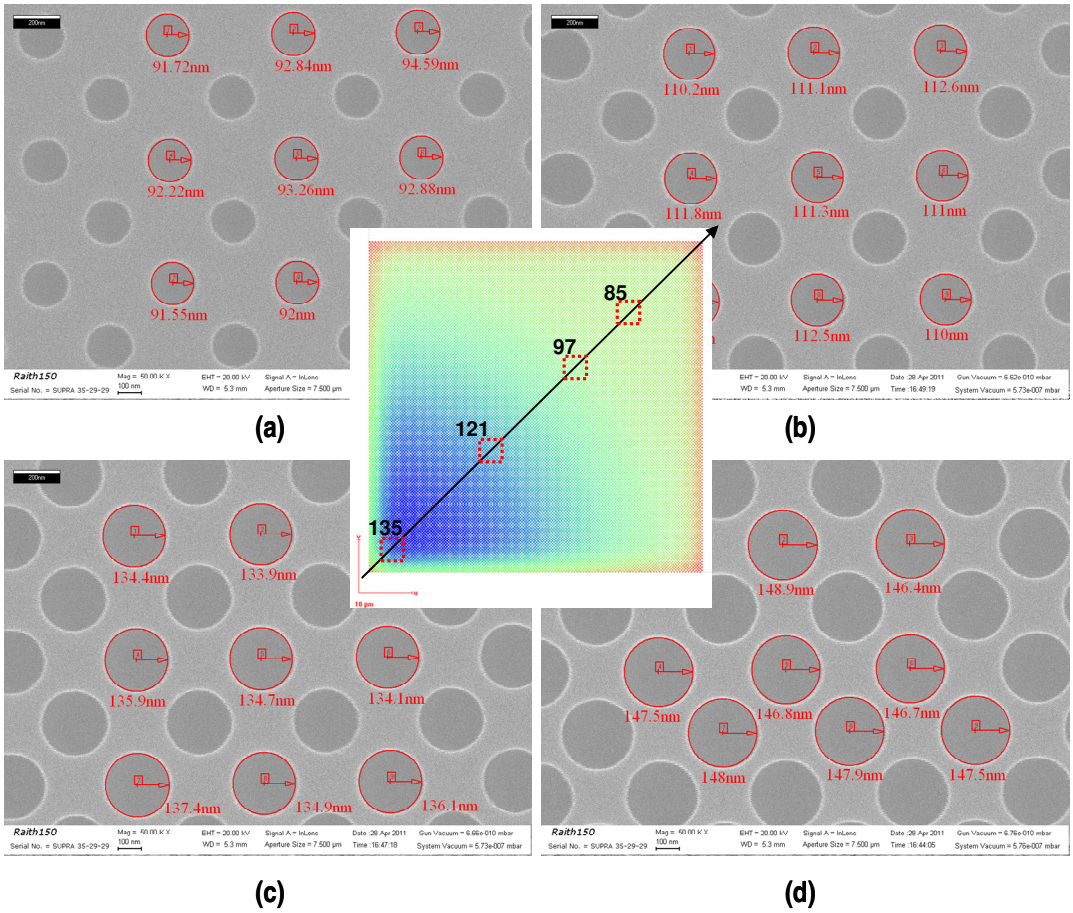

Figure 4.6: SEM images at different regions in the fabricated GPhC area with the *factor of dose 0.75* with measured values of air hole radii: (a) zone of fabricated air-holes of 92nm after correction on the mask, (b) zone of fabricated air-holes of 111nm, (c) zone of fabricated air-holes of 134nm, (d) zone of fabricated air-holes of 147nm.

Fig. 4.7 presents the relationship between the designed values of air hole on the mask and the measured ones. It can be seen that the difference between measured and designed values is linear when employing a factor of dose *0.75* with a shift around 14nm.

From this result, we reduced the designed sizes on the GDSII mask by *10nm* (due to the ±2nm resolution of Alicona measurement software) in order to get the expected sizes of air holes and match with the air hole profiles deduced from the simulation of GPhC structures presented earlier in this manuscript. This made possible the comparison between experimental results, which will be presented in the next section, and the simulation results already presented in chapter 3.

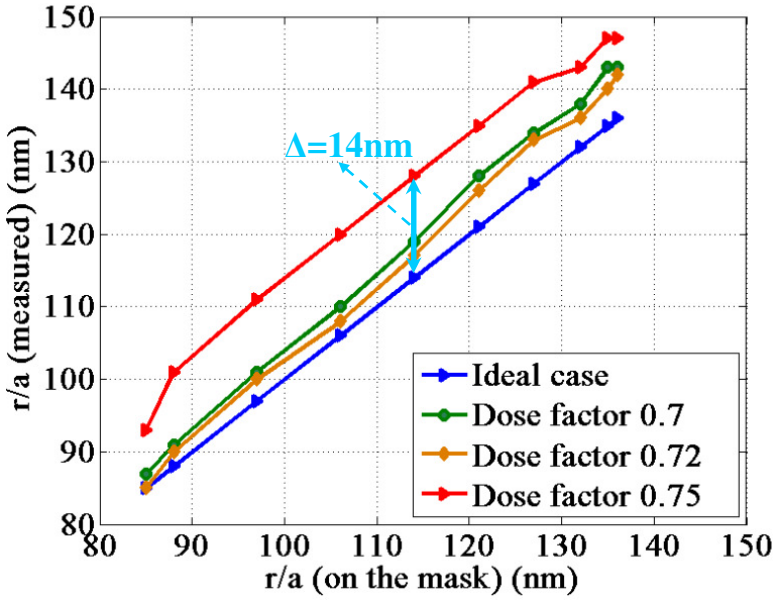

Figure 4.7: Relationship between the measured air hole radius (of different GPhC sample fabricated with dose factors of 0.7, 0.72 and 0.75) and the designed values on the mask. A linear relationship was obtained in the range of 90nm-130nm when employing the dose factor of 0.75.

4.2. Description of characterization benches

To characterize the fabricated devices, two methods were used: the far-field (*butt-coupling injection/collection of light*) and the near-field (*SNOM*) techniques which provided us an estimation of the transfer function of light as well as a visual evidence of super-bending effect inside our fabricated GPhC devices, respectively. In the following, the experimental setups employed in these two measurement methods will be described.

4.2.1. Experimental setup for the far-field measurement

Our first experimental characterization of fabricated devices was the far-field measurements which allowed the estimation of the optical transfer function of the GPhC structures. The optical bench setup for this measurement is shown schematically in Fig. 4.8. As described in the figure, first, light from a laser diode (namely Wavelength Tunable Laser Diode) with a broad wavelength range from 1390nm to 1620nm) was used as the source. Light from the laser diode was then injected into the MT9820 All-Band Optical Component Tester via an optical fiber, enabling the optical transmission measurement to be performed over the operating wavelength range with the chosen wavelength resolution of 8pm. From the output of the Optical Component Tester, signal was guided to a polarization controller to provide either TE or TM polarized light and then coupled into the fabricated GPhC device through an input strip waveguide of 3µm width by a taper-lensed fiber.

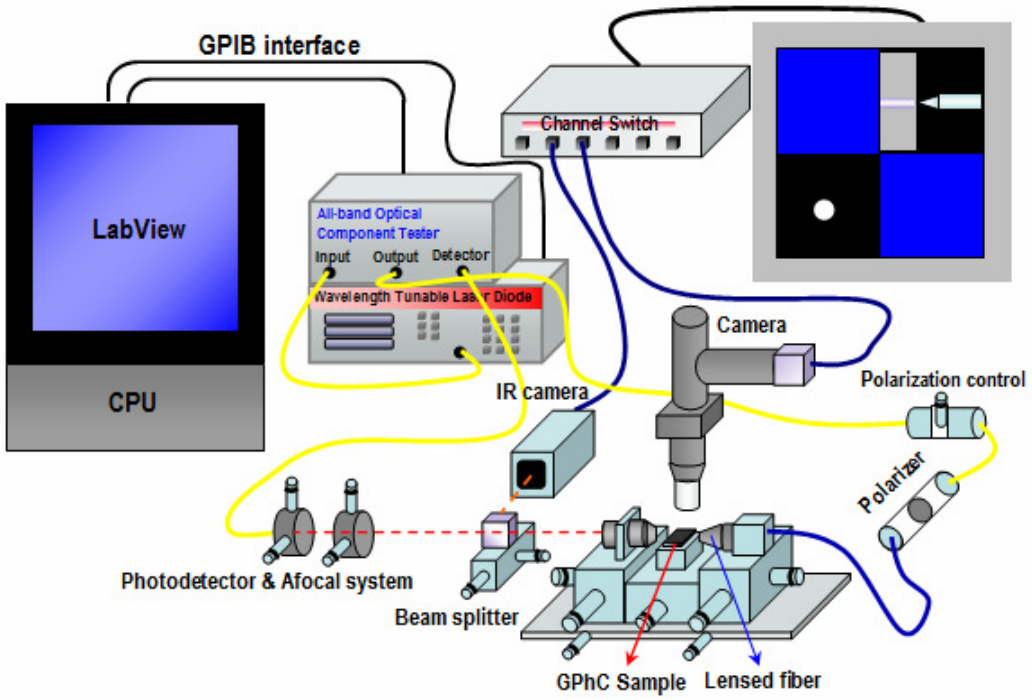

Figure 4.8: Schematic view of the optical bench (in *MINAPHOT*, IEF) for optical transmission measurement.

The fabricated GPhC device was placed on a holder in a photonic alignment system which provided the precise sample positioning, and the possibility to view the surface of the sample and the tip of the taper-lensed fiber on the screen by a microscope camera placed vertically above the sample.

Light at the output facet of the fabricated GPhC device was then collected by a microscope objective, then an afocal system and finally a detector. The signal received from the detector was subsequently sent to the MT9820 All-Band Optical Component Tester through a single mode optical fiber in order to measure the optical transfer function. This optical transfer function was determined by comparing the intensity of the input signal received from the tunable laser diode (the source) to the intensity of the signal received at the detector. The acquisition of the transmission spectra of the testing GPhC device was finally observed by a computer with LABVIEW software which is connected to both the laser source (tunable laser diode) and the optical measuring device (All-band Optical Component Tester).

4.2.2. Experimental setup for the near field measurement

The above mentioned far-field measurement setup enabled us to investigate the transfer function of light in the fabricated GPhC samples but not to visualize the flow of light inside the samples. Before my thesis, our group had been in collaboration with the research group of Frédérique de Fornel in Dijon which masters in Scanning Near-Field Optical Microscopy (SNOM). The collaboration results have provided a direct experimental observation of the beam propagation inside a photonic crystal superprism [35]. It was a precious chance for me to get in this collaboration to explore the property of our fabricated GPhC samples.

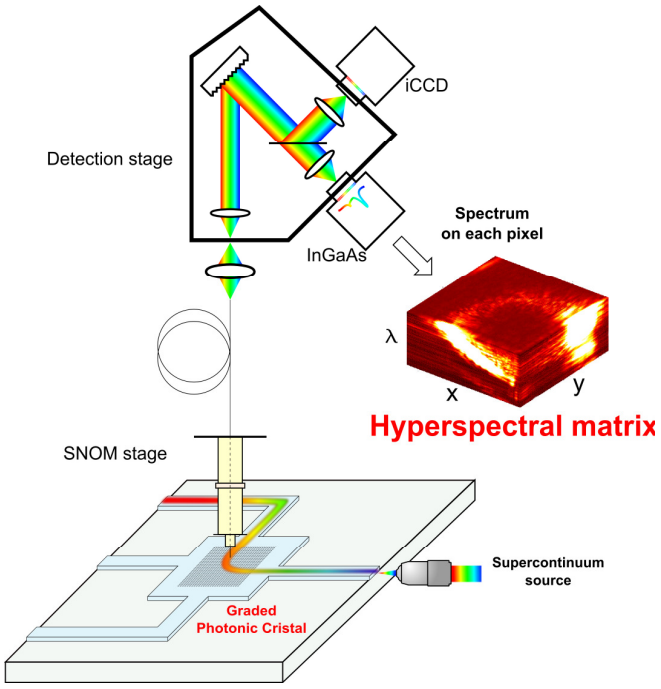

Figure 4.9: Overview of the Hyperspectral SNOM experimental setup (at ICB). The spectrum of light collected by the near-field probe during the surface scanning process was recoded at each pixel to provide a 3D hyperspectral matrix over the broad spectral range (1200nm-1650nm).

SNOM measurements were performed in the *Laboratoire Interdisciplinaire Carnot de Bourgogne (ICB*) by developing a hyperspectral scanning near-field optical microscope (Hyp-SNOM) using a broadband illumination and detection as proposed at visible wavelengths in plasmonics. It enabled the direct observation of light dispersion (here is the mirage effect) within our fabricated GPhC devices operating at optical wavelengths. The spectral and spatial dispersion could be also experimentally quantified from this measurement.

The experimental setup of the Hyp-SNOM measurement is schematically overviewed in Fig. 4.9. A supercontinuum laser source with an output power up to 0.1mW/nm was used as an intense broadband excitation over the spectral range of 400nm-1700nm. The evanescent decay of the light guided inside the GPhC sample was collected by a near-field probe made of a tapered single mode silica fiber placed at 4nm above the sample's surface. A free space spectrometer was then used to disperse the collected light and the spectra were recorded synchronously with the probe scan every 50ms on a cooled InGaAs camera for near-infrared wavelengths or on an intensified charge coupled device (iCCD) for visible operations.

In practical point of view, for silicon based materials, only near-infrared wavelengths above the Silicon electronic bandgap can propagate inside the SOI chip and thus in SNOM measurement, the near-field detection is restricted to the 1200-1650nm spectral range. The spectra of light guided inside the fabricated GPhC device which are collected by the near-field probe and recorded on each pixel provides a 3D hyperspectral matrix over a broad spectral (as shown on the right of Fig. 4.9).

Results obtained from these two methods were then analyzed and will be discussed and presented in the next section.

4.3. Results and discussions

4.3.1. SEM images of fabricated structures

Fig. 4.10 shows the detailed scanning electron microscope (SEM) images of a fabricated GPhC sample. We can see the overall structure of GPhC sample in Fig. 4.10(a), and several detailed SEM images from which the gradual profile in the GPhC area can be guessed (as in Fig. 4.10(b)).

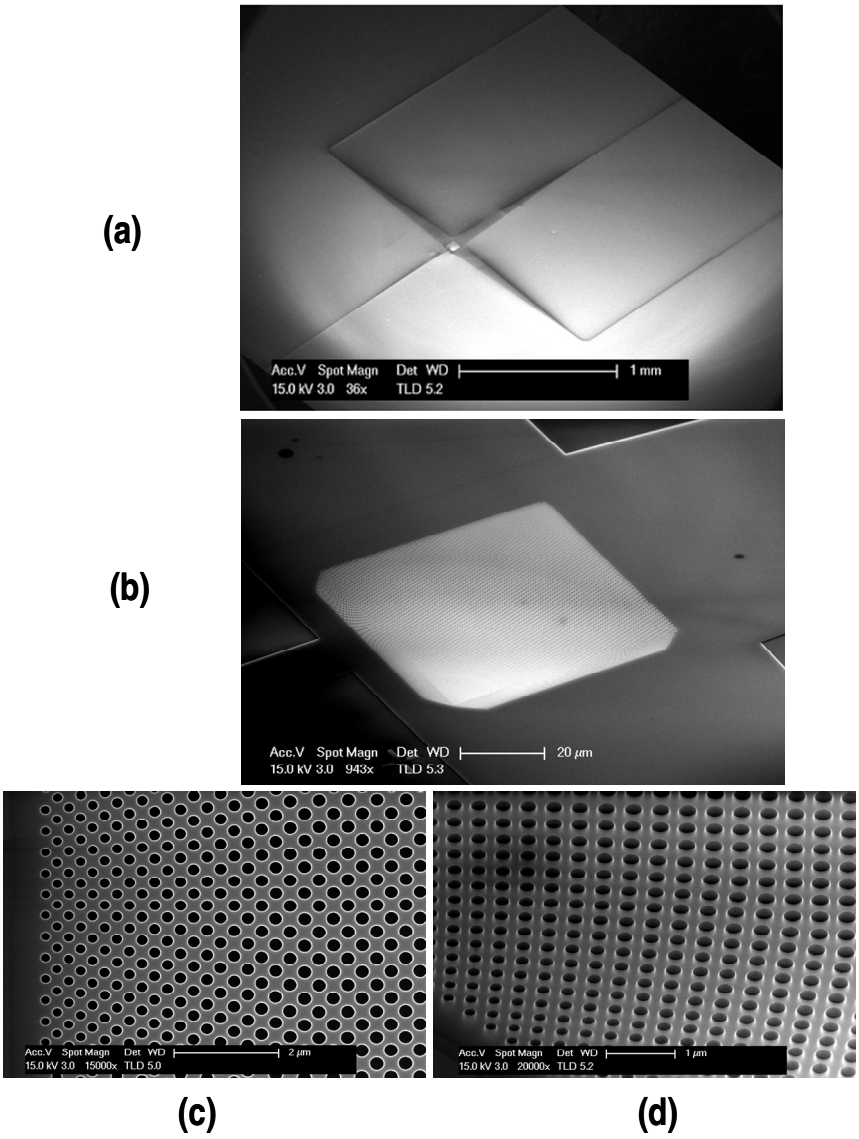

Figure 4.10: SEM images of a fabricated GPhC structure: (a) Overview of the fabricated sample, (b) GPhC area in fabricated sample, (c) and (d) Detailed views of tapering regions of the GPhC.

SEM images of the photonic lattice were also taken at different positions in the GPhC area, as seen in Fig. 4.10. These images show that the fabrication process at IEF was successful to define the considered GPhC configuration.

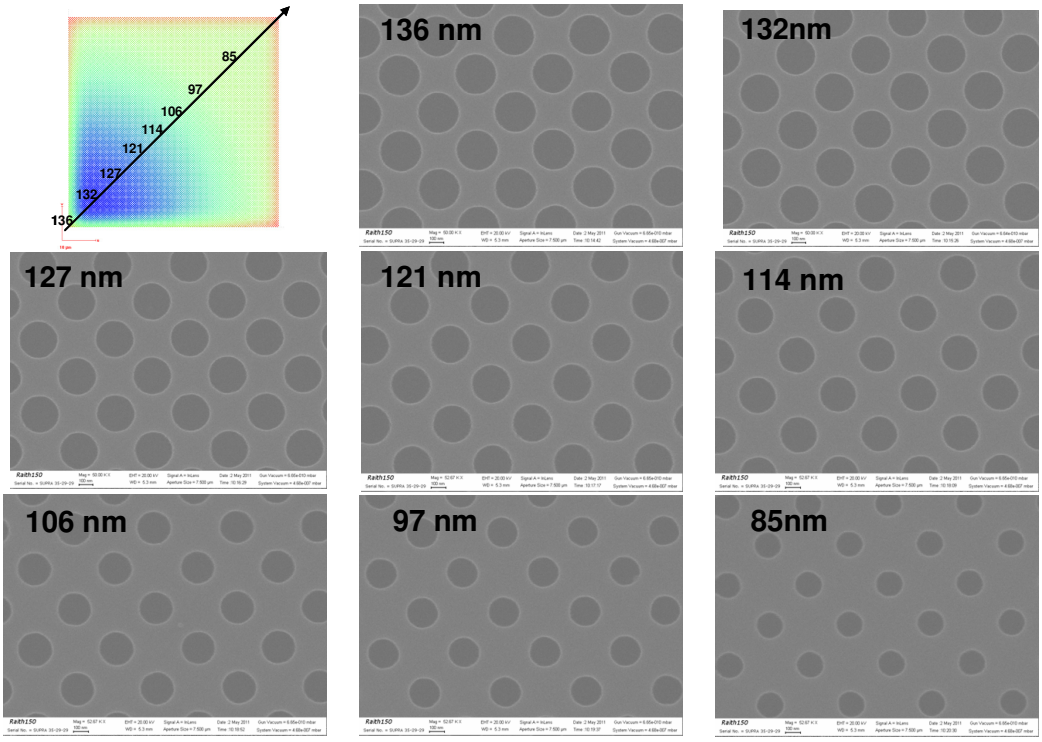

Figure 4.11: SEM images of the air hole photonic crystal lattice at different points of the fabricated GPhC area.

4.3.2. Experimental investigation of the optical mirage and super-bending effect in GPhCs

Using the experimental setup shown in Fig. 4.8, we first measured the transmission powers of TE polarized light through our three fabricated samples:

1) Sample of GPhC without any I/O taper,
2) sample of GPhC with I/O tapers,
3) and a normalization sample which is the same as the two above ones, but without any GPhC.

Signals from the outputs of the two samples with GPhC configurations were then normalized by the signal obtained at the output of the normalization sample to give the normalized transmission powers of the two GPhC samples. The normalized light transmission powers (for TE polarized light) through the fabricated GPhC devices (without and with input/output tapers) obtained at the bended channel by far-field measurement are shown in Fig. 4.12(a), in which the red and blue curves are for GPhC samples without I/O taper and with I/O taper, respectively. These curves can be compared with the theoretical results presented in Fig. 3.7(b) in chapter 3. Ripples observed in these two curves are due to Fabry-Perot resonances at the two edges of the whole sample.

Reminding that in our manipulation the transmitted light were collected at the bended output, it means that light is 90^{o}-bended and transmitted through the GPhC area, as can be seen from Fig. 4.12(a), with a low loss level. Although the

electromagnetic exploited modes are situated below the light line whatever the beam position is within the GPhC area, out-off-plane optical losses may arise due to the in-plane two-dimensional chirp of the photonic crystal filling factor. The low loss shown in these two curves is an experimental confirmation that out-off-plane losses remain at a small level in our fabricated GPhC samples. The insertion losses are slightly smaller for the GPhC sample with I/O tapers than for the GPhC sample without I/O tapers. This result is in good agreement with the prediction presented in chapter 3 and experimentally shows that the use of tapering PhC regions at the input and output of the GPhC area can enhance the light power transmitting through it.

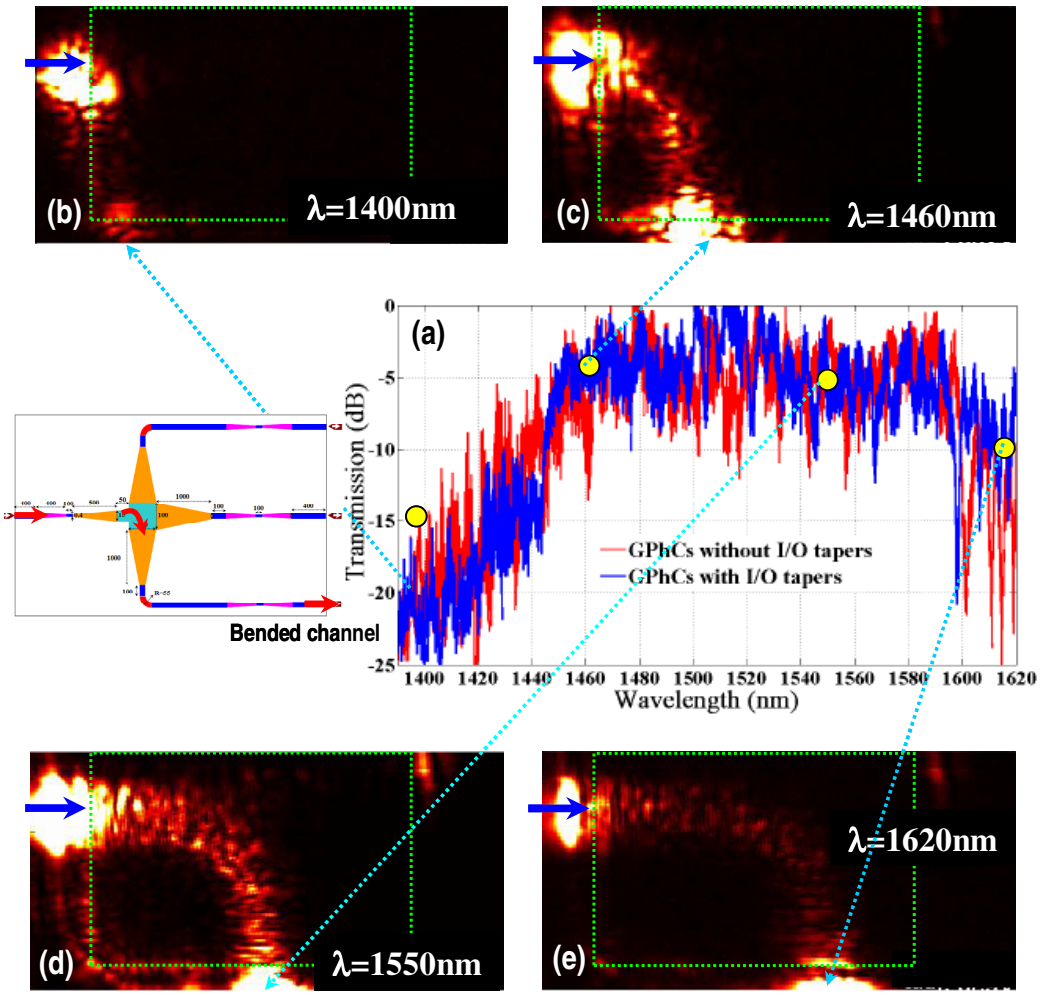

Figure 4.11: (a) Experimental transmission spectra of fabricated GPhC samples without input/output tapers (red line) and with input/output tapers (blue line), respectively, obtained by using the optical bench for far field measurement.

(b), (c), (d) and (e) SNOM image showing the electromagnetic intensity map obtained for TE polarized light at wavelength λ=1400nm, 1460nm, 1550nm and 1620nm, respectively.

If compared with the theoretical transmission curves (Fig. 3.7(b) in chapter 3), we can see that the experimental bandwidth (from 1460nm to 1620nm) is smaller, and that light bending occurs at slightly shorter wavelengths. This wavelength shift and spectrum small compression can be understood by the fact that 2D simulation was performed with the effective index approximation. Experimental transmission curves show that light starts to be bended in the fabricated GPhC device roughly at the

wavelength λ=1460nm. Four SNOM images in Fig. 4.12 (b) to (d) observed at different considered wavelengths (indicated on the experimental transmission curve) showing the electromagnetic intensity map of TE polarized light inside the GPhC area provide the direct evidence for the optical mirage and superbending effect in our fabricated GPhC samples. At λ=1400nm, we see that almost no light can enter the GPhC area (the green frame), since at this wavelength light is in the photonic bandgap between band 1 and band 2 of the photonic crystal lattice at the input point of the GPhC area. Starting from the wavelength λ=1460nm, TE light can enter into and begins to be bended inside GPhC area. It is visible that the intensity as well as the light path shape at each considered wavelength are different. The sensitivity of light trajectories inside our fabricated GPhC area will be considered in more detail in the next section, which is devoted to the dispersive properties of the considered GPhC configuration.

4.3.2. Dispersion properties of the GPhC configuration

After the transmission estimation by far field measurement, the study on light propagation and dispersion behavior inside fabricated GPhC samples were performed for TE polarized light by SNOM measurement. For this, a hyperspectral matrix of electromagnetic field was recorded over the total spectral range (1200nm-1650nm) with a spectral resolution of 1nm, with a 290nm spatial resolution in *x* and *y* directions over a 45µmx90µm image. This hyperspectral matrix enabled to emphasize the spatial and the spectral properties of the fabricated GPhC area by choosing a representation of it at a selected position or a selected wavelength, respectively.

4.3.2.1. Dispersion properties of the considered GPhC configuration

Fig. 4.13(a) presents the hyperspectral SNOM image obtained by mimicking the classical representation of light dispersion through a glass prism [24], then plotting on a single "white" image by using a color-coded scale over the spectral range of 1400nm-1650nm where the mirage effect takes place. It thus shows the behavior of light propagating inside the fabricated GPhC area simultaneously for different wavelengths in this spectral range, whereas figs. 4.12 (b), (c), (d) and (e), obtained separately at four selected wavelength 1460nm, 1500nm, 1555nm and 1610nm, respectively, provide an experimental visualization of light propagation inside the GPhC sample and the dispersion property of the proposed GPhC configuration.

The extraction from the obtained hyperspectral matrix shows that for wavelengths shorter than 1400nm, TE polarized light cannot penetrate into the PhC area but is reflected at the GPhC interface since it is in the TE photonic bandgap (between the first and the second bands) of the photonic crystal lattice at the input point of the configuration. Then, the mirage effect takes place for longer wavelengths than 1400nm, and remarkably in the 1460nm-1650nm range. In this range, the chromatic dispersion of this effect is clearly evidenced by the progressive penetration of the light beam within the fabricated GPhC area and the displacement of its curvature while increasing the wavelength (from position X_1 to X_4 for λ=1460nm to

λ=1650nm, respectively). Another feature that is clearly visible here is the absence of spatial beam spreading over a main part of the spectrum. This directly proves that light beam is nearly-collimated all along the curved trajectories.

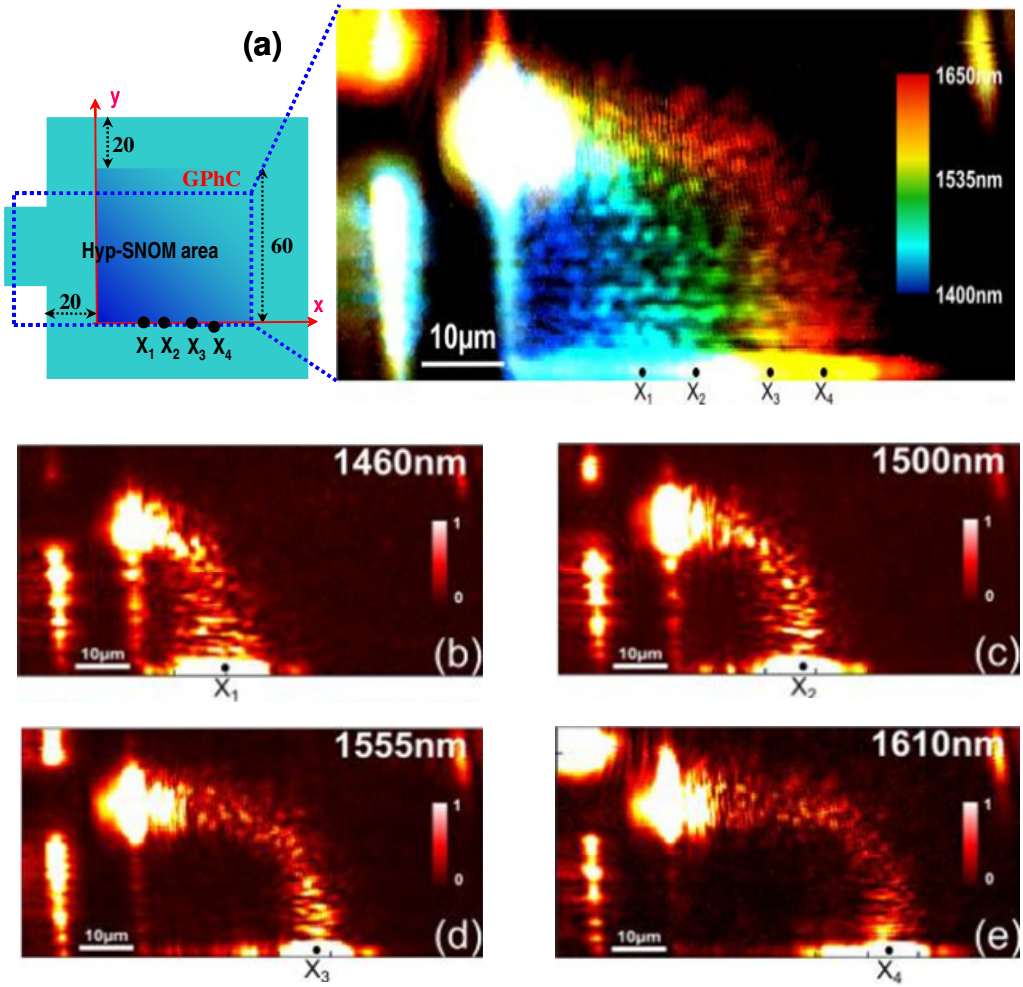

Figure 4.13: (a) Hyperspectral SNOM images providing the visualization of the dispersive behavior of the fabricated GPhC structure, (b), (c), (d), and (e) SNOM images showing EM intensity maps obtained for TE polarized light at wavelength λ=1460nm, 1500nm, 1555nm, and 1610nm, respectively.

From the figure, we can see the displacement of the light beam at the output of the GPhC area for the different wavelengths. To quantitatively estimate this dispersion property, we directly resorted to the analysis of the hyperspectral matrix not only for only four points as indicated in Fig. 4.13 but all along the output interface of the GPhC area (namely along the *x*-axis in the figures). Four snapshots of the spectra at different positions corresponding to the X_1 to X_4 point in Fig. 4.13(a) are plotted in Figs. 4.13 (b), (c), (d) and (e). Each spectrum was then fitted by a Gaussian function to estimate its central wavelength as well as its spectral full width at half maximum (FWHM). Repeating this protocol all along the *x*-axis permitted to extract the dispersion relationships which are plotted in Figs. 4.14(b) and (c).

Fig4.14 (b) and (c) show the light beam position along the output interface of the fabricated GPhC area with respect to the excitation wavelength. For each position,

the spectral (Fig.4.14(b)) and spatial (Fig.4.14(c)) FWHMs of the light beam are superimposed by horizontal and vertical segments, respectively. From this analysis, it is found that the output beam shifts almost linearly with a slope of 0.25µm/nm in the 1470-1600nm spectral range without noticeable spatial or spectral spreading (blue square points presented in the two figures). This dispersion value is comparable to that one achievable thanks to the PhC superprism effect [35] over almost the same propagation length, about 0.4µm/nm, but the strong beam spreading inherent to the superprism effect appears here drastically reduced.

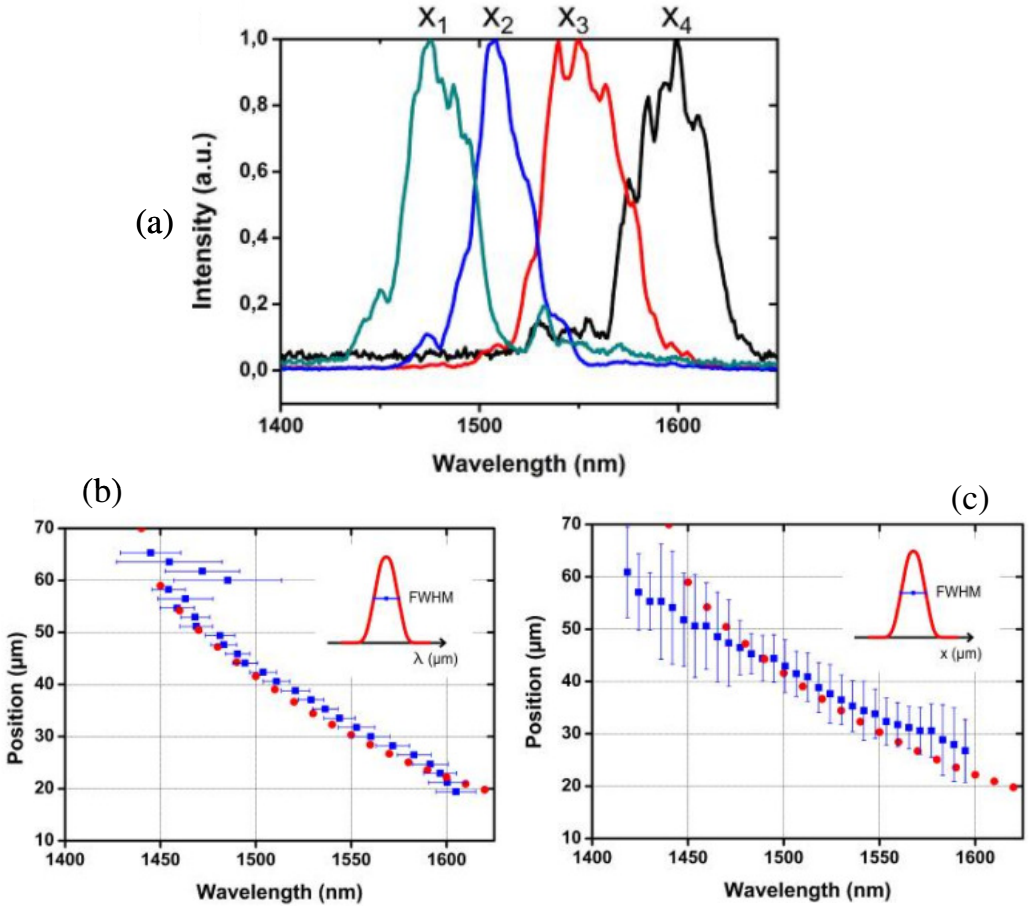

Figure 4.14: Quantitative estimation of the wavelength dispersion properties of the fabricated GPhC structures using Hyp-SNOM measurements: a) Spectral profiles recorded at the different coordinates depicted in Figs. 4.13(b) to (e). Position of the centre of the output optical beam along the x-axis as a function of light wavelength: filled blue squares corresponds to Hyp-SNOM measurements (b) with horizontal segments showing the beam FWHM spectral size, (c) with vertical segments showing the beam FWHM spatial size.

In the two last sub-figures, the red circles correspond to ray beam propagation results using Hamiltonian Optics calculations and based on the GPhC local bandstructure extracted using 3D-PWE calculations

These experimental results were also compared to the numerical predictions presented in chapter 3 (red circle points in the two figures Figs. 4.14(b) and (c). A quantitative agreement between Hyp-SNOM experimental results and 3D-PWE-assisted Hamiltonian Optics (HO) ray beam propagation was clearly obtained. This whole consistency shows that near-field measurements can successfully probe electromagnetic phenomena in artificial optical materials made of GPhCs. It also

experimentally proves that modeling the light propagation using the local bandstructure in the approximation of a slow variation of opto-geometrical parameters inherent to the HO formalism (presented in chapter 3 of this thesis) is valid here. In addition, these results also experimentally show that non-homogenizable GPhCs can be used to reconfigure the light path by changing the light wavelength. Optical beams operating at different wavelengths see different local parameters of the PhC lattice like the hole radius, and do not see the same photonic crystal bandstructure all along the propagation as predicted in [36].

4.3.2.1. Wavelength demultiplexing devices based on the considered GPhC configuration

Continuing the characterization steps of the dispersion properties of the fabricated samples, we here present some experimental results on the possibility to use this configuration as basic demultiplexing devices.

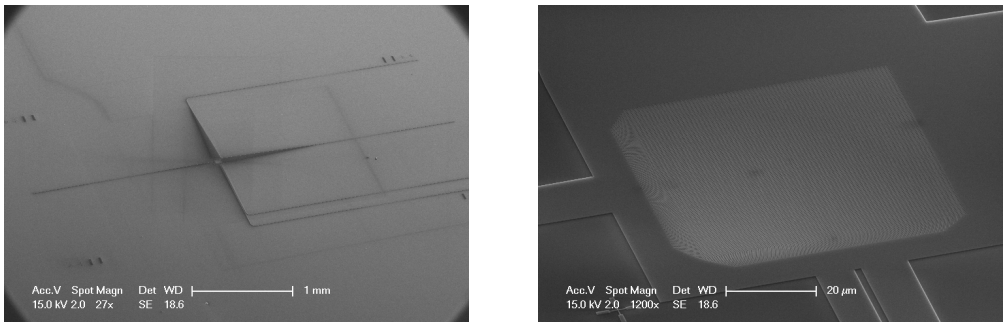

Figure 4.15: SEM images of a fabricated GPhC sample for wavelength demultiplexing purpose: (a) Overall view of the two-channel demultiplexing device, and (b) A zoomed view of this device.

Fig. 4.15(a) and (b) are SEM images of the GPhC sample fabricated for the purpose of two-channel demultiplexing. For this, the output waveguide to collect the overall transmission power at GPhC output was replaced by two output waveguides placed at the proper estimated positions obtained from the numerical calculation of the structure dispersion properties presented in chapter 3.

The fabricated sample was then measured by the use of the optical bench in *MINAPHOT* group. To do this, the optical source with a 1390nm-1620nm spectral range was still employed.

Figs. 4.16(a),(b), and (c) show the experimental optical transmission powers of three different fabricated GPhC samples (which were designed to present two wavelength demultiplexing channel around λ = 1550nm) in comparison with the numerical results obtained by 2D-FDTD simulation. In these figures, dashed lines stand for simulation transmission and rippled lines represent experimental results (reminding that related experimental transmission spectra have been normalized by the transmission power spectrum of a sample without the GPhC but having the same photonic circuit to input and collect the light).

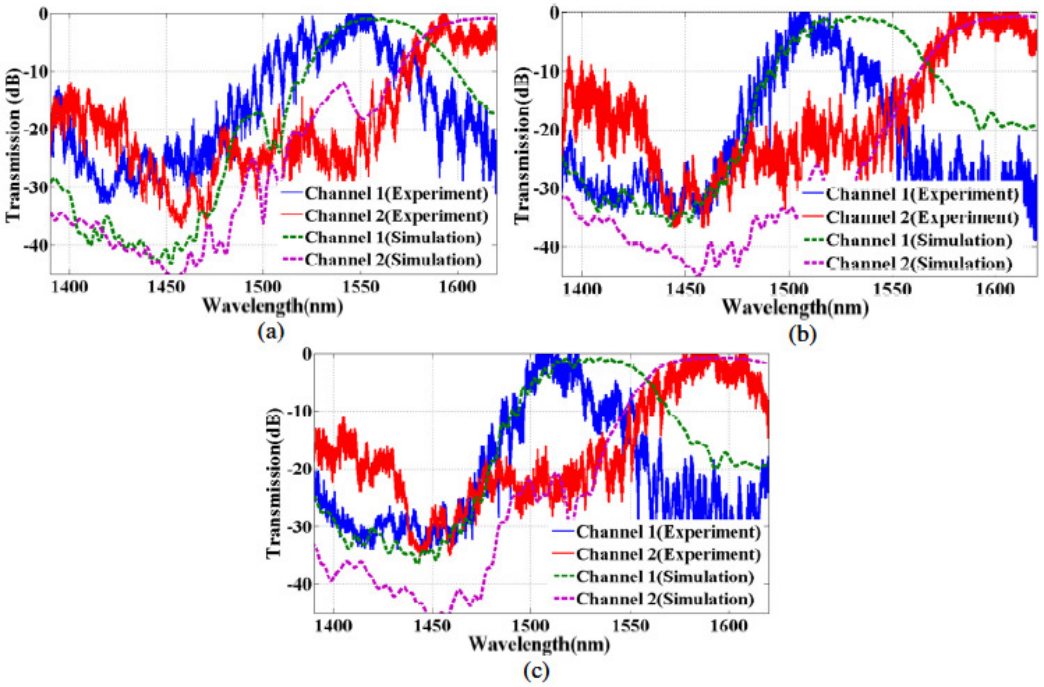

Figure 4.16: Operation of three fabricated GPhC-based two-channel demultiplexing devices (a) channel 1: λ_1 = 1552nm and channel 2: λ_2 = 1616nm; (b) channel 1: λ_1 = 1510nm and channel 2: λ_2 = 1600nm; and (c) channel 1: λ_1 = 1510nm and channel 2: λ_2 = 1590nm.

Results show a correct agreement between experiments and simulation with a wavelength blue-shift just like already pointed out in 4.3.2 and due to the 2D feature of the performed FDTD simulations.

As can be seen from the results, two centered wavelength channels of each demultiplexer are well separated and then collected at two outputs with low loss (<2dB) and low crosstalk (less than −20dB) levels.

4.3.3. Polarization-dependency of the GPhC configuration

As theoretically presented and studied in section 3.3 of chapter 3, the proposed GPhC configuration is sensitive to light polarization and it is predicted that the configuration can be used for a polarization beam splitting purpose. To experimentally prove this prediction, the fabricated GPhC samples were characterized using the experimental SNOM setup.

Light paths for TE and TM polarized beams inside the fabricated GPhC sample were directly visualized by using a Scanning Near-field Optical Microscope operating in collection mode. The experimental SNOM images recorded at λ=1550nm for the two polarization are presented in Figs. 4.17(a) and 4.17(b). As predicted earlier, the TE-beam is bended inside the GPhC while the TM-beam goes straight. Since the near-field probe is selectively sensitive to the components of the electric field transverse to the probe axis, the TM-beam (major E-field parallel to the probe axis) is measured experimentally with a significantly lower signal to noise ratio compared to the TE-

beam. This does not prevent from the qualitative demonstration of the polarization splitting effect but this implies that attempts to quantitatively compare the data recorded for the TE and TM beams are hazardous.

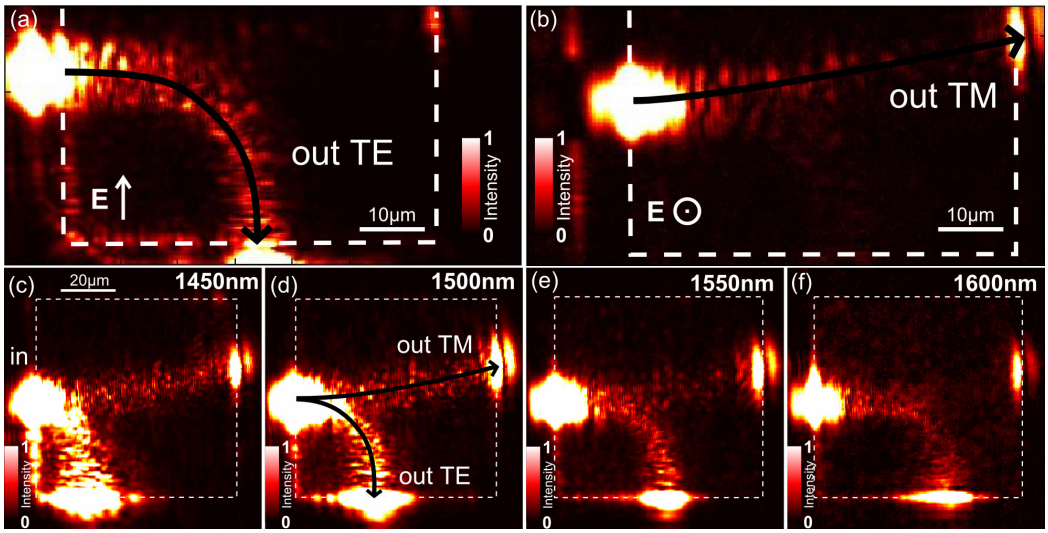

Figure 4.17: (a) SNOM image obtained at λ=1550nm for a TE polarized light at the input. (b) SNOM image obtained at λ=1550nm for a TM polarized light at the input, (c) to (f) Hyp-SNOM images obtained at λ=1450nm, 1500nm, 1550nm, and 1600nm, with a non-polarized light source. The beam splits into a TE and a TM polarized beams. Over a broadband of 150nm, TE-beam is bended while TM-beam goes straight.

To provide a direct evidence of the beam splitting effect over the spectrum, an unpolarized supercontinuum laser source was injected into the GPhC and the light spectrum was collected by the probe on each pixel. The SNOM snapshots of the hyperspectral measurement at λ=1450nm, 1500nm, 1550nm, and 1600nm, respectively, are plotted in Fig. 4.17(c) to (f). As can be seen, the predicted beam splitting effect is evidenced over the full 150nm spectral range, while, due to the probe collection efficiency, the TE-beam is more intense than the TM-beam. We also note that the TM-beam remains almost unchanged over the spectrum while the TE-beam bending depends on the wavelength resulting in a variation of its output position. One could take benefit from this feature to combine the beam splitting effect with a wavelength division demultiplexing. Otherwise, an inverted tapered waveguide could be used to collect the TE-beam and cancel this dispersive effect.

4.3.4. Transition between homogenizable regime and PhC regime

As discussed earlier in chapter 1 and chapter 2, light propagation in photonic crystal structures can be classified into two regimes: the long-wavelength regime (**LWR** or homogenization regime) and the short-wavelength regime (**SWR** or dispersive regime). The terminology of short-wavelength regime refers to a frequency range close to the photonic bandgap where the optical fields are strongly influenced by the interference pattern between forward and backward waves. Given the classical Bragg relationship, this condition corresponds to a normalized frequency ω, defined as the ratio of the lattice parameter a and the vacuum wavelength λ, given by

ω_B=1/2n, with n the optical effective index to be considered. With values of n in the range 1.7-3 for most of planar two-dimensional (2D) PhCs fabricated within semiconductor technologies, ω_B is typically comprised between 0.2 and 0.3 and is frequently around 0.25. In this regime, numerous interesting phenomena have been reported over the years like photonic bandgap effects leading to photon confinement in nanoscale optical cavities [37] and "slow light" effects [38], or unusual dispersive phenomena in allowed dispersion bands like the negative refraction, superprism, self-collimation or superlensing phenomena [39, 40].

The other region which is well below the photonic bandgap ($\omega << \omega_B$), is called the *long-wavelength regime* (LWR) or the homogenization regime. A large number of works devoted to the theory of homogenization of periodic and composite materials was published [41-44]. Basically, in this regime the wavelength being much larger than the lattice period, light then "feels" a homogeneous-like medium. In the most general case, 2D PhCs then behave as anisotropic biaxial optical media, which can give rise to interesting physical properties like unusually large in-plane anisotropy in comparison with natural crystals [45].

Using a rotationally symmetric lattice cell unit, defined by both the Bravais lattice and the geometry of the inclusions, PhCs with long-wavelength in-plane isotropic behaviours can be defined, then reducing the homogenized index tensor to a single scalar value. This index can be evaluated by considering for $\omega \to 0$ the square root of the PhC dispersion curve slope. It is known that TE and TM modes have different slopes [44]. Whereas, the effective long-range index for TE-modes does not have an analytic expression, it is given by the following relationship for TM-modes [44, 45]:

$$n_{long-range} = \sqrt{f \times n_{hole}{}^2 + (1-f) \times n_{diel}{}^2} \qquad (4.1)$$

, with f the PhC filling factor, and n_{hole} and n_{diel} the indices of the hole and surrounding dielectric media, respectively.

Such a homogenized index approach has recently received a strong attention for the implementation at optical frequencies of concepts inherited from the field of metametarials designed using the formalism of spatial coordinate transforms. It was for example applied to the practical realization of electromagnetic invisibility devices or Luneburg lensing structures [17, 46].

The two *long and short wavelength regimes* have been separately explored, yet the gap between them has not received much attention. Starting from this point and motivated by the previous obtained results, we try investigating the study on the transition between these two regimes in the GPhC fabricated structures. Due to experimental (available reachable wavelength range) and theoretical reasons (more convenient homogenization of periodic media in TM polarization), attention was concentrated on the TM polarization of light.

EFS of band 1 in TM polarization of infinitely periodic PhC square lattices made of air holes with filling factors of r/a=0.2, r/a=0.275, and r/a=0.35, respectively, are shown in Fig. 4.18 (all over opto-geometrical parameters are the same as in previous chapters and sections). In the three cases, the transition between the LWR and the SWR is visible by the progressive deformation of the EFS from positively curved circular shapes centered on Γ to square shapes centered on the M points close to the Brillouin area and having thus a negative curvature with respect to

Γ. Yet, the limit between the two regimes shifts with the considered *r/a* value, meaning that, at one given frequency, light propagation within the GPhC may (LWR propagation) or may not (SWR propagation) follow a classical behaviour in the sense of homogenized media. Any abrupt change of the light beam direction within the GPhC is thus likely to be the signature of the transition between the LWR and SWR. This principle is the basis of the experimental method that was applied to investigate the transition between the two regimes.

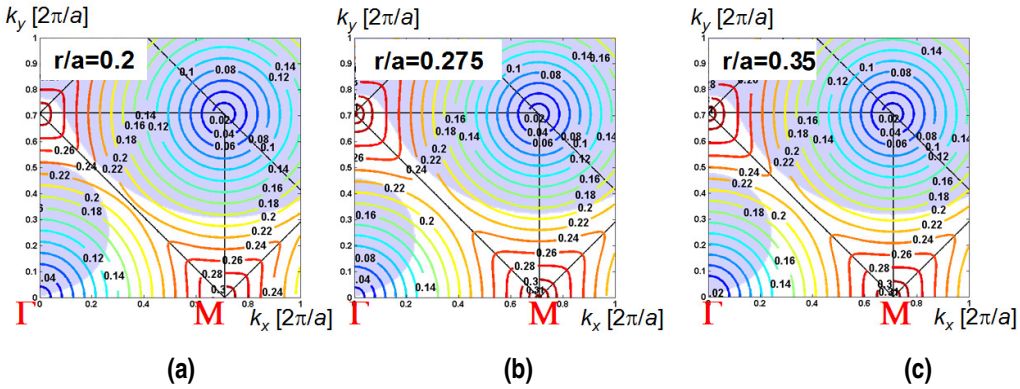

Figure 4.18: Equi-Frequency Surfaces in TM light polarization of a 2D square photonic crystal of lattice period a and cylindrical air holes (n=1) of normalized radius *r/a* etched in a surrounding optical medium of 2.26 index: (a) *r/a*=0.2, (b) *r/a*=0.275, (c) *r/a*=0.35

The fabricated GPhC sample (presented in Fig. 4.10(a)) was characterized by employing the Hyp-SNOM experimental setup which allowed us to tune light wavelength from λ=1650nm (ω=0.230) to 1300nm (ω=0.292) in order to explore the normalized frequency range of interest (0.23-0.29) and monitor the related spatial and spectral properties of the GPhC. Figure 4.18 shows the SNOM image measured at ω=0.2675 (λ=1420nm), which is characteristic of the observed phenomena, at least from λ=1350nm to 1440nm (0.264≤ω≤0.281).

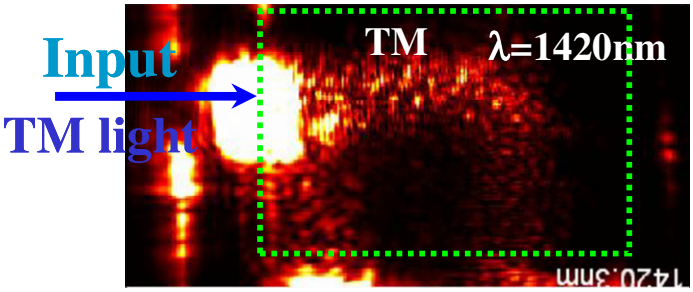

Figure 4.19: Optical near-field image of the light optical intensity propagation through the structure in TM polarization at λ=1420nm (ω=a/λ≈0.2675 given a≈390nm)

As seen in Fig. 4.19, light propagation is first characterized by a slightly upward bended path towards the region of smaller air hole radii (higher long range index), whereas the last part of the light trajectory is directed downward towards the region of larger air holes (lower long range index). Moreover, the transition between these two behaviors is interestingly fairly abrupt and occurs at a specific location (x_{th},y_{th}) within the GPhC area that can be easily estimated from the SNOM image. The beginning upward bending of the light path can be easily related to conventional

mirage effect in the LWR regime, in exact analogy with the atmospheric mirage effect where light trajectory is bended towards high index regions of graded index media. The monitored abrupt downward bending effect is thus the signature of a non-conventional mirage effect meaning that light propagation has then entered the SWR at the threshold position (x_{th},y_{th}). Qualitatively, it is understandable that λ/n_{long_range} decreases along the first part of the light path, as the long range index first progressively increases, and that below a given "λ/n" value, the approximation of homogenization fails.

By exploiting the images collected for different frequencies other than ω=0.2675 and repeating the estimation of (x_{th},y_{th}) in the full frequency range under investigation, we extracted the local PhC filling factor for each (x_{th},y_{th}) threshold point, and then estimated the local long range index using equation (4.1) as a function of light wavelength using n_{diel}=2.26.

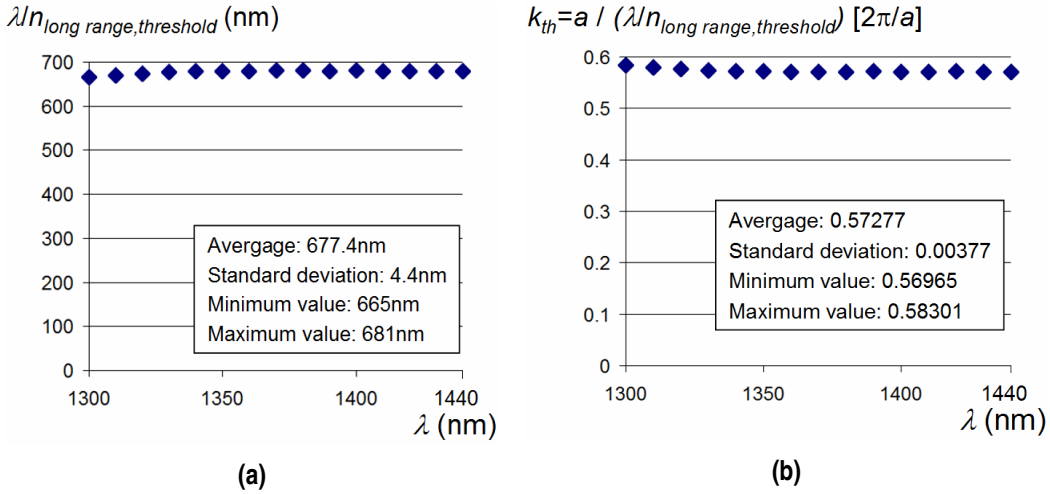

Figure 4.20: Experimental investigation of the criterion characterizing the transition between the long-wavelength and short-wavelength regimes of light propagation within the graded photonic crystal area: (a) Evolution of "λ/n" using a homogenized PhC index at the threshold position between the conventional the conventional and unconventional mirage effects typically shown in Figure 4.18b, and (b) Reformulation of the experimentally estimated "λ/n" quantity in term of normalized wavevector amplitude (2π/a units) following the classical notation of PhCs.

The related experimental ratio $\lambda/(n_{long\_range})$ threshold, which describes the transition between the LWR and the SWR, is reported in Figure 4.20(a). In the 1300nm-1490nm wavelength range, $\lambda/(n_{long\_range})$ threshold is estimated to 677.4nm, i.e. only 1.78 times the lattice period a, with a standard deviation as low as 4.4nm. This "invariant" quantity can be converted into wavevector modulus as the dispersion relationship "$k=n.2\pi/\lambda$" holds for each wavelength up to the threshold point with $n=n_{long\text{-}range}$. Doing this and rescaling the wavector into $2\pi/a$ normalized units to match with the conventional PhC notation, the threshold wavevector amplitude $k_{threshold}$ depicted in Figure 4.20(b) is obtained. The obtained average value is 0.573 [$2\pi/a$] (with a standard deviation of 0.0038), which can be superimposed on the EFS in reciprocal wavevector space. As shown in Fig. 4.18, the experimental LWR/SWR threshold condition seems to correspond to the region in k-space where a change of the EFS curvature sign occurs with respect to Γ.

In order to analyze these experimental data and understand the modification of the light propagation direction, we came back to the theoretical condition for the possible homogenization of PhCs. As shown in previous works, Bloch waves in PhCs can be decomposed in an infinite series of plane waves in the form [47]:

$$\boldsymbol{H}(\boldsymbol{r}) = exp(i\boldsymbol{k}.\boldsymbol{r})\sum_{\boldsymbol{G}} h_k(\boldsymbol{G})\boldsymbol{H}_0\, exp(i\boldsymbol{G}.\boldsymbol{r}) \qquad (4.2)$$

In this equation, $\boldsymbol{H_0}$ is the field amplitude, $\boldsymbol{k}$ is the wavevector, $h_G(\boldsymbol{k})$ are the dimensionless Fourier coefficients of the Bloch field periodic part. The contribution rates $\eta_G(\boldsymbol{k})$ to the global Bloch wave energy of each plane wave at point $\boldsymbol{k}$ characterized by a $\boldsymbol{G}$ shift with respect to the Γ is obtained ($0<\eta_G<100\%$) as [47]:

$$\eta_G(\boldsymbol{k}) = \left|h_k(\boldsymbol{G})\right|^2 \qquad (4.3)$$

As mentioned in Ref. [44], the long-wavelength limit of PhC can be understood as the situation when the Fourier expansion of the field of Eq. (4.2) reduces to only one plane wave due to a condition of the form $h_k(\boldsymbol{G}\neq 0) << h_k(\boldsymbol{G}=0)$ when $\omega \rightarrow 0$. To go beyond this qualitative statement, we calculated the contribution rates $\eta_{j,\ 0\leq j\leq 4}$ of the first five dominant plane waves along the ΓM segment in reciprocal space where the previously reported change of the EFS curvature sign occurs. For this, the PhC eigenvalue/eigenvector Hemholtz equation was solved for an infinitely periodic square PhC characterized by a given value of *r/a* using a $\boldsymbol{H}$ formulation of the Helmoltz master equation using a truncated plane wave basis with 289 components. Using the wavelength/wavevector relationship in band 1 along the ΓM segment, we then estimated the contribution rates $\eta_{j,\ 0\leq j\leq 4}$ as a function of ω.

Fig. 4.21 shows the obtained result for *r/a=0.31*, corresponding to the air hole normalized radius close to the injection point within the GPhC area, i.e. in a situation of strong index corrugation in which the PhC homogenization hypothesis is more challenging than for smaller air hole filling factors.

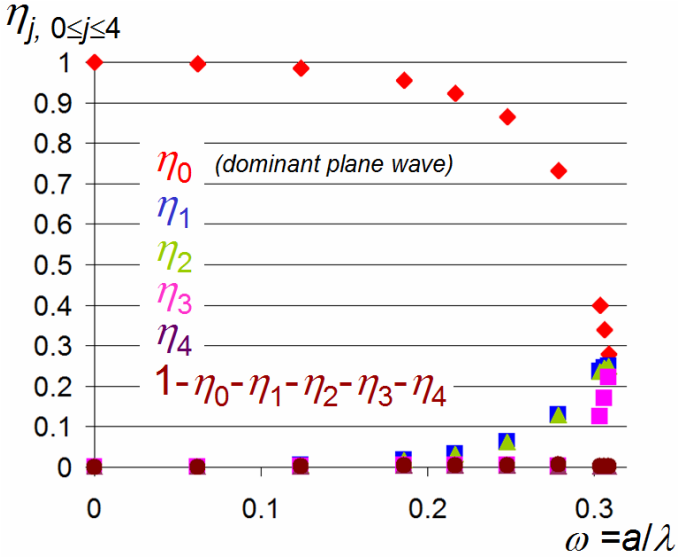

Figure 4.21: Theoretical investigation of the relative contribution rates ($0\leq\eta_j\leq 1$) of the five dominant partial waves ($0\leq j\leq 4$) of the PhC Bloch modes excited for wavevectors ranging in the Γ-M in the reciprocal space of the considered square lattice PhC (see Figure 4.17)

To guide the eye, a vertical line is added at ω=0.275, corresponding the frequency of beam collimation between the two situations of EFS with opposite curvature signs with respect to Γ. For $\omega \to 0$, the principal plane wave characterized by $\boldsymbol{G}$=0 clearly carries most of the Bloch wave energy, but its contribution is still above 70% up to ω=0.275 and then suddenly drops due to the influence of the photonic bandedge. This result suggests that the inversion of the EFS curvature can be interpreted as a sharp decrease of the main plane ($\boldsymbol{G}$=0) contribution in the Bloch wave decomposition. In the same time, this analysis provided by following the wavevector along the ΓM segment does not directly take into account the possible exit of the primary wavevector path out of the first Brillouin area.

Considering the closed shapes of the EFS around the M points for ω>0.25, let us here consider for this a excitation $\boldsymbol{k}$ point given by $\boldsymbol{k}$=0.45$\boldsymbol{b_1}$+0.55$\boldsymbol{b_2}$, with $\boldsymbol{b_1}$,$\boldsymbol{b_2}$ the two PhC primary vectors in reciprocal space. Due to the translational shift of any $\boldsymbol{k}$ points by $\mathbf{G}=l_1\boldsymbol{b_1}+l_2\boldsymbol{b_2}$, with l_1,l_2 two integers, contributions to the Bloch wave energy can arise, as previously, from components located in all Brillouin zones. The minimum number of "dominant" plane waves is then only three, but four ones are considered here to include the contributions from around the four M points.

Figure 4.22 shows the obtained situation in reciprocal space, with the contribution rates in % of the four dominant plane waves, as well as arrows having sizes related to their phase velocities defined as $\boldsymbol{v_{phase}}(l_1,l_2)=(\omega/|l_1\boldsymbol{b_1}+l_2\boldsymbol{b_2}|^2).(l_1\boldsymbol{b_1}+l_2\boldsymbol{b_2})$, the Bloch wave group velocity being then given as a whole by $\boldsymbol{v_{group}}(\boldsymbol{k})=\sum|h_{\boldsymbol{k}}(l_1\boldsymbol{b_1}+l_2\boldsymbol{b_2})|^2.\boldsymbol{v_{phase}}(l_1,l_2)$ [47].

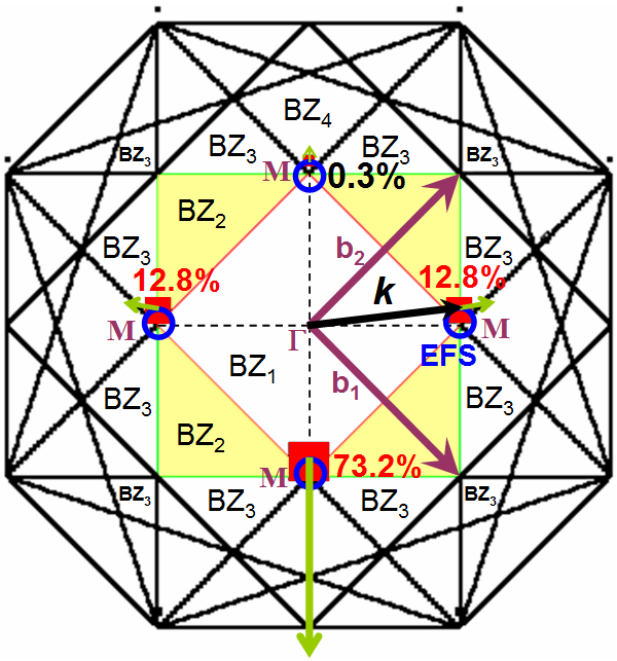

Figure 4.22: Analysis of the physical origin of the "λ/n" invariant experimentally evidenced in Fig. 4.20 by the decomposition of the PhC Bloch wave characterized by a wavevector slightly lying out of the first Brillouin area on a closed round EFS centred on the M points (as shown in Figure 4.17 for ω>0.25) and given by k=0.45$\boldsymbol{b_1}$+0.55$\boldsymbol{b_2}$ with $\boldsymbol{b_1}$,$\boldsymbol{b_2}$ the two PhC primary vectors in reciprocal space. Indications about the contribution rates of the main four plane waves as well as well as about their individual phase velocities are also given.

The main partial contribution to the Bloch wave now corresponds to $h_k(\boldsymbol{G}=-\boldsymbol{b_2})$ and not $h_k(\boldsymbol{G}=\boldsymbol{0})$. As it carries more than 73% of the Bloch wave energy, its downward phase velocity is dominating the group velocity expansion as a sum of weighted phase velocities. This result means that the transition between the LWR and SWR is not necessarily accompanied by a strong power transfer from the dominant partial plane wave to the others provided that the operating wavevector does not approach the M points too closely. In the situation considered here, $|\boldsymbol{k}-\boldsymbol{k_M}|$ is already as low as $0.05|\boldsymbol{b_2}-\boldsymbol{b_1}|=0.05\sqrt{2}\approx 0.071$ $[2\pi/a]$.

Considering this, an interpretation of the transition between the LWR and SWR light propagation in the studied GPhC configuration can be proposed by considering the wavevector path in reciprocal space corresponding to the light beam trajectory depicted in Fig. 4.18. Fig. 4.22 shows a schematic representation of the related EFS deformation and successively obtained group velocities. Homogenization of the PhC medium can be considered as a valid approach up or close to the crossing between the primary wavevector path and the first Brillouin area limit. At this position, the first plane wave strength is maintained but a sudden shift of wavevector occurs to maintain the dominant plane wave in the first Brillouin area, corresponding to a change of the form $h_k(\boldsymbol{G}=0)>>h_k(\boldsymbol{G}\neq 0)$ => $h_k(\boldsymbol{G}=-\boldsymbol{b_2})>>h_k(\boldsymbol{G}\neq-\boldsymbol{b_2})$. The experimentally evidenced invariant quantity characterizing the transition between the LWR and SWR can be attributed to the nearly independent wavevector path for wavelengths in the range of interest, thus inducing a nearly constant threshold wavevector amplitude k_{th} around 0.573.

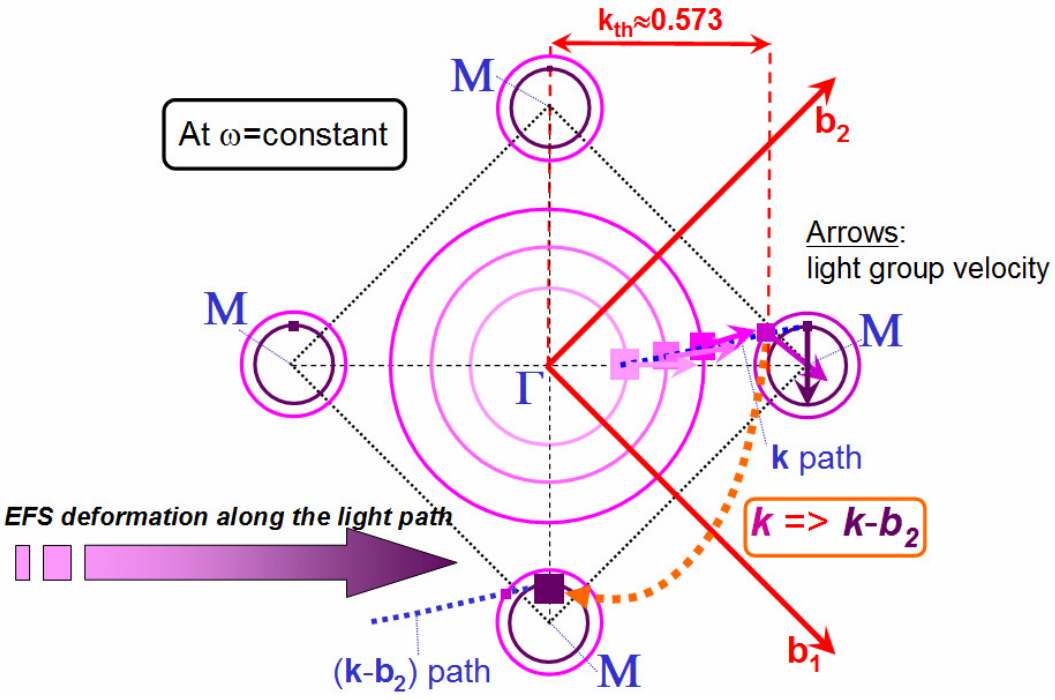

Figure 4.23: Schematic picture of the wavevector path, EFS deformations, and excited light group velocities corresponding to the transition between the LWR and SWR of light propagation observed in the GPhC studied structure using Hyp-SNOM measurements.

4.4. Conclusion

The fabrication of GPhC samples has been presented in this chapter. E-beam lithography with correction of proximity effects of the exposure dose has been successfully employed in the employed fabrication process. Various samples have been designed and fabricated in order to evaluate the transmission efficiency and investigate the demultiplexing performances of the studied GPhC configuration. SEM images of GPhC samples have proved that our technical parameters are reasonable to well define the GPhC structures in the range of this thesis.

Results on experimental investigation of fabricated GPhC samples have been also presented by using two measurement methods: near-field and far-field measurements. Results obtained from these two methods have proved the presence of the mirage effect at optical wavelengths.

The considered GPhC configuration was presented to be sensitive to the wavelength tuning. Its dispersive coefficient around 0.25µm/nm allows the possibility of utilizing this configuration for wavelength demultiplexer devices with relatively low loss and low level of crosstalk between demultiplexing channels.

The polarization properties as well as the transition from the homogenizable regime to the diffraction regime presented through experimental results will be interesting for the realization of high efficient polarization beam splitters and the realization of GPhC devices that can work in both homogenizable and non-homogenizable regimes.

Conclusion and Perspectives

The works presented in this thesis manuscript have been motivated by the possible exploitation of electromagnetic artificial materials at optical frequencies to shape optical beams and propose optical functionalities such as wavelength-sensitive or polarization-sensitive structures. They rely on the use of graded photonic crystals (GPhCs) made of a two-dimensional variation of opto-geometrical parameters of a planar photonic crystal lattice.

Due to the large number of degrees of freedom to define GPhCs structures by modulating the lattice parameters (filling factor, basic vector orientation, aspect ratio between two basic vectors or a combination those variation) and to the wish that we had to try fabricating and experimentally characterizing practical structures, the choice was made to focus most of efforts on a first simple configuration. A fairly general modeling methodology based on the description of the propagation of light from the local photonic band structure using a ray tracing approach was developed but essentially applied to the chosen "reference structure" made of a planar air hole graded photonic crystal of square lattice with a variable filling factor and operating in the first photonic band. The related methodology was presented in chapter 2, which also showed a good agreement of this approach with numerical simulations made using Finite Difference Time Domain (FDTD) calculations.

The optical properties of the considered GPhC structures have been then studied in chapter 3. A particular Gaussian-like air hole filling factor was chosen to enable a 90°-like light bending with low insertion loss due to the use of input/output tapers between the periodically corrugated area and surrounding slab regions. The structure dispersion properties, namely the light beam deflection in °/nm or µm/nm was numerically estimated, as well as its properties with respect to the TE/TM light polarization.

Experimental results about the fabrication techniques, the methods of optical characterization, and the optical structure properties have been presented in chapter 4. The employed fabrication process using Electron Beam Lithography (EBL) with a careful correction of proximity effects proved to bring a reasonable approach for the correct fabrication of silicon on insulator (SOI) GPhC structures. The far-field experiments carried out in the near infra-red around λ=1.5µm led to the demonstration of the predicted light bending effect and provided the practical level of the structure insertion losses below 2dB. The exploitation of the scanning near-field optical microscope (SNOM) images obtained by the research group of Frédérique De Fornel

in Dijon also allowed the experimental visualization of the predicted electromagnetic phenomena and brought interesting results about the dispersion and polarization properties of the GPhC samples. A quantitative agreement was obtained between the monitored structure wavelength dispersion and the achieved ray tracing propagation modeling exploiting three-dimensional Plane Wave Expansion calculations for the extraction of the local photonic bandstructure. This overall consistency was a satisfying point, both in regards to the ability of the SNOM hyperspectral developed setup to characterize optical artificial optical materials and to the employed modeling methodology and fabrication process. Additionally, the performed measurements provided a nearly-linear beam deflection of 40µm in a 150nm optical bandwidth for a 60µm square photonic crystal structure, i.e. close to what is usually obtained with photonic crystal superprisms but without noticeable spectral and spatial beam spreadings.

The TE/TM beam splitting effect was also clearly observed using the employed near-field setup. The quantitative measurements from this approach of the polarization crosstalk was not possible due to the difference between the SNOM probe sensitivities in TE and TM polarizations, respectively, but the predicted bandwidth around 160nm was experimentally confirmed. Last, the performed experiments in a broad wavelength range allowed experimentally investigating the transition between the homogeneous and diffraction regimes of light propagation in GPhCs. The study of the SNOM images collected from the wavelength of 1300nm and 1440nm in TM polarization led to the experimental observation of an invariant quantity characterization the transition between the two regimes quoted above and to the interpretation of the observed physical phenomenon in connection with the photonic crystal Equi-Frequency Surfaces in reciprocal space.

As a whole, the research presented in this manuscript is mostly restricted to a single graded photonic crystal configuration and has led to the experimental observation of the light bending effect predicted in previous works and to the investigation of the structure dispersion and polarization properties.

More complicated two-dimensional chirps of the photonic crystal parameters can be envisaged in forthcoming works as well as the exploitation of other frequency bands.

References

1. P. Yeh, "Electromagnetic propagation in birefringent layered media," J. Opt. Soc. Am. 69, 742-756 (1979).
2. L. Wu, M. Mazilu, T. Karle, and T. F. Krauss, "Superprism phenomena in planar photonic crystals," IEEE Journal of Quantum Electronics 38, 915-918 (2002).
3. T. Prasad, V. Colvin, and D. Mittleman, "Superprism phenomenon in three dimensional macroporous polymer photonic crystals," Phys. Rev. B 67, 165103 (2003).
4. C. Luo, M. Soljačić, and J. D. Joanopoulos, "Superprism effect based on phase velocities," Opt. Lett. 29, 745-747 (2004).
5. A. Lupu, E. Cassan, S. Laval, L. E. Melhaoui, P. Lyan, and J. Fedeli, "Experimental evidence for superprism phenomena in SOI photonic crystals," Opt. Express 12, 5690-5696 (2004).
6. Y. Jiao, S. Fan, and D. A. B. Miller, "Designing for beam propagation in periodic and nonperiodic photonic nanostructures: extended Hamiltonian method," Phys. Rev. E Stat. Nonlin. Soft Matter Phys. 70, 036612 (2004).
7. D. R. Smith, J. B. Pendry, and M. C. K. Wiltshire, "Metamaterials and negative refractive index," Science 305, 788–792 (2004).
8. N. Engheta, and R. W. Ziolkowski, "Metamaterials: Physics and Engineering Explorations," (John Wiley and Sons, 2006), pp. 211–221.
9. J. B. Pendry, D. Schurig, and D. R. Smith, "Controlling electromagnetic fields," Science 312, 1780–1782 (2006).
10. Z. Saïd, A. Sihvola, and A. P. Vinogradov, "Metamaterials and Plasmonics: Fundamentals, Modelling, Applications," (Springer-Verlag, 2008), p. 106.
11. A. V. Kildishev, and V. M. Shalaev, "Engineering space for light via transformation optics," Opt. Lett. 33, 43– 45 (2008).
12. M. Rahm, S. A. Cummer, D. Schurig, J. B. Pendry, and D. R. Smith, "Optical design of reflectionless complex media by finite embedded coordinate transformations," Phys. Rev. Lett. 100, 063903 (2008).
13. N. I. Landy, and W. J. Padilla, "Guiding light with conformal transformations," Opt. Express 17, 14872–14879 (2009).
14. Z. L. Mei, and T. J. Cui, "Arbitrary bending of electromagnetic waves using isotropic materials," J. Appl. Phys. 105, 104913 (2009).
15. W. Ding, D. Tang, Y. Liu, L. Chen, and X. Sun, "Arbitrary waveguide bends using isotropic and homogeneous metamaterial," Appl. Phys. Lett. 96, 041102 (2010).
16. L. H. Gabrielli, and M. Lipson, "Transformation optics on a silicon platform," J. Opt. 13, 024010 (2011).

17. L. H. Gabrielli, J. Cardenas, C. B. Poitras, and M. Lipson, "Silicon nanostructure cloak operating at optical frequencies," Nat. Photonics 3, 461–463 (2009).
18. J. Valentine, J. Li, T. Zentgraf, G. Bartal, and X. Zhang, "An optical cloak made of dielectrics," Nat. Mater. 8, 568–571 (2009).
19. P. S. J. Russel, and T. A. Birks, "Hamiltonian optics of nonuniform photonic crystals," J. Lightwave Technol. 17, 1982-1988 (1999).
20. E. Centeno, and D. Cassagne, "Graded photonic crystals," Opt. Lett. 30, 2278–2280 (2005).
21. E. Centeno, D. Cassagne, and J.-P. Albert, "Mirage and superbending effect in two-dimensional graded photonic crystals," Phys. Rev. B 73, 235119 (2006).
22. P. S. J. Russel, and T. A. Birks, eds. Block wave optics in photonic crystals: Physics and Application (Kluwer Academic Publishers, 1996).
23. E. Cassan, and K. V. Do, "Analytic design of graded photonic crystals in the metamaterial regime," J. Opt. Soc. Am. B 28, 1905-1910 (2011).
24. E. Akmansoy, E. Centeno, K. Vynck, D. Cassagne, and J. M. Lourtioz, "Graded photonic crystals curve the flow of light: An experimental demonstration by the mirage effect," Appl. Phys. Lett. 92, 133501 (2008).
25. S. G. Johnson, P. Bienstman, M. A. Skorobogatiy, M. Ibanescu, E. Lidorikis, and J. D. Joannopoulos, "Adiabatic theorem and continuous coupled-mode theory for efficient taper transitions in photonic crystals," Phys. Rev. E 66, 066608 (2002).
26. D. Bernier, E. Cassan, L. Roux, D. Marris-Morini, and L. Vivien, "Efficient band-edge light injection in two dimensional planarphotonic crystals using a gradual interface," Opt. Eng. Lett 48, 070501 (2009).
27. I. Kiyat, A. Aydinlin, and N. Dagli, "A compact Silicon-on-Insulator Polarization Splitter," Photonics Technology Letters 17, 100-102 (2005).
28. D. Dai, and J. E. Bowers, "Novel concept for ultracompact polarization splitter-rotator based on silicon nanowires," Opt. Expr. 19, 10940-10949 (2011).
29. T. Barwicz, M. R. Watts, M. A. Popovic, P. T. Rakich, L. Socci, F. X. Kartner, E. P. Ippen, and H. I. Smith, "Polarization-transparent microphotonic devices in the strong confinement limit," Nature Photonics 1, 57-60 (2007).
30. L. Wu, M. Mazilu, J.-F. Gallet, T. F. Krauss, A. Jugessur, and R. M. D. L. Rue, "Planar photonic crystal ploarization splitter," Opt. Lett. 29, 1620-1622 (2004).
31. X. Ao, L. Liu, L. Wosinski, and S. He, "Polarization beam splitter based on a two-dimensional photonic crystal of pillar type," Applied Physics Letters 89, 171115 (2006).
32. E. Schonbrun, Q. Wu, W. Park, T. Yamashita, and C. J. Summers, "Polarization beam splitter based on a photonic crystal heterostructure," Opt. Lett. 31, 3104-3106 (2006).

33. V. Zabelin, L. A. Dunbar, N. L. Thomas, R. Houdré, M. V. Kotlyar, L. O'Faolain, and T. F. Krauss, "Self-collimating photonic crystal polarization beam splitter," Opt. Lett. 32 530-532 (2007).
34. A. Martinez-Gil, "Nanostructuration de surfaces de silicium pour guider la croissance auto-organisée de nanostructures métalliques."
35. J. Dellinger, D. Bernier, B. Cluzel, X. L. Roux, A. Lupu, F. D. Fornel, and E. Cassan, "Near-field observation of beam steering in a photonic crystal superprism," Opt. Lett. 36, 1074-1076 (2011).
36. K. V. Do, X. L. Roux, C. Caer, D. Marris-Morini, N. Izard, L. Vivien, and E. Cassan, "Wavelength demultiplexer based on a two-dimensional graded photonic crystal" IEEE Photon. Technol. Lett. 23 1094–1096 (2011).
37. E. Kuramochi, M. Notomi, S. Mitsugi, A. Shinya, T. Tanabe, and T. Watanabe, "Ultrahigh-Q photonic crystal nanocavities realized by the local width modulation of a line defect," Applied Physics Letters 88, 041112-041111-041113 (2006).
38. T. Baba, "Slow light in photonic crystals," Nature Photonics 2, 465-473 (2008).
39. T. Matsumoto, S. Fujita, and T. Baba, "Wavelength demultiplexer consisting of Photonic crystal superprism and superlens," 13 26, 10768-10776 (2005).
40. D. Bernier, X. L. Roux, A. Lupu, D. Marris-Morini, L. Vivien, E. Cassan, and O. E. ", vol. 16, n°22, pp. , 2008., "Compact, low cross-talk CWDM demultiplexer using photonic crystal superprism," Opt. Express 16, 17209-17214 (2008).
41. S. Datta, C. T. Chan, K. M. Ho, and C. M. Soukoulis, "Effective dielectric constant of periodic structures," Physical Review B 48, 14937-14943 (1993).
42. P. Lalanne, "Effective medium theory applied to photonic crystals composed of cubic or square cylinders," Applied Optics 35, 5369-5380 (1996).
43. A. Kirchner, K. Busch, and C. M. Soukoulis, "Transport properties of random arrays of dielectric cylinders," Physical Review B 57, 277-288 (1998).
44. A. A. Krokhin, P. Halevi, and J. Arriaga, "Long-wavelength (homogenization) for two-dimensional photonic crystals," Physical Review B 65, 115208 (2002).
45. P. Halevi, A. A. Krokhin, and J. Arriaga, "Photonic Crystal Optics and Homogenization of 2D Periodic Composites," Physical Review Letters 82, 719-722 (1999).
46. A. D. Falco, S. C. Kehr, and U. Leonhardt, "Luneburg lens in silicon photonics," Opt. Expr. 19, 5156-5162 (2011).
47. B. Lombardet, L. A. Dunbar, R. Ferrini, and R. Houdré, "Fourier analysis of Bloch wave propagation in photonic crystals," Journal of the Optical Society of America B 22, 1179-1190 (2005).

FRENCH SUMMARY

CONTRIBUTION A L'EXPLORATION DES PROPRIETES DISPERSIVES ET DE POLARISATION DE STRUCTURES A CRISTAUX PHOTONIQUES GRADUELS

CONTRIBUTION TO THE EXPLORATION OF DISPERSIVE AND POLARIZING PROPERTIES OF GRADED PHOTONIC CRYSTAL STRUCTURES

Ce résumé en français est une courte synthèse des travaux de thèse détaillés plus amplement dans le reste du manuscrit rédigé en anglais.

1. INTRODUCTION

Ce travail de thèse s'inscrit dans le contexte des travaux de recherche effectués depuis quelques années autour du thème des matériaux artificiels pour l'optique, en particulier pour l'optique guidée. L'idée sous-jacente est de pouvoir définir des matériaux aux propriétés ajustables conduisant à des phénomènes électromagnétiques originaux (invisibilité, lentilles de Luneberg, Maxwell's fish-eye) et/ou à la possibilité de réaliser de fonctions optiques pour la transmission (guidage, multiplexage, …) ou le traitement (modulation, commutation, …) de signaux optiques.

Le domaine étudié est connexe de celui des métamatériaux photoniques, naturellement adaptés à cette problématique. Des phénomènes emblématiques, tels que le « cloaking » ou la réfraction négative, ont été d'abord étudiés puis démontrés expérimentalement dans la gamme des fréquences micro-ondes, typiquement dans la période 2000-2006. Parmi les articles les plus marquants dans ce domaine figure notamment [Sch-06]. La transposition directe des concepts utilisés aux longueurs d'ondes RF au domaine des longueurs d'onde optiques dans le proche infra-rouge (λ~1,5µm) s'est en fait avérée assez difficile en raison des contraintes technologiques posées par la fabrication de 'méta-atomes' de dimensions très sub-longueur d'onde (en pratique ~50nm) et des pertes induites par l'utilisation des métaux aux fréquences optiques. Sur le plan théorique, une adaptation des outils de transformation de coordonnées d'espace a été nécessaire afin de prendre en compte la nécessité d'une utilisation de matériaux aux propriétés quasi-isotropes usuellement rencontrés en optique (principaux semiconducteurs dont le silicium, oxydes, etc). Ceci s'est traduit par la proposition effectuée en 2008 d'une nouvelle transformation conforme [Li-08]. Ces travaux théoriques ont contribué à des avancées, mais n'ont pas permis de résoudre tous les problèmes, la conception de métamatériaux photoniques non-réduits à des cartes d'indice (comme dans [Gab-09,Lip-09]) restant basées sur l'utilisation de

métaux, donc à pertes. Une autre caractéristique de l'ensemble de ces travaux tient également à l'utilisation du principe d'homogénéisation, conduisant à un fonctionnement très large bande, perçu en général comme un avantage.

Sur ces deux points, pertes optiques et fonctionnement large bande (donc non-dispersif), nous avons cherché, dans ce travail de thèse, à nous démarquer de ces travaux, et notre choix s'est ainsi plutôt tourné vers l'utilisation de cristaux photoniques graduels [Rus-99], [Jia-04],[Cen-05] obtenus par un ajustement « lentement variable » des propriétés opto-géométriques du réseau d'un cristal photonique (facteur de remplissage, forme de la maille, etc). L'utilisation de matériaux semiconducteurs (silicium) ou diélectriques (silice, air) permet de diminuer le niveau des pertes optiques. Par ailleurs, le choix très souple du rapport période/longueur d'onde (a/λ) permet également d'envisager a priori un fonctionnement dans deux types de régimes : *régime d'homogénéisation* pour $a/\lambda<<0.5$, et *régime diffractif* pour $a/\lambda>0.25$ typiquement, ce dernier offrant la possibilité de reconfigurer les trajectoires des faisceaux optiques se propageant dans le milieu graduel par modification de la longueur d'onde et ainsi d'exploiter les effets dispersifs des cristaux photoniques.

Des études préliminaires ont été menées pour étudier les effets de déformations opto-géométriques de la maille des cristaux photoniques par des calculs de décomposition en ondes planes (Plane Wave Expansion), en considérant la possibilité d'un facteur de remplissage graduel, d'une orientation graduellement variable des vecteurs élémentaires du réseau périodique, et du rapport d'amplitude entre ces deux vecteurs élémentaires. Elles ont permis de dégager des tendances qualitatives intéressantes et de préparer les perspectives à ce travail de thèse. Cela dit, devant la richesse et la complexité des possibilités offertes par un gradient bi-dimensionnel arbitraire de ces paramètres ou d'une combinaison d'entre eux, nous avons fait le choix de restreindre les études menées dans cette thèse au cas d'un cristal photonique de maille carrée et à facteur de remplissage graduel. Les résultats résumés ci-après ont été obtenus pour ce type de structures.

2. PRINCIPAUX RESULTATS DE SIMULATION-MODELISATION :

a) <u>Etape préalable</u> : Modélisation de la propagation de la lumière par extraction de la structure de bandes photonique et utilisation des lois de l'optique Hamiltonnienne

Afin de pouvoir dimensionner les structures graduelles à cristaux photoniques et prévoir leur comportement, voire, dans certains cas, les concevoir en fonction de telle ou telle propriété visée, nous avons commencé par mettre en place une méthodologie de modélisation. La direction de propagation des modes de Bloch propagatifs d'un cristal photonique étant bien décrite par la notion de courbe iso-fréquence extraite du diagramme de dispersion [Lou-09], nous nous sommes appuyés sur une description de ce type, que nous avons couplée aux équations de l'optique Hamiltonienne [Rus-99]. Cette dernière approche consiste à propager un ou plusieurs rayons lumineux selon deux équations maîtresses décrivant l'évolution de la position $\boldsymbol{r}$ et du vecteur d'onde $\boldsymbol{k}$ de chaque rayon en fonction du gradient en $\boldsymbol{k}$ et en $\boldsymbol{r}$ d'un Hamiltonien $H(\boldsymbol{r},\boldsymbol{k})$ dépendant de la structure de bandes photonique locale.

Cette approche a été appliquée au cas d'un cristal photonique planaire constitué d'un réseau de maille carrée de trous d'air de rayon *r* gravés dans un film mince de silicium d'épaisseur *h*=260nm,, de paramètre de maille *a* (=380nm), et de facteur de remplissage $f=\pi(r/a)^2$ graduel dans le plan d'un substrat silicium sur isolant (SOI). Dans ces structures, le confinement vertical est obtenu par guidage réfractif dans un guide plan asymétrique SiO_2 (substrat)/Si (*h*=260nm) / air (superstrat).

Afin de modéliser la propagation de la lumière dans ce type de cristal photonique graduel, nous avons extrait des expressions analytiques des courbes de dispersion iso-fréquences de la première bande photonique au voisinage des extrema de la zone de Brillouin (points M : voir **Fig. RF1**), qui ont été couplées aux deux équations de l'optique Hamiltonienne, permettant de décrire la propagation de la lumière dans le cas d'un profil bi-dimensionnel du facteur de remplissage arbitraire, soit $f=f(x,y)$, *x* et *y* représentant les deux coordonnées d'espace du plan des couches.

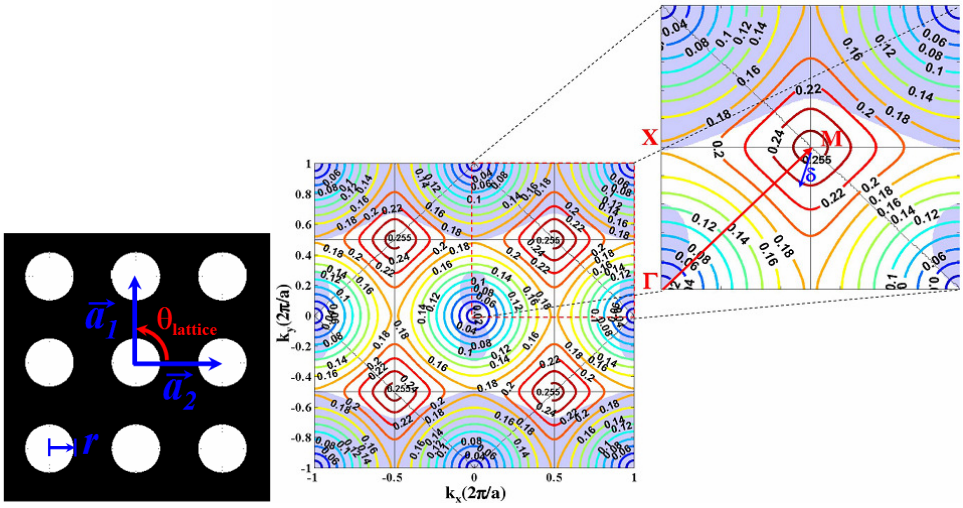

(a) (b)

Figure RF1 : (a) Vue de principe du réseau direct d'un cristal photonique de maille carrée constituée de trous cylindriques d'air de rayon normalisé $r/a = 0.3$ perçés dans une matrice de haut indice,(b) Courbes iso-fréquences de la première bande photonique en polarisation TE (paramètres complets : [Cas-11a]).

Une comparaison de cette approche avec des simulations FDTD (Finite Difference Time Domain Simulation) a permis d'en montrer la validité (voir **Fig. RF2**), indiquant ainsi la pertinence de ce modèle simple de propagation de la lumière pouvant conduire à une discussion physique aisée (connaissance de la bande photonique excitée, suivi des paramètres opto-géométriques du cristal photonique graduel le long des trajectoires) et à une optimisation beaucoup plus rapide des facteurs de remplissage en trous ou du point d'excitation de la structure graduelle depuis un guide plan qu'une simulation numérique complète. Ces différents aspects ont été détaillés dans [Cas-11a].

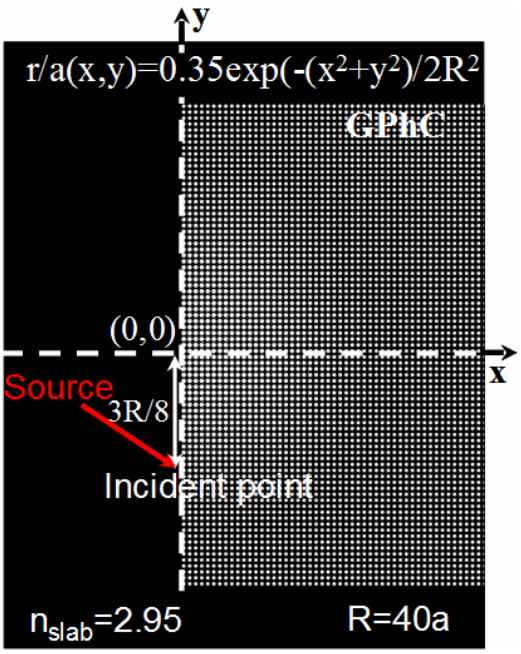

(a)

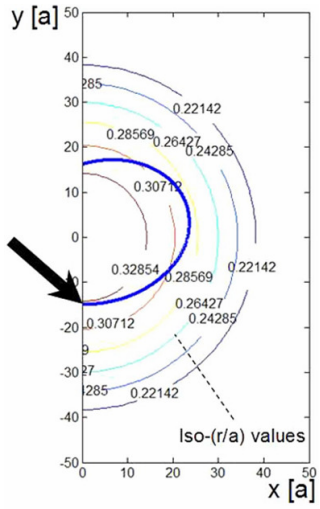

(b)

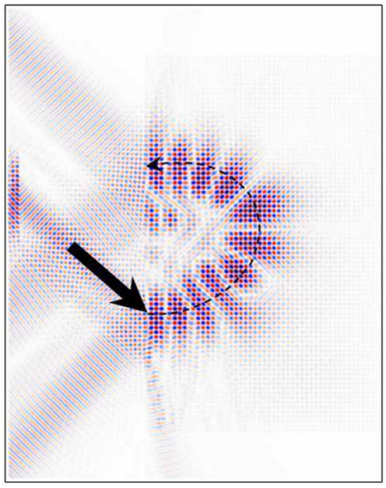

(c)

Figure RF2 : **(a)** Carte de permittivité diélectrique de la structure proposée de cristal photonique planaire dont la loi d'évolution du rayon normalisé des trous d'air est donnée par : r/a=0.35.exp(-(x^2+y^2)/(2R^2)) ;
(b) Propagation d'un rayon lumineux à la fréquence normalisée ω=a/λ=0.25 injecté dans le cristal photonique graduel au point (x=0;y=3R/8) ; **(c)** Propagation de la lumière dans les mêmes conditions à l'aide du logiciel de FDTD MEEP, la flèche en traits pointillés représentant le trajet du rayon lumineux du (b).

b) <u>Principaux résulats de modélisation</u> :

La méthodologie de modélisation développée a permis d'étudier les propriétés du cristal photonique graduel à maille carrée considéré dans la thèse. Les principaux résultats de modélisation obtenus peuvent être classés en trois points.

i) Effet de courbure des faisceaux optiques

Nous avons identifié les conditions d'excitation (orientation du cristal photonique à 45°, caractéristiques des faisceaux excitateurs : angle d'incidence, largeur des faisceaux, choix de la localisation du point d'injection, etc) permettant d'observer un effet de courbure ou de superbending de la lumière [Cen-06] au sein du cristal photonique vers les régions à fort facteur de remplissage en trous d'air (c'est-à-dire de plus bas indice de réfraction au sens de l'homogénéisation des milieux optiques). Une optimisation des entrées/sorties du cristal photonique graduel a par ailleurs été effectuée, se traduisant par la conception de zones d'adapation d'impédance électromagnétique (« tapers »). Ces résulats sont résumés en **Fig. RF3**.

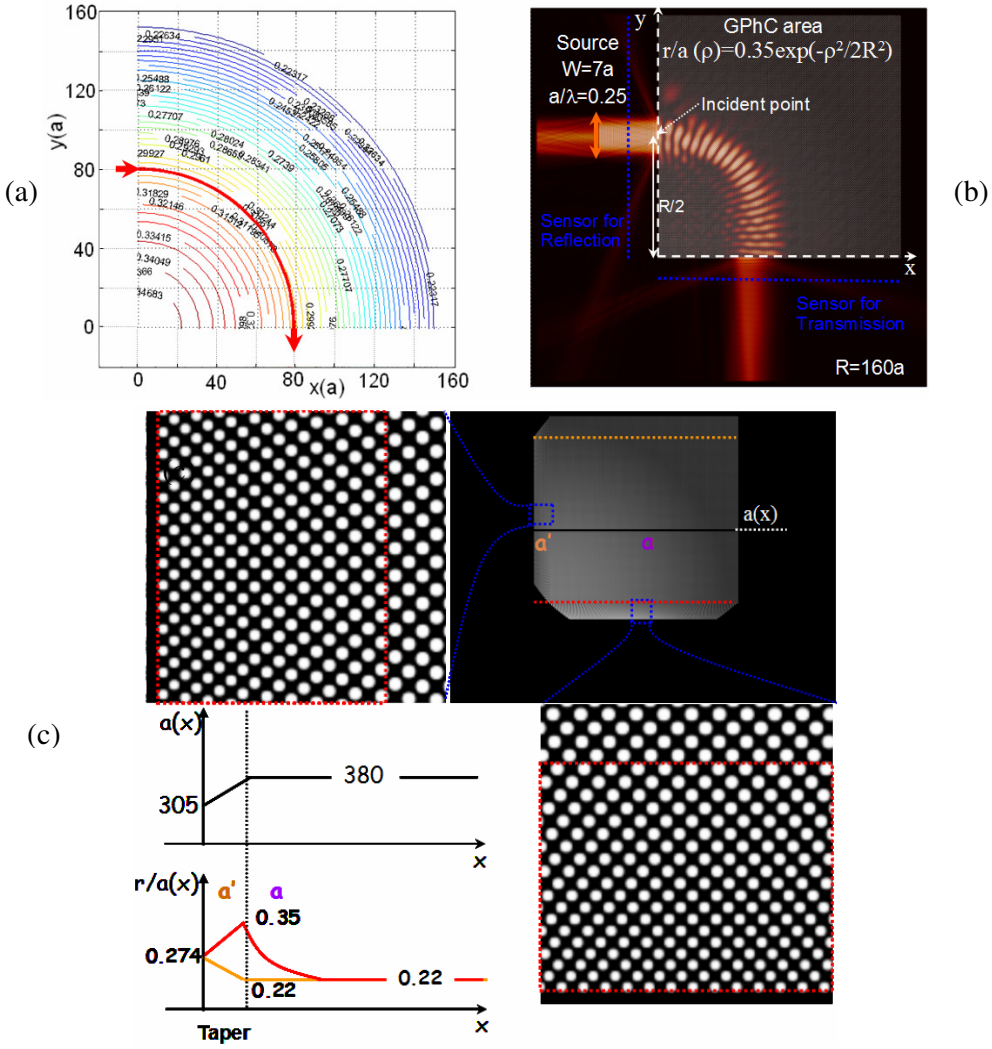

Figure RF3 : Effet de courbure de la lumière par le cristal photonique graduel considéré (maille carrée, facteur de remplissage graduel) (détail des paramètres : [Do-12] : (a) Optimisation du point d'entrée au sein du cristal photonique par propagation d'un rayon à l'aide de la structrure de bandes photoniques locales, (b) Résultat de simulation FDTD de l'effet de mirage optique à λ=1550nm, (c) Détail du résultat de l'optimisation des tapers d'entrée/sortie permettant de diminuer les pertes d'insertion globales de la structure à cristal photonique graduel.

ii) Dispersion en longueur d'onde

Bien que de conception relativement simple, inspirée du profil d'indice de réfraction déduit d'un calcul analytique valable en régime d'homogénéisation [Cas-11b], la structure de cristal photonique graduelle proposée s'est avérée présenter des propriétés de dispersion en longueur d'onde assez intéressantes.

L'origine physique de cette dispersion tient au fait que les courbes iso-fréquences du milieu graduel au sein duquel se propage la lumière dépendent à la fois de la position locale au sein de la structure mais également de la fréquence. En conséquence, deux faisceaux optiques de longueurs d'ondes différentes mais injectés au même point du cristal photonique suivent des trajectoires différentes, ce qui permet, en principe, de les séparer si la distance des points de sortie de ces deux faisceaux est supérieure à leur extension latérale.

Une dispersion assez comparable à celles de dispositifs de type « superprisme » à cristaux photoniques a ainsi été obtenue, autour des 0,25°/nm. Par rapport à ces dernières, les deux avantages suivants sont apparus :

- la divergence par diffraction des faisceaux s'est avérée très faible lors de la propagation, ceci étant lié à la forme des courbes iso-fréquences graduelles exploitées,
- la dispersion spatiale (°/nm) s'est avérée linéaire dans une gamme spectrale de l'ordre de 200nm.

Ces résultats, qui font actuellement l'objet d'une soumission à des revues à comités de lecture, sont décrits davantage dans la partie 3) de ce résumé.

iii) Sensibilité à la polarisation de la lumière

Les cristaux photoniques planaires sont connus pour être très sensibles à la polarisation de la lumière, c'est-à-dire présenter une forte biréfringence TE/TM. Intuitivement, il doit en être de même pour les cristaux photoniques graduels. Curieusement, ces derniers n'ont pas été étudiés dans la littérature pour leurs propriétés vis-à-vis de la polarisation. Sans aborder cette question dans sa généralité, ce qui serait plutôt à classer parmi les perspectives à ce travail de thèse, nous avons restreint ici notre étude à celle du comportement de la *« structure-type »* considérée dans cette thèse (**Fig. RF3 (b)**). La **Fig. RF4** résume les principaux résulats de modélisation obtenus.

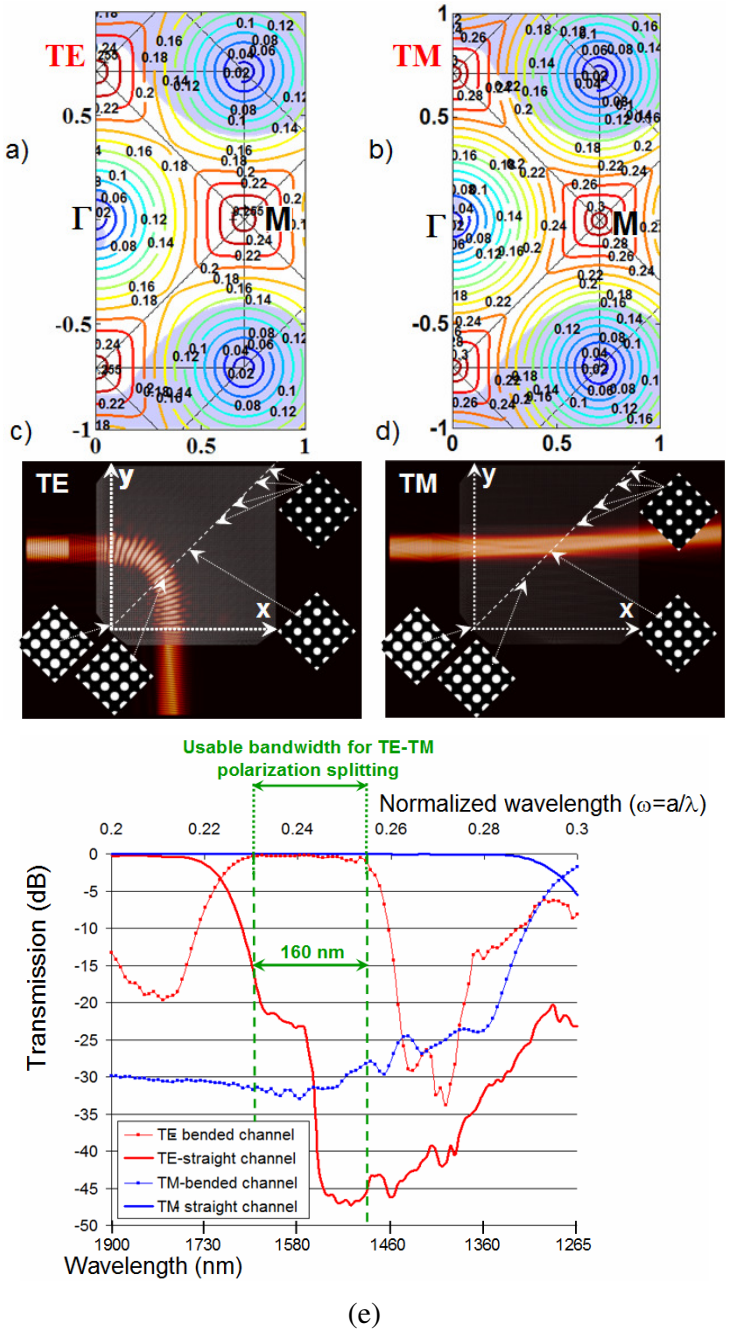

Figure RF4 : Effet de séparation des polarisations TE et TM par la structure-type de cristal photonique : a),b) Courbes iso-fréquences, c),d) Cartes de champ obtenues par simulation FDTD, e) Transmission de la structure sur les canaux direct et à 90° faisant apparaître les pertes d'insertion et la diaphotie inter-canaux.

Un effet très net de séparation des deux polarisations TE et TM est ainsi obtenu. Physiquement, cet effet est lié à la biréfringence d'indice TE/TM qui conduit, à même longueur d'onde, à faire opérer le cristal photonique graduel en régime d'homogénéisation pour la polarisation TM et en régime diffractif pour la polarisation TE. Ceci conduit à induire une trajectoire assez rectiligne pour les faisceaux en polarisation TM, tandis qu'une forte courbure à 90° est obtenue pour les faisceaux en polarisation TE en raison de l'inversion de concavité des courbes iso-fréquences en bord de zone de Brillouin par rapport à un 'milieu ordinaire'.

D'un point de vue fonctionnel, les avantages de cette structure par rapport à celles proposées jusqu'ici sont de :

- permettre une injection/collection à incidence normale par rapport à l'interface guide plan/cristal photonique graduel, ce qui permet de limiter les pertes d'insertion de la structure,
- séparer les fonctions d'injection de la lumière et de séparation des polarisations,
- d'opérer par une « séparation douce » des polarisations liée à la gradualité de la structure.

3. PRINCIPAUX RESULTATS EXPERIMENTAUX

Des résultats expérimentaux ont été obtenus sur les trois volets décrits dans la section 2).

Les structures ont été fabriquées à l'Institut d'Electronique Fondamentale (UMR CNRS 8622) par lithographie électronique et gravure ICP. Une attention particulière a été portée à la correction des effets de proximité, essentielle pour la définition de motifs graduels au sein d'un cristal photonique. La contribution de Xavier LE ROUX, ingénieur salle blanche/process à l'IEF, a été essentielle sur l'ensemble de ces aspects. La **Fig. RF5** rassemble quelques images prises au microscope électronique à balayaye (MEB) d'un dispositif réalisé.

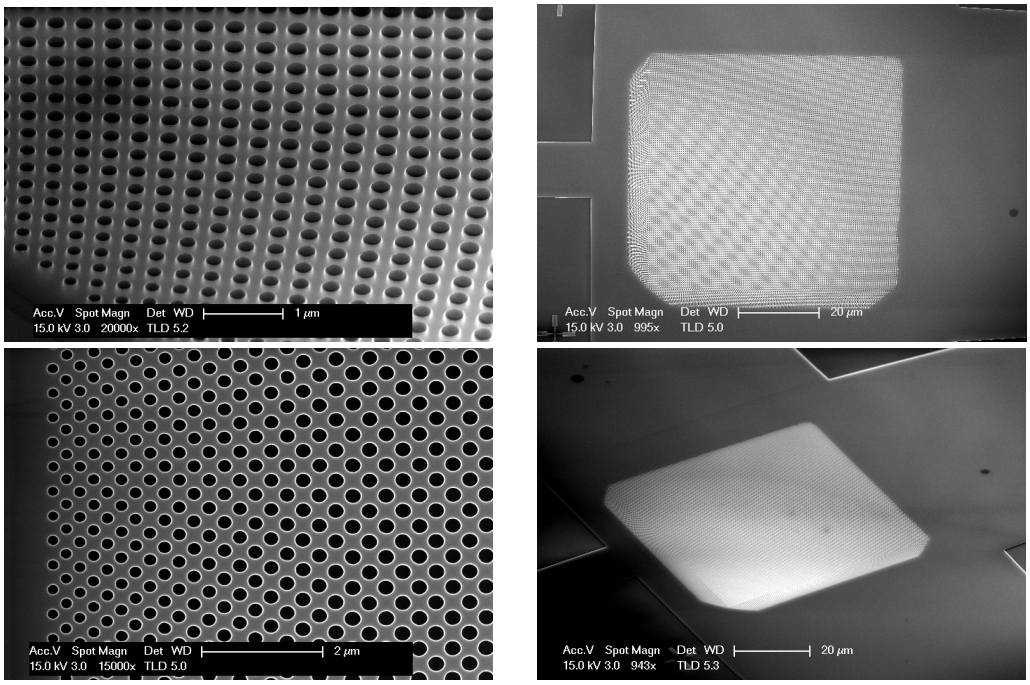

Figure RF5 : Photos MEB d'une structure fabriquée à l'IEF :
GAUCHE : Détails du cristal et vue du détail de la gradualité d'un « taper » d'entrée
DROITE : Vues d'ensemble de la structure-type de cristal photonique graduel et sous deux incidences

La **Fig. RF6** donne, quant à elle, deux vues différentes d'une autre structure présentant un guide d'entrée et deux guides ruban de sortie, orientée vers la réalisation d'un démultiplexeur en longueur d'ondes élémentaire.

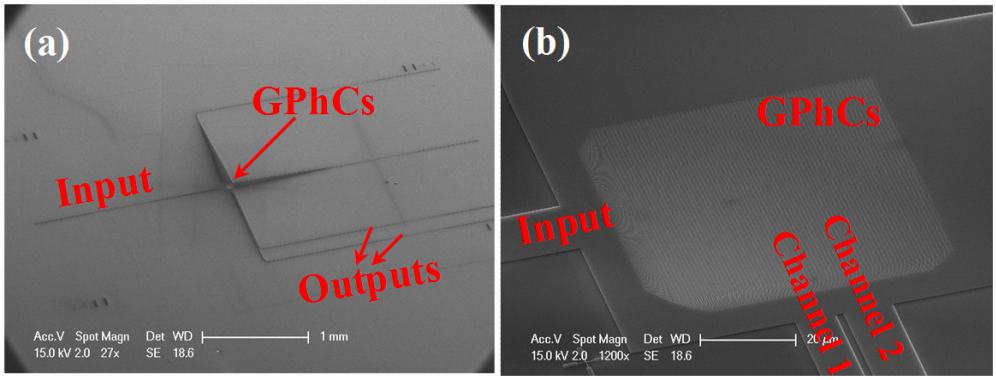

Figure RF6 : Photos MEB d'une autre structure fabriquée à l'IEF :

Concernant les mesures, deux types principaux en ont été effectués (**Fig. RF7**) :

- Des mesures de transmission ont été effectuées sur les bancs de mesure de l'opération Minaphot (http://silicon-photonics.ief.u-psud.fr/) de l'IEF. La lumière est couplée par la tranche au moyen de fibres lentillées positionnées correctement, puis collectée en sortie d'échantillon, soit au moyen d'une fibre, soit d'un objectif de microscope. Une mesure du spectre optique en transmission est alors possible en quelques secondes grâce à l'instrumentation du banc.
- Des mesures en champ proche optique (SNOM) ont également été effectuées. Nous avons eu le plaisir pour cela de collaborer avec le groupe de champ proche optique dirigé à l'Institut Inter-disciplinaire Carnot de Bourgogne (ICB) par Frédérique de Fornel. Ce type de mesures a apporté une visualisation directe des phénomènes de courbure de la lumière et de sensibilité à la longueur d'onde et à la polarisation. Les séries d'images prises dans une plage spectrale assez large (typiquement 1300nm<λ<1650nm => *Hyp-SNOM*) se sont également avérées un outil d'analyse très riche pour la compréhension des phénomènes de propagation apparaissant dans les CP graduels.

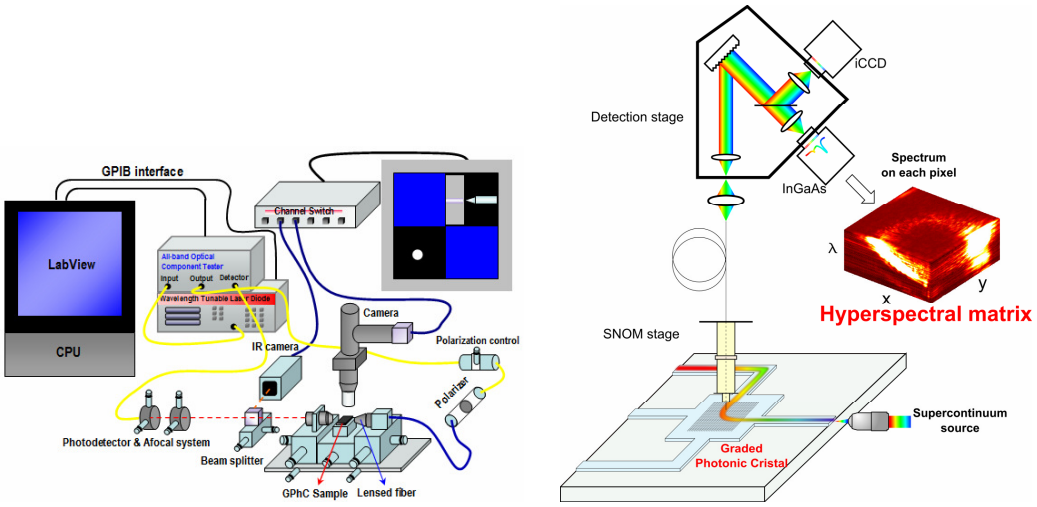

Figure RF7 : Environnement et méthodes de mesures :
GAUCHE : Mesures champ lointain de la transmission des échantillons (IEF)
DROITE : Mesures hyperspectrales en champ proche optique, ou Hyp-SNOM (ICB)

i) Effets de courbure des faisceaux optiques et de sensibilité à la longueur d'onde

La **Fig. RF8** donne la carte de champ hyperspectrale obtenue expérimentalement par *Hyp-SNOM*, l'extension spectrale mesurée en plusieurs points de sortie de la structure à CP graduel, le décalage du point de sortie du faisceau (directement lié à la dispersion en longueur d'onde), ainsi que des indications concernant l'élargissement spatial et l'élargissement spectral des faiscaux se propageant au sein de la région structurée par des trous d'air de diamètres variables.

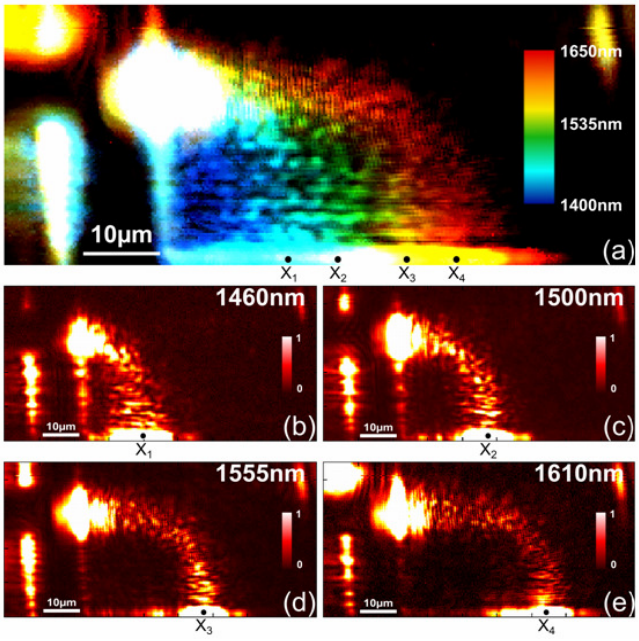

Figure RF8 : Mesure de l'effet de courbure et de l'effet de dispersion de la structure-type : Mesure par Hyp-SNOM

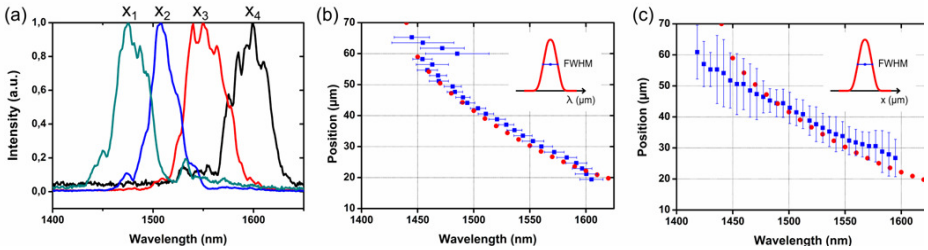

Figure RF9 : Mesure de l'effet de courbure et de l'effet de dispersion de la structure-type : a) largeur spectrale en plusieurs points, b) et c) dispersion en longueur d'onde (bleu : SNOM ; rouge : calculs PWE-3D et propagation de rayons)

Les résultat expérimentaux obtenus ont démontré :

- l'effet de courbure de la lumière prédit par plusieurs travaux antérieurs mais encore non mesuré jusque là aux longueurs d'ondes optiques,
- une forte sensibilité à la longueur d'onde du décalage du faisceau de sortie (40µm environ pour une plage spectrale de l'ordre de 150nm),
- une quasi-linéarité de cette dispersion en longueur d'onde,
- un accord quantitatif avec les résultats des modélisations effectuées par extraction de la structure de bandes photonique locale et propagation de rayons optiques (des simulations PWE-3D avec prise en compte de l'asymétrie de la membrane verticale ont néanmois été nécessaires pour cela).

Ces effets dispersifs ont également été relevés par des mesures en champ lointain effectuées à l'IEF sur des structures telles que celle présentée en **Fig. RF6**. La **Fig. RF10** donne les spectres ainsi collectés sur les deux canaux, indiquant un accord correct avec les modélisations FDTD (*les écarts constatés sont liés au caractère 2D des expériences numériques*), des pertes d'insertion faible (<-1,5dB), et des niveaux de diaphotie intercanal de l'ordre de -20dB.

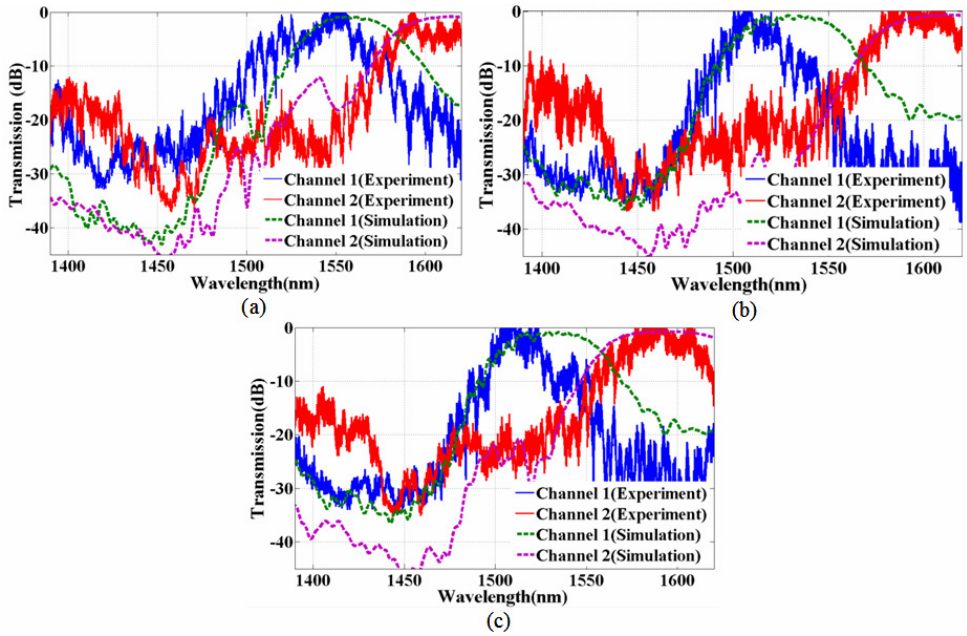

Figure RF10 : Spectres de transmission obtenus expérimentalement pour le dispositif présenté en **Fig. RF6**.

ii) Sensibilité à la polarisation de la lumière

Cette effet a été relevé lors des mesures en champ lointain effectuées à l'IEF, puis par la technique de champ proche optique développée à l'ICB. La **Fig. RF11** en donne une illustration.

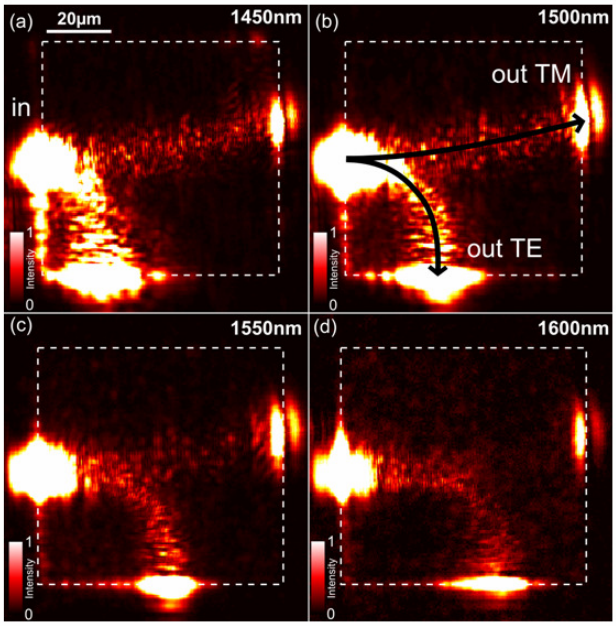

Figure RF11 : Caractérisation par champ proche optique hyper-spectral de l'effet de séparation des polarisations TE/TM

4. CONCLUSION ET PERSPECTIVES

Cet aperçu rapide des résultats de la thèse résume les principales contributions du travail qui a été mené pendant trois ans.

L'accent a été mis sur une méthodologie de modélisation assez générale, basée sur la description de la propagation de la lumière à partir de la structure de bandes photonique locale, mais elle a été très essentiellement appliquée à une « structure-type » simple constituée d'un cristal photonique planaire à réseau carré, de facteur de remplissage variable, et fonctionnant en bande 1.

La motivation pour cette approche a découlé :

- d'une part de la très grande richesse des « chirps bi-dismensionnels » possibles pour la définition de cristaux photoniques graduels (*facteur de remplissage, vecteurs du réseau direct en orientations et en normes, forme et orientation du motif élémentaire, bande photonique exploitée, ou une combinaison de ces paramètres*) qui rendait difficile une analyse des propriétés générales des cristaux photoniques graduels avant l'étude détaillée d'une structure particulière,
- et d'autre part de notre souhait de démontrer expérimentalement un certain nombre de résultats avant de nous consacrer à d'autres types de CP graduels.

Nous n'avons pas laissé ces aspects de côté ; ils font en effet l'objet de nos perspectives.

La « structure-type » qui a été étudiée, bien que simple, s'est finalement avérée assez riche. Elle a permis de démontrer expérimentalement l'effet de courbure de la lumière dans un CP graduel par des mesures effectuées en champ lointain [Do-12], mais également par des mesures de champ proche optique effectuées dans le cadre d'une collaboration active avec l'Institut Inter-disciplinaire Carnot de Bourgogne (ICB) [soumis]. Ont également été démontrés, quantifiés, et interprétés les effets de dispersion en longueur d'onde et de sensibilité à la polarisation de la lumière.

Les perspectives à ce travail sont nombreuses. Nous les avons évoquées ci-dessus. Le potentiel des cristaux photoniques graduels n'a en effet, selon nous, pas encore été exploité compte tenu notamment du manque d'approche et de méthodologie générale pour l'étude de ces matériaux optiques artificiels fonctionnant en régime diffractif et ne pouvant donc pas être facilement décrits par les méthodes de transformations spatiales de coordonnées applicables aux métamatériaux photoniques. Nous espérons pouvoir contribuer à l'avenir à cet objectif.

5. BIBLIOGRAPHIE

[Cas-11a] E. Cassan, K.V. Do, C. Caer, D. Marris-Morini, L. Vivien

"Short-Wavelength Light Propagation in Graded Photonic Crystals"

Journal of Lightwave Technology 29 (13), 1937-1943 (2011)

[Cas-11b] E. Cassan, K. V. Do

"Analytic design of graded photonic crystals in the metamaterial regime"

Journal of the Optical Society of America B **28** (8), 1905-1910 (2011)

[Cen-05] E. Centeno, D. Cassagne

"Graded photonic crystals"

Optics Letters 30 (17), 2278-2280 (2005)

[Cen-06] E. Centeno, D. Cassagne, J.-P. Albert

"Mirage and superbending effect in two-dimensional graded photonic crystals"

Phys. Rev. B 73, 235119-1-5 (2006)

[Do-12] K.-V. Do, X. Le Roux, D. Marris-Morini, L. Vivien, E. Cassan

"Experimental demonstration of light bending at optical frequencies using a non-homogenizable graded photonic crystal"

Optics Express 20 (14), 4476-4783 (2012)

[Gab-09] L. H. Gabrielli, J. Cardenas, C. B. Poitras, M. Lipson

"Silicon nanostructure cloak operating at optical frequencies"

Nature Photonics **3**, 461-463 (2009)

[Jia-04] Jiao, S. Fan, D. A. B. Miller

"Designing for beam propagation in periodic and nonperiodic nanostructures: Extended Hamiltonian method"

Physical Review E 70, 036612-1-9 (2004)

[Li-08] J. Li, J.B. Pendry

"Hiding under the carpet : A New Strategy for Cloaking"

Physical Review Letters **101**, 203901-1-4 (2008)

[Lou-09] J.-M. Lourtioz, H. Benisty, V. Berger, J.-M. Gerard, D. Maystre, A. Tchelnokov

"Photonic Crystals: Towards Nanoscale Photonic Devices"

Springer, 2009

[Rus-99] P.S. Russel, T. A. Birks

"Hamiltonian approach of non-uniform photonic crystals"

Journal of Lightwave Technology 17 (11), 1982-1988 (1999)

[Sch-06] D. Schurig, J. J. Mock, B. J. Justice, S. A. Cummer, J. B. Pendry, A. F. Starr, D. R. Smith

"Metamaterial electromagnetic cloak at microwave frequencies"

Science **314** (5801), 977-980 (2006)

[Val-09] J. Valentine, J. Li, T. Zentgraf, G. Bartal, X. Zhang

"An optical cloak made of dielectrics"

Nature Materials **8**, 568-571 (2009)

Publications and Conferences

Publications:

1. E. Cassan and K. V. Do, "Analytic design of graded photonic crystals in the metamaterial regime", JOSA-B **28**(8), pp 1905-1910 (2011).
2. E. Cassan, K. V. Do, C. Caer, D. Marris-Morini and L. Vivien, "Short-wavelength light propagation in graded photonic crystals", Journ. of Lightwave Techn. **29**(13), 1937-1943 (2011).
3. K. V. Do, X. Le Roux, C. Caer, D. Marris-Morini, N. Izard, L. Vivien and E. Cassan, "Wavelength demultiplexer based on a two-dimensional graded photonic crystal", Photonics Techn. Lett. **23**(15), 1094-1096 (2011).
4. C. Caer, X. Le Roux, V. Khanh Do, D. Marris-Morini, N. Izard, L. Vivien, D. Gao, E. Cassan "Dispersion engineering of Wide Slot Photonic Crystal Waveguides by Bragg-like Corrugation of the Slot" Photonics Technology Letters **23**(18), 1298-1300, (2011).
5. K-V Do, X. Le Roux D. Marris-Morini, L. Vivien and E. Cassan, "Experimental demonstration of light bending at optical frequencies using a non-homogenizable graded photonic crystal", Optics Express, **20**(4), 4776-4783, (2012).
6. Do K. V., Le Roux X. , Caer C., Morini D., Vivien L., Cassan E., "All-dielectric photonic metamaterials operating beyond the homogenization regime", Advanced Electromagnetics, http://aemjournal.org/index.php/AEM/article/view/80, **1**(6) (2012)

Conferences:

1. Khanh Van DO, Eric CASSAN, Xavier Le Roux, Charles CAER, Delphine MARRIS-MORINI, Laurent VIVIEN "*Cristaux photoniques en régime d'homogénéisation approach*" Colloque National Métamatériaux (CNM 2011)
2. K. V. Do, E. Cassan, HELIOS project summer school (http://www.helios-project.eu/) "*Propagation of light in graded photonic crystal*".

3. C. Caer, X. Le Roux, K. V. Do, D. Marris-Morini, L. Vivien, E. Cassan, "*Bragg-like Corrugations of Slot Photonic Crystal Waveguides for Dispersion Engineering*", International Conference on Solid State Devices and Materials (SSDM 2011), 28-30 Septembe, 2011, Nagoya, Japan

4. E. Cassan, K. V. Do, X. Le Roux, C. Caer, D. Marris-Morini, N. Izard, L.Vivien "*Proposal for new method to design all-dielectric photonic metamaterials using an analytical approach*", Fifth International Congress on Advanced Electromagnetic Materials in Microwaves and Optics (Metamaterials 2011), Barcelona, Spain, 10-15 October 2011

5. E. Cassan, K. V. Do, D. Marris-Morini and L. Vivien, "*Analytic design of chirped planar photonic crystals in the metamaterial regime*", Photonics Europe 2012, Bruselles, 16-19 April 2012.

6. K. V. Do, X. Le Roux, D. Marris-Morini, L. Vivien and E. Cassan, "*Experimental demonstration of light bending effect at optical wavelengths in a non-homogenizable graded photonic crystal*", Photonics Europe 2012, Bruselles, 16-19 April 2012.

7. Cassan E., Do Khanh V., Le Roux X., Caer C., Marris-Morini D., Vivien L., "*All-dielectric photonic metamaterials operating beyond the homogenization regime*", META'12 (International Conference on Metamaterials, Photonic Crystals, and Plasmonics), 20120419 – 20120422, Paris